8-2012

Development and Implementation of the Use of Optically Stimulated Luminescent Detectors in the Radiological Physics Center Anthropomorphic Quality Assurance Phantoms

Jennelle Bergene

DEVELOPMENT AND IMPLEMENTATION OF THE USE OF OPTICALLY STIMULATED LUMINESCENT DETECTORS IN THE RADIOLOGICAL PHYSICS CENTER ANTHROPOMORPHIC QUALITY ASSURANCE PHANTOMS

by

Jennelle E. Bergene, B.S.

APPROVED:

_____
David Followill, Ph.D.
Supervisory Professor

_____
Stephen Kry, Ph.D.

_____
Andrea Molineu, M.S.

_____
David Bellezza, M.S.

_____
Laurence Court, Ph.D.

_____
Valen Johnson, Ph.D.

APPROVED:

_____
Dean, The University of Texas
Graduate School of Biomedical Sciences at Houston

DEVELOPMENT AND IMPLEMENTATION OF THE USE OF OPTICALLY STIMULATED LUMINESCENT DETECTORS IN THE RADIOLOGICAL PHYSICS CENTER ANTHROPOMORPHIC QUALITY ASSURANCE PHANTOMS

A

THESIS

Presented to the Faculty of
The University of Texas
Health Science Center at Houston
and
The University of Texas
M. D. Anderson Cancer Center
Graduate School of Biomedical Sciences
in Partial Fulfillment

of the Requirements

for the Degree of

MASTER OF SCIENCE

by

Jennelle E. Bergene, B.S.
Houston, Texas

August 2012

Acknowledgements

I would like to thank my advisor, Dr. David Followill, for giving me the opportunity to work on this project, and his guidance and patience along the way. Dr. Followill has been a great source of encouragement and motivation throughout this project, and I so appreciate him not giving up on me when I told him I was going to have a baby during the writing process and not long before my defense. Also, thank you to the members of my committee for their ideas and time: Dr. Stephen Kry, Andrea Molineu, David Bellezza, Dr. Laurence Court, and Dr. Valen Johnson.

I would like to express my gratitude to the many wonderful people at the RPC who have helped me and encouraged me throughout my project, especially Paola Alvarez, Carrie Amador, Lynda McDonald, Sarah Willis, Sonia Gonzalez, and to John Costales at UH for all the phantom machining he did. The RPC has been a wonderful place to work and learn, and I am so thankful for the time I have been able to work there and for the people that make it what it is. To my fellow students and friends, especially Kevin Casey, Kevin Vredevoogd, Jessie Huang, and Mitchell Carroll, thank you for answering my questions, providing feedback, your support, and for just being awesome people. A special thanks to Kevin Casey for your reading and editing talents. Thanks also go out to James Kerns, for answering my questions on his work and his extremely prompt responses to my emails.

Finally, to my husband and my children, thank you for all your love, support and patience. Thank you for putting up with my long hours, erratic schedule, and having an anxious wife and mommy at times. Also, thanks to my wonderful, encouraging, taskmaster of a mother for taking such good care of me and my family after the baby was born, allowing me to finish this work and really concentrate my efforts.

DEVELOPMENT AND IMPLEMENTATION OF THE USE OF OPTICALLY STIMULATED LUMINESCENT DETECTORS IN THE RADIOLOGICAL PHYSICS CENTER ANTHROPOMORPHIC QUALITY ASSURANCE PHANTOMS

Publication No._____

Jennelle E. Bergene, B.S.

Supervisory Professor: David Followill, Ph.D.

The Radiological Physics Center (RPC) uses both on-site and remote reviews to credential institutions for participation in clinical trials. Anthropomorphic quality assurance (QA) phantoms are one tool the RPC uses to remotely audit institutions, which include thermoluminescent dosimeters (TLDs) and radiochromic film. The RPC desires to switch from TLD as the absolute dosimeter in the phantoms, to optically stimulated luminescent dosimeters (OSLDs), but a problem lies in the angular dependence exhibited by the OSLD. The purpose of this study was to characterize the angular dependence of OSLD and establish a correction factor if necessary, to provide accurate dosimetric measurements as a replacement for TLD in the QA phantoms. A 10 cm diameter high-impact polystyrene spherical phantom was designed and constructed to hold an OSLD to study the angular response of the dosimeter under the simplest of circumstances for both coplanar and non-coplanar treatment deliveries. OSLD were irradiated in the spherical phantom, and the responses of the dosimeter from edge-on angles were normalized to the response when irradiated with the beam incident normally on the surface of the dosimeter. The average normalized response was used to establish an angular correction factor for 6 MV and 18 coplanar treatments, and for 6 MV non-coplanar treatments specific to CyberKnife. The RPC pelvic phantom dosimetry insert was modified to hold OSLD, in addition to the TLD, adjacent to the planes of film. Treatment plans of increasing angular beam delivery were developed, three in Pinnacle v9.0 (4-field box, IMRT, and VMAT) and one in Accuray's MultiPlan v3.5.3 (CyberKnife). The plans were delivered to the pelvic phantom containing both TLD and OSLD in the target volume. The pelvic phantom was also sent to two institutions to be irradiated as trials, one delivering IMRT, and the other a CyberKnife treatment. For the IMRT deliveries and the two institution trials, the phantom also included film in the sagittal and coronal planes. The doses measured from the TLD and OSLD were calculated for each irradiation, and the angular correction factors established from the spherical phantom irradiations were applied to the OSLD dose. The ratio of the TLD dose to the angular corrected OSLD dose was calculated for each irradiation. The corrected OSLD dose was found to be within 1% of the TLD measured dose for all irradiations, with the exception of the in-house CyberKnife deliveries. The films were normalized

to both TLD measured dose and the corrected OSLD dose. Dose profiles were obtained and gamma analysis was performed using a 7%/4 mm criteria, to compare the ability of the OSLD, when corrected for the angular dependence, to provide equivalent results to TLD. The results of this study indicate that the OSLD can effectively be used as a replacement for TLD in the RPC's anthropomorphic QA phantoms for coplanar treatment deliveries when a correction is applied for the dosimeter's angular dependence.

Table of Contents

Signature Page i

Title Page ii

Acknowledgements iii

Abstract iv

Table of Contents vi

List of Figures x

List of Tables xviii

List of Equations xix

Chapter 1 Introduction 1

1.1 Statement of Problem 1

1.2 Radiological Physics Center 2

1.3 Optically Stimulated Luminescence 3

1.3.1 OSL Phenomenon 3

1.3.2 Properties of Al_2O_3:C Dosimeters 5

1.3.3 Measurement of OSL Signal 7

1.4 Hypothesis and Specific Aims 9

Chapter 2 Methods and Materials 10

2.1 Phantoms 10

2.1.1 Spherical Phantom 10

2.1.2 RPC Pelvic Phantom 10

2.1.3 Slab Phantom 12

2.2 Treatment planning 13

2.2.1 Phantom Simulation 13

2.2.2 Dose Prescription 14

2.2.3 Planning Procedures 15

2.2.3.1 Four Field Box 16

2.2.3.2 IMRT 16

2.2.3.3 VMAT 16

2.2.3.4 CyberKnife 17
2.3 Phantom Irradiations 17
2.3.1 Spherical Phantom Irradiations 17
2.3.1.1 Coplanar 6 MV Irradiations 18
2.3.1.2 Coplanar 18 MV Irradiations 20
2.3.1.3 Non-coplanar 6 MV Irradiations 20
2.3.2 Pelvic Phantom Irradiations 21
2.3.2.1 Institution Trials 23
2.3.3 Energy Correction Irradiations 23
2.4 RPC TLD Dosimetry 25
2.4.1 TLD Batch Correction Factors 25
2.4.2 System Sensitivity 26
2.5 RPC OSLD Dosimetry 26
2.5.1Element Correction Factor 28
2.5.2 OSLD Batch Correction Factors 28
2.5.3 microStar™ Reader 29
2.5.4 Signal Depletion 30
2.5.5 Optical Bleaching 31
2.6 RPC Film Dosimetry 31
2.6.1 Film Scanning 33
2.6.2 Registration 34
2.7 Dosimetric Evaluation 34
2.7.1 Absolute Dose 35
2.7.2 Dose Profiles 36
2.7.3 Gamma Analysis 36
Chapter 3 Results and Discussion 38
3.1 Treatment Planning 38
3.1.1 Four Field Box 38
3.1.2 IMRT 39

3.1.3 VMAT 39
3.1.4 CyberKnife 40
3.2 Phantom Irradiations 41
3.2.1 Spherical Phantom Irradiations 41
3.2.2 Pelvic Phantom Irradiations 47
3.2.3 Energy Correction Irradiations 49
3.3 Dosimetric Evaluation 52
3.3.1 Absolute Dose 52
3.3.2 Dose Profiles 56
3.3.3 Gamma Analysis 61
Chapter 4 Conclusions 68
4.1 Conclusion 68
4.2 Future Work 69
Chapter 5 Appendix 71
5.1 TG-21 Worksheets 71
5.2 Dose Profiles 74
5.2.1 IMRT_1 74
5.2.2 IMRT_3 77
5.2.3 CyberKnife Trial 80
5.2.4 IMRT Trial 83
5.3 Gamma Analysis 86
5.3.1 IMRT_1 Coronal Films 86
5.3.2 IMRT_1 Sagittal Films 88
5.3.3 IMRT_3 Coronal Films 90
5.3.4 IMRT_3 Sagittal Films 92
5.3.5 CyberKnife Trial Coronal Films 94
5.3.6 CyberKnife Trial Sagittal Films 96
5.3.7 IMRT Trial Coronal Films 98
5.3.8 IMRT Trial Sagittal Films 100

References 102
Vita 105

List of Figures

Figure 1.1 Anthropomorphic QA phantoms: prostate (upper left), thorax (upper right), IMRT head and neck (lower left), SBRT spine (upper middle), SRS head (lower middle), and SBRT liver (lower right) 2

Figure 1.2 RPC phantoms mailed per year 3

Figure 1.3 Diagram of components for measuring OSLD signal. Copied with permission from Thesis defense of Kevin Casey 8

Figure 2.1 High-impact polystyrene spherical phantom (left), and phantom base and insert holding the OSLD within the spherical phantom (right) 10

Figure 2.2 Axial CT scans of phantom (left) and patient (right) demonstrating similarity of phantom to patient anatomy 11

Figure 2.3 RPC pelvic phantom shell (left) with dosimetry (middle) and imaging (right) inserts 11

Figure 2.4 Dosimetry insert split into posterior and anterior half (left), and posterior half split into two quarters to show positioning of OSLD and TLD (red circles) at the center of the target (right) .. 12

Figure 2.5 High-impact polystyrene phantom showing section where OSLD placed 13

Figure 2.6 Axial CT image of prostate phantom at the level of simulation isocenter with the target and critical structures as indicated 14

Figure 2.7 Diagram of OSLD and angles for 6 MV coplanar irradiations. Angles irradiated continue around bottom half of OSLD in edge-on orientation every 45°. 19

Figure 2.8 Spherical phantom positioned for 45° OSLD irradiations 19

Figure 2.9 Diagram of OSLD and angles for 18 MV coplanar irradiations 20

Figure 2.10 Diagram of OSLD and angles for 6 MV non-coplanar irradiations 21

Figure 2.11 CyberKnife irradiation of pelvic phantom 22

Figure 2.12 nanoDot OSLD from Landauer, Inc. 27

Figure 2.13 microStar reader, adapter, and control computer 30

Figure 2.14 Cabinet for optical bleaching of OSLD at the RPC 31

Figure 2.15 Setup of microdensitometer used for film scanning 33

Figure 2.16 Diagram of inferior view of the dosimetry insert showing positions of TLD and OSLD active volumes within the target 35

Figure 2.17 Masks applied to a sagittal film before gamma analysis 37

Figure 3.1 Four field isodose coverage (left) and DVH (right) for the prostate phantom. The PTV, prostate, bladder, rectum, and femoral heads are displayed as purple, blue, yellow, green, and pink, respectively. 38

Figure 3.2 IMRT isodose coverage (left) and DVH (right) for prostate phantom. The PTV, prostate, bladder, rectum, and femoral heads are displayed as purple, blue, yellow, green, and pink, respectively. 39

Figure 3.3 VMAT isodose coverage (left) and DVH (right) for prostate phantom. The PTV, prostate, bladder, rectum, and femoral heads are displayed as purple, blue, yellow, green, and pink, respectively. 40

Figure 3.4 CyberKnife isodose coverage (left) and DVH (right) for prostate phantom. The PTV, prostate, bladder, and rectum are displayed as orange, coral, light blue, and green. The left and right femoral heads are represented by the pink and blue contours, respectively. 40

Figure 3.5 OSLD response for coplanar 6 MV spherical phantom irradiations 42

Figure 3.6 OSLD response for coplanar 18 MV spherical phantom irradiations 43

Figure 3.7 OSLD response for non-coplanar 6 MV spherical phantom irradiations 44

Figure 3.8 Angular response of OSLD at 6 MV normalized to response at 0°, error bars represent the coefficient of variation (Kerns *et al.*), copied with permission from AAPM. 45

Figure 3.9 Angular response of OSLD at 18 MV normalized to the response at 0°, error bars represent the coefficient of variation (Kerns *et al*), copied with permission from AAPM. 46

Figure 3.10 TLD and OSLD doses from 3 Gy coplanar pelvic phantom irradiations 47

Figure 3.11 TLD and OSLD doses from the three 6 Gy non-coplanar pelvic phantom irradiations... 48

Figure 3.12 TLD and OSLD doses from 6 Gy institution trials 49

Figure 3.13 Lateral dose profile in coronal plane from IMRT_2 as planned by TPS and measured by film normalized to TLD dose 58

Figure 3.14 Lateral dose profile in coronal plane from IMRT_2 as planned by TPS and measured by film normalized to corrected OSLD dose 58

Figure 3.15 AP dose profile in sagittal plane from IMRT_2 as planned by TPS and measured by film normalized to TLD dose 59

Figure 3.16 AP dose profile in sagittal plane from IMRT_2 as planned by TPS and measured by film normalized to corrected OSLD dose 59

Figure 3.17 Superior-inferior dose profile in sagittal plane from IMRT_2 as planned by TPS and measured by film normalized to TLD dose 60

Figure 3.18 Superior-inferior dose profile in sagittal plane from IMRT_2 as planned by TPS and measured by film normalized to corrected OSLD dose 60

Figure 3.19 IMRT_2 color scale gamma results for coronal film normalized to TLD dose 63

Figure 3.20 IMRT_2 color scale gamma results for coronal film normalized to corrected target OSLD dose..... 63

Figure 3.21 IMRT_2 binary gamma results for coronal film normalized to target TLD dose 64

Figure 3.22 IMRT_2 binary gamma results for coronal film normalized to corrected target OSLD dose..... 64

Figure 3.23 IMRT_2 color scale gamma results for sagittal film normalized to target TLD dose..... 65

Figure 3.24 IMRT_2 color scale gamma results for sagittal film normalized to corrected target OSLD dose..... 65

Figure 3.25 IMRT_2 binary gamma results for sagittal film normalized to target TLD dose 66

Figure 3.26 IMRT_2 binary gamma results for sagittal film normalized to corrected target OSLD dose..... 66

Figure 5.1 Lateral dose profile in coronal plane from IMRT_1 with film normalized to TLD dose .. 74

Figure 5.2 Lateral dose profile in coronal plane from IMRT_1 with film normalized to corrected OSLD dose 74

Figure 5.3 AP dose profile in sagittal plane from IMRT_1 with film normalized to TLD doses 75

Figure 5.4 AP dose profile in sagittal plane from IMRT_1 with film normalized to corrected OSLD dose..... 75

Figure 5.5 Superior-inferior dose profile in sagittal plane from IMRT_1 with film normalized to TLD dose 76

Figure 5.6 Superior-inferior dose profile in sagittal plane from IMRT_1 with film normalized to corrected OSLD dose 76

Figure 5.7 Lateral dose profile in coronal plane from IMRT_3 with film normalized to TLD dose .. 77

Figure 5.8 Lateral dose profile in coronal plane from IMRT_3 with film normalized to corrected OSLD dose 77

Figure 5.9 AP dose profile in sagittal plane from IMRT_3 with film normalized to TLD dose 78

Figure 5.10 AP dose profile in sagittal plane from IMRT_3 with film normalized to corrected OSLD dose 78

Figure 5.11 Superior-inferior dose profile in sagittal plane from IMRT_3 with film normalized to TLD dose 79

Figure 5.12 Superior-inferior dose profile in sagittal plane from IMRT_3 with film normalized to corrected OSLD dose 79

Figure 5.13 Lateral dose profile in coronal plane from CyberKnife trial with film normalized to TLD dose 80

Figure 5.14 Lateral dose profile in coronal plane from CyberKnife trial with film normalized to corrected OSLD dose 80

Figure 5.15 AP dose profile in sagittal plane from CyberKnife trial with film normalized to TLD dose 81

Figure 5.16 AP dose profile in sagittal plane from CyberKnife trial with film normalized to corrected OSLD dose 81

Figure 5.17 Superior-inferior dose profile in sagittal plane from CyberKnife trial with film normalized to TLD dose 82

Figure 5.18 Superior-inferior dose profile in sagittal plane from CyberKnife trial with film normalized to corrected OSLD dose 82

Figure 5.19 Lateral dose profile in coronal plane from IMRT trial with film normalized to target TLD dose 83

Figure 5.20 Lateral dose profile in coronal plane from IMRT trial with film normalized to corrected OSLD dose 83

Figure 5.21 AP dose profile in sagittal plane from IMRT trial with film normalized to TLD dose ... 84

Figure 5.22 AP dose profile in sagittal plane from IMRT trial with film normalized to corrected OSLD dose 84

Figure 5.23 Superior-inferior dose profile in sagittal plane from IMRT trial with film normalized to TLD dose 85

Figure 5.24 Superior-inferior dose profile in sagittal plane from IMRT trial with film normalized to corrected OSLD dose 85

Figure 5.25 IMRT_1 color scale gamma results for coronal film normalized to TLD dose 86

Figure 5.26 IMRT_1 color scale gamma results for coronal film normalized to corrected OSLD dose 86

Figure 5.27 IMRT_1 binary gamma results for coronal film normalized to TLD dose 87

Figure 5.28 IMRT_1 binary gamma results for coronal film normalized to corrected OSLD dose... 87

Figure 5.29 IMRT_1 color scale gamma results for sagittal film normalized to TLD dose..... 88

Figure 5.30 IMRT_1 color scale gamma results for sagittal film normalized to corrected OSLD dose..... 88

Figure 5.31 IMRT_1 binary gamma results for sagittal film normalized to TLD dose..... 89

Figure 5.32 IMRT_1 binary gamma results for sagittal film normalized to corrected OSLD dose 89

Figure 5.33 IMRT_3 color scale gamma results for coronal film normalized to TLD dose 90

Figure 5.34 IMRT_3 color scale gamma results for coronal film normalized to corrected OSLD dose..... 90

Figure 5.35 IMRT_3 binary gamma results for coronal film normalized to TLD dose 91

Figure 5.36 IMRT_3 binary gamma results for coronal film normalized to corrected OSLD dose... 91

Figure 5.37 IMRT_3 color scale gamma results for sagittal film normalized to TLD dose..... 92

Figure 5.38 IMRT_3 color scale gamma results for sagittal film normalized to corrected OSLD dose..... 92

Figure 5.39 IMRT_3 binary gamma results for sagittal film normalized to TLD dose..... 93

Figure 5.40 IMRT_3 binary gamma results for sagittal film normalized to corrected OSLD dose 93

Figure 5.41 CyberKnife trial color scale gamma results for coronal film normalized to TLD dose... 94

Figure 5.42 CyberKnife trial color scale gamma results for coronal film normalized to corrected OSLD dose 94

Figure 5.43 CyberKnife trial binary gamma results for coronal film normalized to TLD dose..... 95

Figure 5.44 CyberKnife trial binary gamma results for coronal film normalized to corrected OSLD dose..... 95

Figure 5.45 CyberKnife trial color scale gamma results for sagittal film normalized to TLD dose ... 96

Figure 5.46 CyberKnife trial color scale gamma results for sagittal film normalized to corrected OSLD dose 96

Figure 5.47 CyberKnife trial binary gamma results for sagittal film normalized to TLD dose 97

Figure 5.48 CyberKnife trial binary gamma results for sagittal film normalized to corrected OSLD dose..... 97

Figure 5.49 IMRT trial color scale gamma results for coronal film normalized to TLD dose..... 98

Figure 5.50 IMRT trial color scale gamma results for coronal film normalized to corrected OSLD dose..... 98

Figure 5.51 IMRT trial binary gamma results for coronal film normalized to TLD dose..... 99

Figure 5.52 IMRT trial binary gamma results for coronal film normalized to corrected OSLD dose..... 99

Figure 5.53 IMRT trial color scale gamma results for sagittal film normalized to TLD dose 100

Figure 5.54 IMRT trial color scale gamma results for sagittal film normalized to corrected OSLD dose..... 100

Figure 5.55 IMRT trial binary gamma results for sagittal film normalized to TLD dose 101

Figure 5.56 IMRT trial binary gamma results for sagittal film normalized to corrected OSLD dose..... 101

List of Tables

Table 2.1 RPC Prostate IMRT normal tissue constraints 15

Table 3.1 Angular correction factors and standard deviations from spherical phantom irradiations .. 46

Table 3.2 Ion chamber measurements in slab phantom at depth of 10 cm for 6 MV and 18 MV photon beams..... 50

Table 3.3 Energy correction factors for OSLD in full phantom conditions 52

Table 3.4 TLD to OSLD dose ratios for coplanar treatment plans..... 53

Table 3.5 TLD to corrected OSLD dose ratios for coplanar treatment plans 54

Table 3.6 TLD to OSLD dose ratios for CyberKnife treatments..... 54

Table 3.7 TLD to corrected OSLD dose ratios for CyberKnife treatments..... 55

Table 3.8 TLD to OSLD dose ratios for the institution trials 55

Table 3.9 TLD to corrected OSLD dose ratios for the institution trials 55

Table 3.10 Percent of pixels passing gamma analysis for IMRT deliveries in the coronal and sagittal films for a criteria of 7%/4 mm for film normalized to TLD dose and corrected OSLD dose 62

Table 3.11 Percent of pixels passing gamma analysis for institution trials in the coronal and sagittal films for 7%/4 mm criteria for film normalized to TLD dose and corrected OSLD dose..... 62

List of Equations

Equation 2.1 Linac MU calculation 18

Equation 2.2 Ratio of dosimeter responses to correct for energy dependence 24

Equation 2.3 TLD dose calculation 25

Equation 2.4 TLD fading correction factor 25

Equation 2.5 TLD linearity correction 26

Equation 2.6 TLD raw dose calculation 26

Equation 2.7 OSLD dose calculation 27

Equation 2.8 Element corrected average reading 27

Equation 2.9 Readings averaged and depletion corrected 27

Equation 2.10 OSLD fading correction factor 28

Equation 2.11 OSLD linearity correction 29

Equation 2.12 OSLD raw dose calculation 29

Equation 2.13 OSLD depletion correction 31

Equation 2.14 Calibration curve for Gafchromic EBT2 film, lot # A05261102 32

Equation 3.1 MU calculation for 6 MV spherical phantom irradiation 41

Equation 3.2 MU calculation for 18 MV spherical phantom irradiation 41

Equation 3.3 Dose rate to muscle at a depth of 10 cm for 6 MV photon beam 50

Equation 3.4 Dose rate to muscle at a depth of 10 cm for 18 MV photon beam 50

Equation 3.5 MU calculation to deliver approximately 100 cGy to OSLD for 6 MV photon beam . 50

Equation 3.6 MU calculation to deliver approximately 100 cGy to OSLD for 18 MV photon beam 51

Equation 3.7 Fading correction factor for dosimeters read 6 days post-irradiation 51

Equation 3.8 Expected dose delivered to OSLD for 6 MV photon beam 51

Equation 3.9 Expected dose delivered to OSLD for 18 MV photon beam 51

Chapter 1 Introduction

1.1 Statement of Problem

The current standard of practice for mailable anthropomorphic quality assurance (QA) phantoms for the purpose of remote audits by the Radiological Physics Center (RPC) includes the use of thermoluminescent dosimeters (TLD) as an absolute dosimeter within the phantom. The TLD have been shown to be able to identify calibration errors greater than 5%, and to have an accuracy similar to ion chamber measurements with a high degree of precision[1]. There are several downsides to using TLD for remote audits, however, including a long wait period following irradiation before being read, temperature and humidity dependence, destruction of signal after a single reading, and a long reading time. The RPC has already made the switch from TLD to optically stimulated luminescence dosimeters (OSLD) in 2010 for remote external beam output monitoring. The benefits of OSLD include lower cost, a shorter wait period following irradiation, simpler readout procedures, minimal energy dependence, they are reusable, can be re-read, and they are not affected by changes in temperature and humidity. The use of OSLD for this purpose has been well studied and validated by the RPC, and under reference conditions, has been shown to agree well with both ion chamber and TLD measurements for both photon and electron irradiations[2]. The switch from TLD to OSLD in the anthropomorphic QA phantoms is also desirable, for the same reasons as stated above. However, the use of OSLD in the RPC's anthropomorphic phantoms has not been studied for evaluation of special treatment techniques, nor for credentialing of institutions to participate in National Cancer Institute (NCI) sponsored clinical trials.

The problem with implementing the OSLD in the anthropomorphic phantoms lies in the angular dependence exhibited by the dosimeters. Kerns *et al.*[3] demonstrated a decreased response of the nanoDot OSL dosimeter of 4% and 3% for 6 MV and 18 MV beams incident parallel to the plane of the dosimeter, respectively. For a radiation treatment with multiple fields at different gantry angles, some or all of the beams could be oriented such that the OSLD demonstrate the decreased angular response. The magnitude of the angular response could potentially be important and should be accounted for in the calculation of dose. This observed under-response of the OSLD was attributed to the non-uniform geometry of the nanoDot dosimeter. A lower fluence of the primary beam is incident on the disk shaped sensitive volume of the dosimeter from an edge-on orientation, which causes the majority of the dose at that orientation to be from scattered photons and low energy Compton electrons. The stopping power ratio of the sensitive material relative to water decreases

with decreasing electron energy, so as compared to the dose deposited in a face-on orientation from higher energy electrons, the dose deposited by the lower energy electrons would be less.

In order to investigate the applicability of the OSLD and their angular dependence for use in the anthropomorphic QA phantoms, the RPC's pelvic phantom was chosen because of its simplicity in design, ease with which it could be modified, and it has been shown to verify treatments with a high level of precision[4]. This study aims to characterize the angular dependence of OSLD in the pelvic phantom for effectively utilizing the dosimeters as a replacement for TLD in the RPC's anthropomorphic quality assurance phantoms.

1.2 Radiological Physics Center

The Radiological Physics Center (RPC) was founded in 1968 and has been continuously funded by the NCI. The mission of the RPC is to ensure that institutions participating in NCI funded cooperative clinical trial groups deliver clinically comparable and consistent radiation therapy treatments. The RPC monitors the radiation therapy programs of each institution by on-site dosimetry reviews and remote audits. The tools for remote audit quality checks include mini-phantoms containing either OSLD or TLD for the purpose of machine output checks, and mailable anthropomorphic QA phantoms.

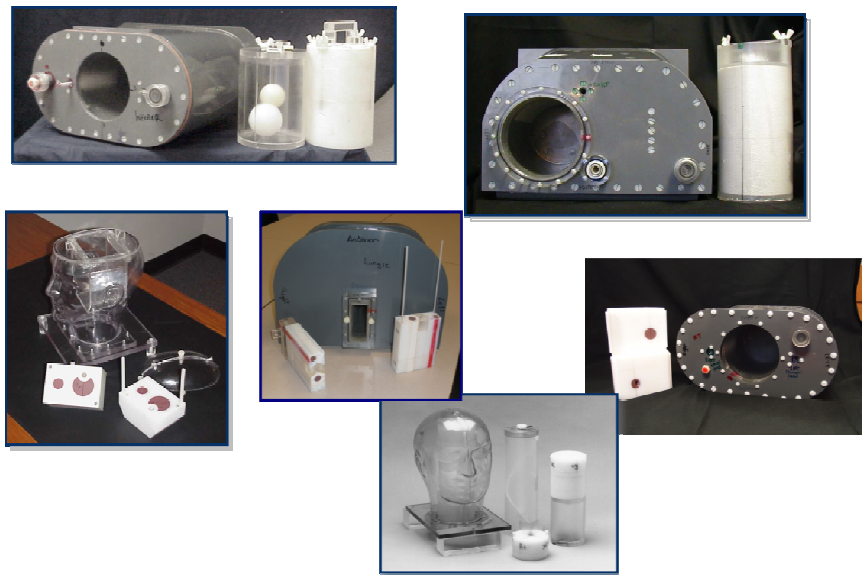

Figure 1.1 Anthropomorphic QA phantoms: prostate (upper left), thorax (upper right), IMRT head and neck (lower left), SBRT spine (upper middle), SRS head (lower middle), and SBRT liver (lower right)

The RPC has five anthropomorphic QA phantom designs, shown above in Figure 1.1: a stereotactic radiosurgery (SRS) head, stereotactic body radiotherapy (SBRT) liver, pelvic-prostate, intensity modulated radiotherapy (IMRT) head & neck, a thorax-lung phantom and an SBRT spine phantom. The QA phantoms are designed to be light-weight and durable for ease of mailing, to have a phantom exterior that approximates the size and shape of the average patient, contain targets as well as organs at risk, heterogeneities, dosimeters to evaluate the treatment delivery, and the phantoms are constructed of materials that simulate patient CT densities[4]. The anthropomorphic QA phantoms assess the radiotherapy treatment process from imaging to dose delivery to achieve a more comprehensive picture of the ability of the institution to deliver dose for special treatment techniques and for credentialing institutions participating in clinical trials. These phantoms were irradiated nearly 500 times last year, as shown in Figure 1.2. Currently, the dosimeters used in the QA phantoms include TLD for absolute point dose measurements in the targets and critical structures, and radiochromic film in two planes of the phantom in order to measure the dose distributions. The dose profiles from the film are normalized to the TLD dose.

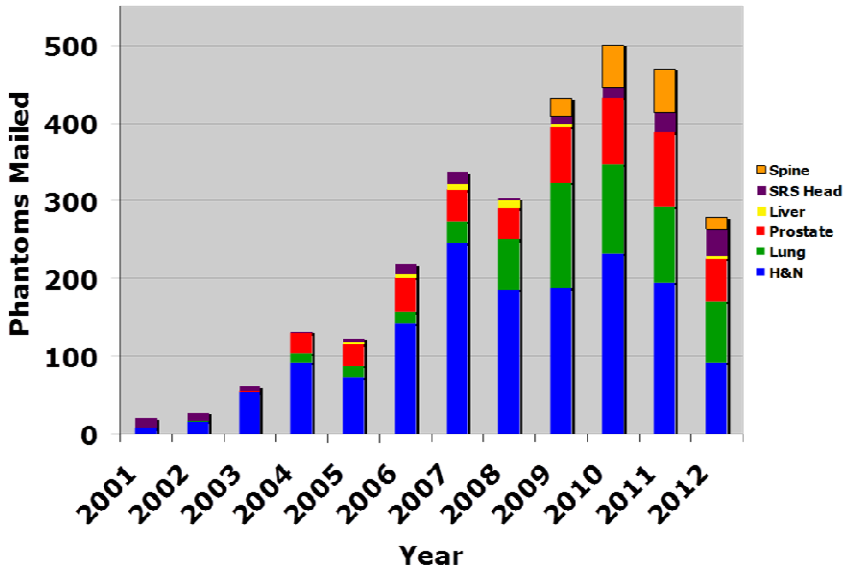

Figure 1.2 RPC phantoms mailed per year

1.3 Optically Stimulated Luminescence

1.3.1 OSL Phenomenon

The phenomenon behind optically stimulated luminescence (OSL) is the same as that behind the TL process, with the stimulation method being exposure to light, rather than the application of

heat. The model consists of two energy levels, the valence and conduction bands, which are separated by a forbidden region. Defects purposefully introduced into the crystalline structure of the material establish local energy levels within the forbidden region, which are called traps. Exposure to ionizing radiation excites the electrons to the conduction band and the holes left behind move to the valence band, creating electron-hole pairs. The electrons that have been excited to the conduction band and the holes in the valence band can move freely within the crystal lattice. The electrons will stay in the conduction band until they move back to the valence band and recombine with a hole, or are captured by an energy trap in the forbidden region[5]. The electrons that have been captured by energy traps cannot recombine with a hole without first being stimulated. Exposing the material to light stimulates the trapped electrons back to the conduction band, from where they can recombine with holes. This recombination of an electron-hole pair creates an excited state of the recombination center, and results in luminescence. A process of hole capture can occur, where a hole in the valence band can combine with an F-center to create additional recombination sites[6].

Depending on the energy level of the trap within the forbidden region, the trap can be either a dosimetric, shallow, or a deep trap. The dosimetric traps are deep enough to keep charge from spontaneously escaping at room temperature, but they are shallow enough that the charge contained can escape by exposing the material to visible light. These dosimetric traps are responsible for the luminescence measured in OSL dosimetry. Ideally, the amount of charge captured within the dosimetric traps is proportional to the absorbed dose of the crystal. Traps that are close in energy to either the conduction band or the valence band are called shallow electron traps and shallow hole traps, respectively. Deep electron traps and deep hole traps also exist within the forbidden region, further in energy from the conduction band for the electron traps, and further from the valence band for hole traps. Yukihara and McKeever[5] describe the influence of charge capture by both the shallow and deep traps on the OSL signal. Shallow traps are associated with phosphorescence directly following irradiation, as well as after exposure to light. Directly following irradiation, charges from shallow traps escape and recombine, releasing luminescence. Phosphorescence after optical stimulation occurs when charges from dosimetric traps escape, but then are captured by shallow traps. Another important process associated with shallow traps is the initial increase in signal intensity when the material is exposed to light. At the beginning of the stimulation, a large number of shallow traps are available and can trap charge coming from the dosimetric traps, but as stimulation continues, these shallow traps become filled and more of the charges escaping from dosimetric traps will recombine and release light. Deep electron and deep hole traps affect the sensitivity of the material by competing with the recombination process, both during irradiation as well as stimulation. The

deep traps may capture charge that has escaped the dosimetric traps, but as the deep traps fill, more electrons recombine and contribute to the OSL signal. This process causes the dosimeter to have a dependence on the history of irradiation, due to a residual signal from previous irradiations that can be difficult to remove from the crystal.

The shape of the luminescence curve versus time can be modeled by an exponential decay, if stimulated by a continuous exposure to light of the appropriate wavelength. The concentration of the shallow and deep traps will affect the OSL curve, but the simplest approach is to assume that the electrons do not fall into another trap after escaping the dosimetric trap, and they are allowed to recombine. The light resulting from the recombination of the electron-hole pair is collected to create the luminescence curve, and the integral of this curve is proportional to the total absorbed dose of the material.

1.3.2 Properties of Al_2O_3:C Dosimeters

The material most commonly used in commercial optically stimulated luminescence dosimeters is carbon-doped aluminum oxide (Al_2O_3:C). This material was originally investigated as a material for thermoluminescence (TL) dosimetry, with approximately 60 times higher TL sensitivity than LiF:Mg,Ti[7], but when it was shown that the TL signal was susceptible to light exposure, the material was implemented as an optically stimulated luminescence dosimeter. A low effective atomic number is a desirable characteristic in a material used for dosimetry; however, the higher effective atomic number of aluminum oxide, 11.28[8], leads to an increase in energy dependence of the dosimeter, especially at lower energies, that must be accounted for if used to be an accurate radiation dosimeter.

Al_2O_3:C can be produced as single crystals, or as powders of varying grain sizes. The crystals are grown in an atmosphere that prevents oxidation keeping the presence of oxygen low, and introducing carbon. This atmosphere creates a high concentration of stable oxygen vacancies and defects in the crystal lattice. When the oxygen vacancy is filled by two electrons, a neutral F-center is created. If the oxygen vacancy is filled with a single electron, a positively charged F^+-center is created. These F and F^+ centers contribute greatly to the luminescence sensitivity of the material, and are present in aluminum oxide in concentrations of 10^{17} cm^{-3} and 10^{15}-10^{16} cm^{-3}, respectively[9]. Electrons that have escaped traps recombine with the F^+-centers, creating excited F-centers, which then relax back to the ground state by emitting luminescence[5,9]. F-center emission is centered at 420 nm with a lifetime of 35 ms at room temperature, and F^+-centers produce luminescence at 330 nm with a much shorter lifetime of less than 7 ns[10].

An advantage of carbon-doped aluminum oxide is the wide energy forbidden region, 9.5 eV[10], which allows the local energy levels in the band gap to be distant enough from the conduction band to be thermally stable. If the gap between the valence and conduction bands is too narrow, the traps are too shallow to hold charge at room temperature for any length of time. Another advantage of the material is its uniformity in sensitivity and properties, due to having a homogeneous mixture of different crystal sizes[5]. The main disadvantage of the material is the residual charge that is stored in the deep traps, which need more than optical bleaching to be removed. According to Reft[11], for absorbed doses up to 2 Gy, optical bleaching will remove virtually all the signal without changing the sensitivity of the material, but for doses above 2 Gy, annealing with fluorescent lights does not remove all trapped charges. However, annealing with a tungsten-halogen lamp (THL) for 3 minutes will remove the signal. It has also been shown that annealing the dosimeters with high temperatures will empty the traps of all charges[12], but dosimeters enclosed in plastic cannot withstand the high temperatures necessary.

The response and measured signal is dependent on characteristics of the material and the reader system, such as energy dependence, fading, linearity, and depletion. The Al_2O_3:C dosimeter characteristics have been previously studied, and will be briefly outlined here. The energy dependence of the OSLD was investigated in Viamonte *et al.*[13], and it was shown that when dosimeters are calibrated using a ^{60}Co beam there is a 4% decrease in the sensitivity for higher energies, making it necessary to apply a correction factor. The response of the OSLD has been shown to have no dependence on dose rate[13,14]. Jursinic[15] investigated the changes in the dosimetric characteristics of the OSLD with accumulated dose, finding that dosimeters with greater accumulated dose experience a greater degree of supra-linearity. He suggested that dosimeters that are to be used multiple times, repeating the cycle of annealing, irradiating and reading, could make measurements with high precision if the individual OSLD are characterized after each annealing to account for changes with accumulated dose. Aguirre *et al.*[16] have reported that the characteristics of individual dosimeters need not be investigated after each annealing, and is independent of the number of cycles it has been irradiated and annealed, provided the accumulated dose to the dosimeter is less than 10 Gy. It has been shown that up to an accumulated dose of 20 Gy, the sensitivity of the OSLD remains the same, but above 20 Gy the sensitivity decreases by approximately 4% with every 10 Gy additional accumulated dose[11,17]. The linearity of the OSL response for an irradiation has been studied extensively, and it has been shown that the response of the dosimeter is linear up to a delivered dose of approximately 2 - 4 Gy[11,13,14,17,18], with supra-linearity observed at higher doses. An explanation

for the observed supra-linearity was given by Jursinic[17], attributing the response to the competition of the deep traps described in Section 1.3.1.

An initial rapid decay of the signal that has been observed in OSLD, called the transient signal, is due to spontaneously escaping charges from the shallow traps without optical stimulation. The decay of the transient response affects the initial intensity of the signal, but does not greatly affect the total area under the luminescence versus time curve[19]. Several studies have shown that after 8 minutes, the transient signal has decayed and the signal is stable[11,17,20]. Perks *et al.*[20] reported a 2% decay in the signal from 10 minutes to 60 hours post-irradiation, and Jursinic[17] observed stability in the signal to be within 2% at 2.5 days after irradiation. Viamonte *et al.*[13] reported no loss of signal within the first six hours after irradiation, a 2 % signal loss within the first five days, and a stable signal from five days to 21 days post-irradiation. Schembri and Heijmen[14] observed a fading of the OSL signal of less than 1.8% over a 3 week time period. Needless to say, the fading characteristics of the OSLD have been studied exhaustively and the conclusion is that this effect should be accounted for in the measurement of dose.

The temperature dependence of the OSL has also been investigated and was shown to not affect the response of the dosimeters for a temperature range of 10° to 40 °C[17]. Each reading of a dosimeter decreases the stored charge by a finite amount. A depletion of the OSL signal with each reading of 0.05% has been reported[17], and other works have suggested that 0.2% of the signal is lost with each reading[13,16].

Jursinic[17] found that when OSL are used repeatedly, going through many cycles of irradiation, reading, and annealing, the measurement uncertainty was 0.6%, demonstrating an improvement in the precision over using the dosimeter a single time. He reported that for the single-use method, the measurement uncertainty was 0.9%. Yukihara *et al.*[18] reported a similar level of uncertainty, 0.7%, for dosimetry in radiotherapy using Al_2O_3:C dosimeters. The reported uncertainty was for the readout of a single dosimeter, and the uncertainty for the readout of more than one dosimeter would decrease with the square root of the number of dosimeters read.

1.3.3 Measurement of OSL Signal

The components necessary to stimulate and capture luminescence in OSLD include a light source, filters, and a photomultiplier tube (PMT), as shown below in Figure 1.3. The light source is used to stimulate the trapped charges, and a filter is necessary for the stimulation light to select the appropriate wavelengths of light. The filtered light incident upon the dosimeter provides the energy

necessary for the trapped charges to escape and recombine, releasing luminescence. Light in the blue wavelengths has been found to be the most efficient for stimulating Al_2O_3:C dosimeter luminescence, but green light is used instead so that the stimulation light is discernible from the F-center emission at 420 nm[10]. Both the stimulation light and the luminescence from the relaxation of the excited F-center pass through another filter prior to entering the PMT in order to remove the stimulation photon component. The emitted luminescence enters the PMT, where it is multiplied and counted.

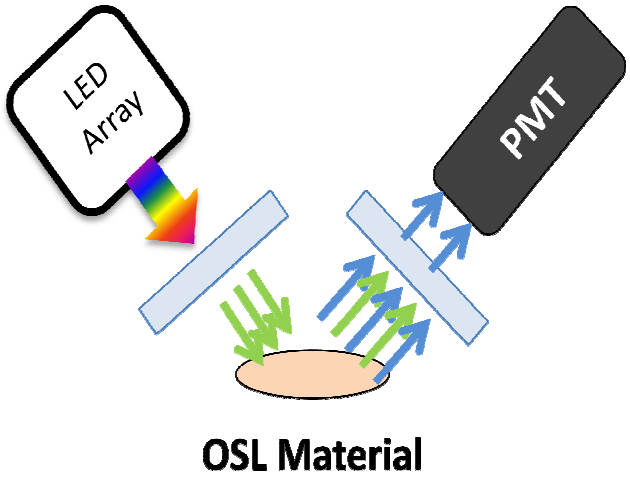

Figure 1.3 Diagram of components for measuring OSLD signal. Copied with permission from Thesis defense of Kevin Casey.

Several stimulation methods have been investigated to induce luminescence, including continuous-wave OSL (CW-OSL) and pulsed OSL (POSL). CW-OSL is the easiest stimulation method and recommended most frequently. This method is performed by exposing the dosimeter to a constant light intensity while collecting the stimulated luminescence. POSL is accomplished by exposing the material to short pulses of stimulation light with a high pulse frequency. The emitted luminescence is then measured in between the light pulses, and not during[21]. This method no longer necessitates discrimination between the stimulation and emitted light, so less filtration is needed before the PMT. This technique requires an understanding of the material and the luminescence, so that appropriate timing can be selected in order to detect most of the emitted signal and at the same time avoid the stimulation light. The signal collected from the dosimeter is integrated over many pulses, and if this method is performed over a longer period, the luminescence versus time curve approximates the luminescence versus time curve for CW-OSL[5].

Measurement of the OSL signal can be made using the initial OSL intensity or the total OSL signal. The initial intensity is determined using only a short exposure to the stimulation light, on the

order of a second. Total OSL signal is determined by stimulating all the trapped charges in the material, and this process can take a much longer time. Yukihara and McKeever[5] state that the choice of measurement technique should not matter, but that the initial OSL intensity is dependent upon the stimulation power and is vulnerable to fluctuations in the power.

1.4 Hypothesis and Specific Aims

We hypothesized that the incorporation of OSLDs into the RPC phantoms, regardless of their angular dependence, will measure on average equivalent dose measurements as compared to the existing TLD measurements within ± 1%.

This hypothesis was tested with the following specific aims:

1. A dosimetry insert for the RPC pelvic phantom was modified to accommodate OSLD and TLD adjacent to the planes of film.
2. Treatment plans of increasing angular beam delivery for the pelvic phantom were developed.
3. Each developed treatment plan was delivered three times to the pelvic phantom, containing two TLD and two OSLD (oriented in the transverse plane) at the center of the PTV, in addition to radiochromic film for the IMRT treatments.
4. The dose measurements from the TLD and OSLD were compared to determine dose measurement equivalency, and whether an angular dependence correction factor was needed.

Chapter 2 Methods and Materials

2.1 Phantoms

2.1.1 Spherical Phantom

A spherical phantom was designed and constructed in order to investigate, under the simplest of circumstances, the magnitude of the response of the OSLD at varying angles. The 10 cm diameter phantom pictured on the left in Figure 2.1 is made of high-impact polystyrene, with the center of the OSLD nano-cassette positioned at the center of the sphere. A cylinder of 1 cm diameter was milled from the base of the sphere, and an insert of the same diameter was made to fit in that space. The cylindrical insert has a slot at the top for holding the OSL at the center of the phantom, and is attached to a flat base as shown on the right in Figure 2.1, which has a pin designed to fit into a corresponding hole on the phantom for reproducible positioning of the OSL.

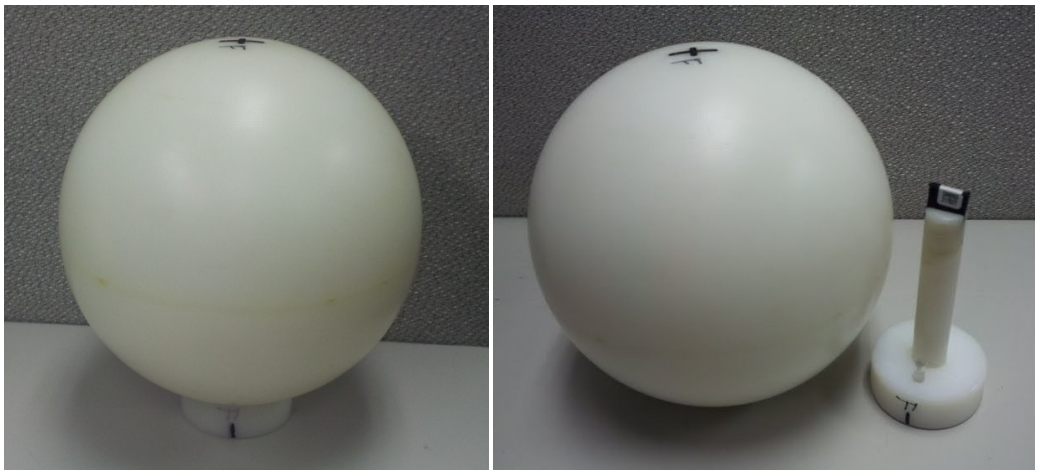

Figure 2.1 High-impact polystyrene spherical phantom (left), and phantom base and insert holding the OSLD within the spherical phantom (right)

2.1.2 RPC Pelvic Phantom

The RPC's pelvic phantom was used for this study, which was designed for remote audits and credentialing of institutions for participation in clinical trials. The phantom shell is made of PVC, can be filled with water to simulate soft tissue, and is made to estimate the average size and shape of patients and organs of interest in the treatment of the prostate as seen in Figure 2.2.

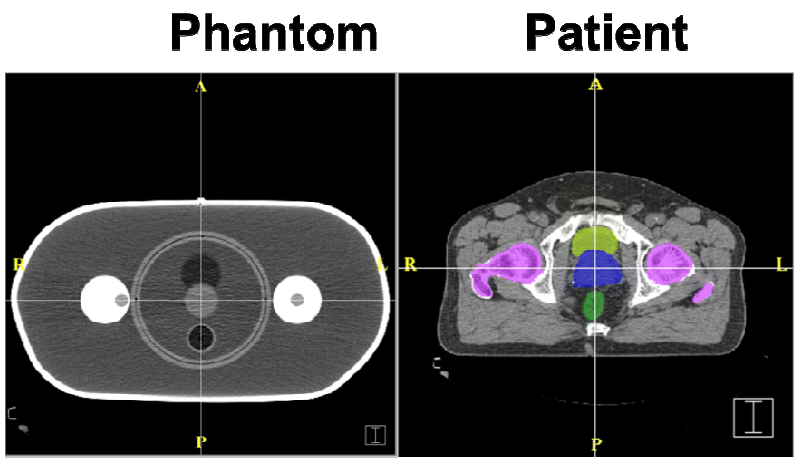

Figure 2.2 Axial CT scans of phantom (left) and patient (right) demonstrating similarity of phantom to patient anatomy

The shell contains polybutylene terephthalate (PBT) – polyester cylinders to simulate the femoral heads, each containing a hollow tube for the insertion of acrylic femoral head rods. There are two imaging rods made of solid acrylic, and two dosimetric rods, each of which contains a hollow space for the positioning of a TLD capsule at the level of the target. At the base of the pelvic phantom, a large diameter tube allows for the placement of the imaging and dosimetric inserts, both locking into place within the tube, as seen in Figure 2.3. For the CyberKnife irradiations, four gold fiducials were placed along the large tube for motion tracking with the orthogonal x-ray imaging system used during CyberKnife treatments.

Figure 2.3 RPC pelvic phantom shell (left) with dosimetry (middle) and imaging (right) inserts

The imaging insert of the phantom contains both a target and organs at risk, made of materials to approximate patient tissue densities and CT numbers. A spherical nylon ball was used for the prostate, a polyethylene ball for the bladder, and a cylinder of wax surrounded by a thin polyethylene tube was used for the rectum and rectal wall. The dosimetry insert is made of high-impact polystyrene, and the cylinder breaks into four quarters for loading dosimeters as seen below in Figure 2.4. Within the target volume of the dosimetry insert, there are two TLD and it was modified to hold an additional two OSLD in the axial plane. The insert also contains film in both the coronal and sagittal planes, which are pricked by pins mounted in the insert in spots unique to the phantom, and these pin pricks are used for the registration of the film, discussed later in Section 2.6.2.

Figure 2.4 Dosimetry insert split into posterior and anterior half (left), and posterior half split into two quarters to show positioning of OSLD and TLD (red circles) at the center of the target (right)

2.1.3 Slab Phantom

The energy dependence of OSLD in full phantom conditions had not yet been characterized by the RPC, so the phantom seen below in Figure 2.5 was used to perform irradiations to determine a full phantom energy-dependence correction factor for OSLD. The phantom is made of 15 x 15 cm^2 slabs of high-impact polystyrene, each 2 cm thick, with the exception of one 3 cm thick slab. One slab contained a section in the middle that could slide out and hold a TLD at the center. A new sliding section was made to the exact dimensions of the previous section holding the TLD, but instead was made to hold an OSLD nano-cassette centered within the slab. A piece of high-impact polystyrene was then placed on top of the OSLD to eliminate any air gap within the phantom. A single OSLD was placed at a depth of 10 cm. Beyond the depth of the OSLD, there was 7 cm of high-impact polystyrene to provide sufficient backscatter. Another 2 cm thick section of the phantom contained a cylinder bored out of the center to insert an ionization chamber.

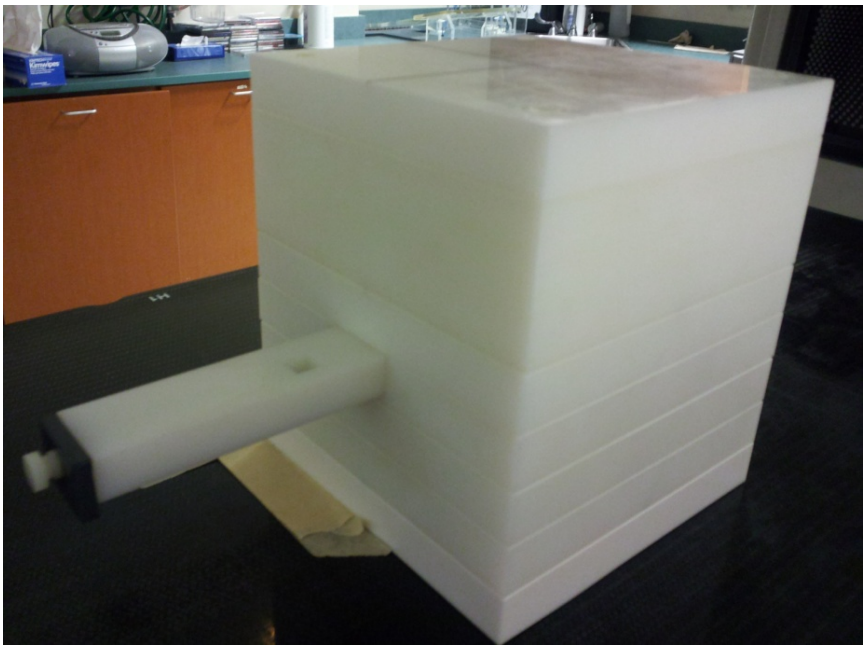

Figure 2.5 High-impact polystyrene phantom showing section where OSLD placed

2.2 Treatment Planning

2.2.1 Phantom Simulation

The CT images were acquired using a GE LightSpeed RT16 scanner (GE Healthcare, Waukesha, WI). The phantom shell and dosimetry insert were filled with water, and the acrylic imaging rods were placed in the femoral heads. The phantom was placed on the imaging couch in the supine position, in a head first orientation. The lasers were aligned to place the isocenter near the center of the prostate. The laser lines were marked with tape on the anterior, left, and right sides of the phantom. Radio-opaque markers (bb's) were placed at the laser crosshairs to mark isocenter. A typical MD Anderson prostate protocol was used for the CT simulation, and the resulting images were imported into the Pinnacle treatment planning system for the three co-planar treatments. The pelvic phantom was then imaged on a GE LightSpeed RT16 Xtra scanner at St. Luke's Episcopal Hospital Radiation Therapy and CyberKnife Facility using the same setup procedure and a similar scanning protocol, for developing the CyberKnife treatment plan. The resulting images were imported into Accuray's MultiPlan (Accuray, Sunnyvale, CA) treatment planning system.

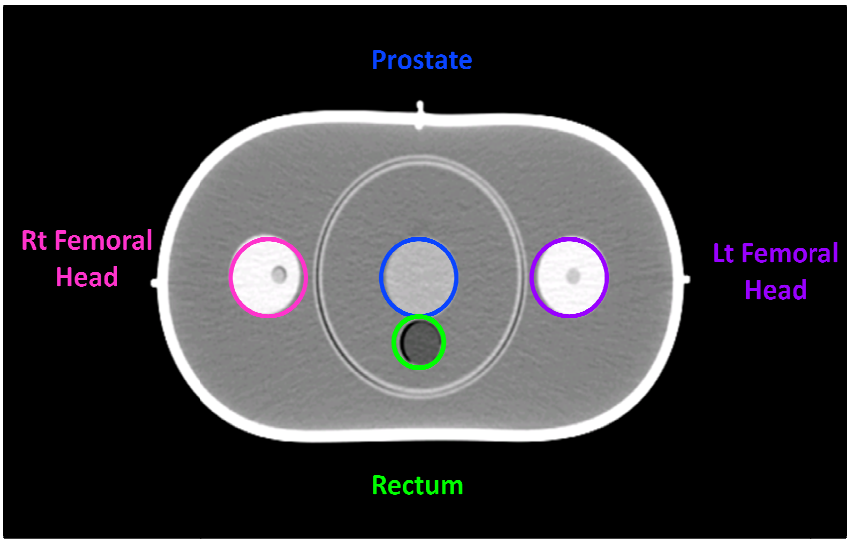

Figure 2.6 Axial CT image of prostate phantom at the level of simulation isocenter with the target and critical structures as indicated

An axial slice of the phantom at the level of the center of the target is shown in Figure 2.6. The bb placement, indicating isocenter, can be seen on the anterior, right and left sides of the phantom in the image.

2.2.2 Dose Prescription

The dosimetric guidelines for this study are based on the dose prescription and constraints set by the RPC Prostate IMRT credentialing protocol. The protocol specifies that at least 98% of the PTV receives a dose of 6 Gy, and a maximum dose of 6.4 Gy may be delivered to less than 2% of the PTV. The bladder, rectum and femoral heads are the critical normal structures, and must not receive more than 6.7 Gy. The normal structure constraints are listed in Table 2.1.

Structure	Dosimetric Constraints
Bladder	$V_{5.7\ Gy} < 50\%$
	$V_{6.0\ Gy} < 35\%$
	$V_{6.3\ Gy} < 25\%$
	$V_{6.7\ Gy} < 15\%$
Rectum	$V_{5.0\ Gy} < 50\%$
	$V_{5.7\ Gy} < 35\%$
	$V_{6.0\ Gy} < 25\%$
	$V_{6.3\ Gy} < 15\%$
Femoral Heads	Maximum dose $\leq$ 6.7 Gy

Table 2.1 RPC Prostate IMRT normal tissue constraints

2.2.3 Planning Procedures

Treatment planning was performed on Pinnacle v9.0 (Phillips Medical, Madison, WI) and MultiPlan v3.5.3 (Accuray, Sunnyvale, CA). The couch was removed from the images, and the treatment isocenter was identified at the intersection of the simulation bb's. Contours were created for the prostate, bladder, rectum and femoral heads manually using the region of interest (ROI) tool. Contours were also created for the TLD in the target and femoral heads, as well as for the OSLD in the target. The external tissue was contoured using the auto-contour function. Using guidelines set by MD Anderson's Genitourinary (GU) Service, several planning structures were created. The prostate was expanded by 7 mm in all directions, with the exception of a 5 mm posterior expansion, to create the PTV. An additional 5 mm margin was added to the PTV to create a structure called 'PTV expand'. A structure for the normal tissue was created by removing the volume 'PTV expand' from the external tissue. Additional planning structures were created, including a 1 cm expansion of the PTV, which could be used to achieve coverage of the target, and a rectum avoid structure to bring the dose off the anterior wall of the rectum. The rectum avoid structure was created by subtracting the structure 'PTV expand' from the contoured rectum.

Four treatment plans of increasing angular beam delivery were created for the pelvic phantom using common dose prescriptions and constraints described in Section 2.2.2.

2.2.3.1 Four Field Box

Four coplanar beams were created for this plan, each using 18 MV photons. The anteroposterior (AP) beam had a gantry angle of 0°, a gantry angle of 180° was used for the posteroanterior (PA) beam, and gantry angles of 90°and 270° were used for the left lateral and right lateral beams, respectively. The jaws were set to achieve adequate coverage of the PTV, while minimizing the dose to the normal tissue. The couch and collimator angles were set to 0° for all beams. The dose grid encompassed the phantom, and used a resolution of 0.4 cm^3. The final dose was computed using the collapsed cone (CC) convolution algorithm.

2.2.3.2 IMRT

The typical beam arrangement for prostate IMRT at MD Anderson uses eight 6 MV photon coplanar beams, with the following gantry angles: 225°, 260°, 295°, 330°, 30°, 65°, 100°, and 135°. The couch and collimator angles were set to 0° for all beams. The dose grid encompassed the phantom and a resolution of 0.4 cm^3 was used. Initially, each beam was set to be equally weighted and unlocked. Direct Machine Parameter Optimization (DMPO) was used for the inverse planning, and was set to allow the computer to set the field size. The objectives for the plan focused foremost on achieving target coverage, achieving the dose constraints to the critical structures, and finally, the normal tissue objective was set to deliver a maximum of half the prescription dose to 1% of the volume. The plan was normalized to 97% of the prescribed dose to achieve PTV coverage. The final dose calculation was computed using the CC convolution algorithm.

2.2.3.3 VMAT

Two arcs were created using the dynamic arc beam type in Pinnacle, allowing for variable gantry rate, MLC leaf speed, and dose rate. The couch angle was set to 0° and 6 MV photons were used for both arcs. The dose grid covered the entire phantom and used a resolution of 0.4 cm^3. Each beam was given equal weight, with the first arc beginning at a gantry angle of 181° and rotating to 180° in a clockwise (CW) motion with a 30° collimator angle. The second arc rotated from 180° to 181° in a counter-clockwise (CCW) motion with a 330° collimator angle. SmartArc optimization was used, and the computer was allowed to set the field size. The optimization generated a new control point every 4 degrees, and the leaf motion was constrained to prevent the MLC from attempting to move too quickly. The objectives for the plan were similar to those used for the IMRT optimization, the most important being target coverage, then trying to meet critical structure dose constraints, and

minimizing the dose to the normal tissue. The plan was normalized to 96% of the prescribed dose to achieve PTV coverage. Final dose was calculated using the CC convolution algorithm.

2.2.3.4 CyberKnife

Using Accuray's MultiPlan v3.5.3 inverse treatment planning system, a CyberKnife plan was created. The CyberKnife Robotic Radiosurgery System (Accuray, Sunnyvale, CA) utilizes a 6 MV compact linear accelerator mounted on a robotic arm, and delivers pencil beams at discrete nodes surrounding the patient. The beam can be collimated by using either a set of interchangeable circular collimators, or the Iris™ Variable Aperture Collimator. The plan for this study used the Iris collimator, and limited the cone sizes used from 25 mm up to 60 mm. The dose grid encompassed the phantom, and a high-resolution dose grid was used during the final dose calculation, which performs calculations for every voxel in the CT image set. The objectives for the plan were the same as those used for the IMRT optimization, the most important being target coverage and meeting critical normal structure constraints. A minimum number of MU per beam was set. The ray-tracing algorithm was used for the final dose calculation, and the plan was normalized to 90% of the prescribed dose. Sharma *et al.*[22] briefly describes the ray-tracing algorithm method. This dose model uses a combination of off-axis ratios (OAR), tissue-phantom ratios (TPR), collimator output factors (OF), and central-axis effective depth calculations to correct for the patient geometry and tissue heterogeneities.

2.3 Phantom Irradiations

2.3.1 Spherical Phantom Irradiations

Irradiations were performed using the spherical phantom described in Section 2.1.1, to investigate the angular response of the OSLD under the simplest of circumstances for 6 MV and 18 MV photon beams. The irradiations were delivered on a Varian 21EX linear accelerator (Varian Medical Systems, Palo Alto, CA) calibrated using the AAPM TG-51 protocol[23] and operated in service mode. The phantom was centered on the central axis (CAX) of the beam, and the top of the phantom was set to 95 cm SSD. The field size was set to 5 x 5 cm^2, and the collimator angle was 0° throughout the irradiation of this phantom. The monitor units (MU) needed to deliver 100 cGy to the OSLD was calculated using Equation 2.1:

$$MU = \frac{D}{k \cdot DF \cdot S_C \cdot S_P \cdot OAF \cdot AF}$$

Equation 2.1 Linac MU calculation

where D is the prescribed dose per field in cGy, k is the cGy/MU under the reference calibration conditions. DF is the depth factor (PDD for SSD techniques or TMR for SAD techniques), S_C and S_P are the collimator scatter and phantom scatter factors, OAF is the off-axis factor, and AF is an attenuation factor, representing any beam attenuators such as wedges or trays.

The positioning of the phantom was checked periodically throughout the irradiations. Three sets of irradiations were performed using the spherical phantom, two coplanar irradiations using beam energies 6 MV and 18 MV, and one non-coplanar irradiation with a 6 MV photon beam.

The dose delivered to each OSLD was calculated using Equation 2.7. The OSLD calculated dose was normalized for all edge-on angles to the face-on angle. The dose calculated to each dosimeter was normalized to the average dose to the dosimeters irradiated at the face-on angle. A statistical analysis of these normalized doses was performed to determine if the response of the OSLD at the face-on angle was different from the responses at the edge-on angles. A one-way analysis of variance (ANOVA) test was performed, which is used to compare the means of two or more groups, with the normalized dose as the dependent variable and the angle as the factor. The null hypothesis states that the samples in these multiple groups are drawn from the same population. A p-value less than α=0.05 indicated that the null hypothesis could be rejected and the group means were significantly different. After performing the one-way ANOVA, if the null hypothesis was rejected, a Fisher's Least Significant Difference (LSD) test was run to determine which means are statistically significantly different from each other. This test compares the mean of one group with the mean of another group using a series of t-tests, the null hypothesis stating that the means of the two groups are equal.

2.3.1.1 Coplanar 6 MV Irradiations

The first set of irradiations were delivered with a 6 MV photon beam. The OSLD response with the beam incident normally on the face of the dosimeter (face-on) was compared to the response of the dosimeter at varying beam angles in an edge-on orientation around the dosimeter. The angles with respect to the OSLD can be seen below in Figure 2.7. The edge-on irradiations were done in 45° increments around the dosimeter, from 0° to 315°. For the irradiation of the angles on the inferior

half of the dosimeter (225°, 270°, and 315°), the OSLD was rotated 180° within the phantom to measure the response of the dosimeter without the influence of the treatment couch and rails.

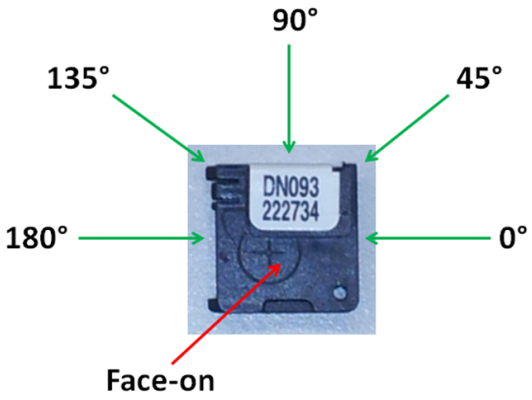

Figure 2.7 Diagram of OSLD and angles for 6 MV coplanar irradiations. Angles irradiated continue around bottom half of OSLD in edge-on orientation every 45°.

Three OSLD were irradiated at each angle, and the average response at each angle was normalized to the average response at the face-on angle. For the face-on irradiation, both the gantry and the couch were set at 270°. For all other angles, the couch rotation was set to 0° and the gantry was rotated about the phantom. The setup for the 45° irradiation is shown below in Figure 2.8.

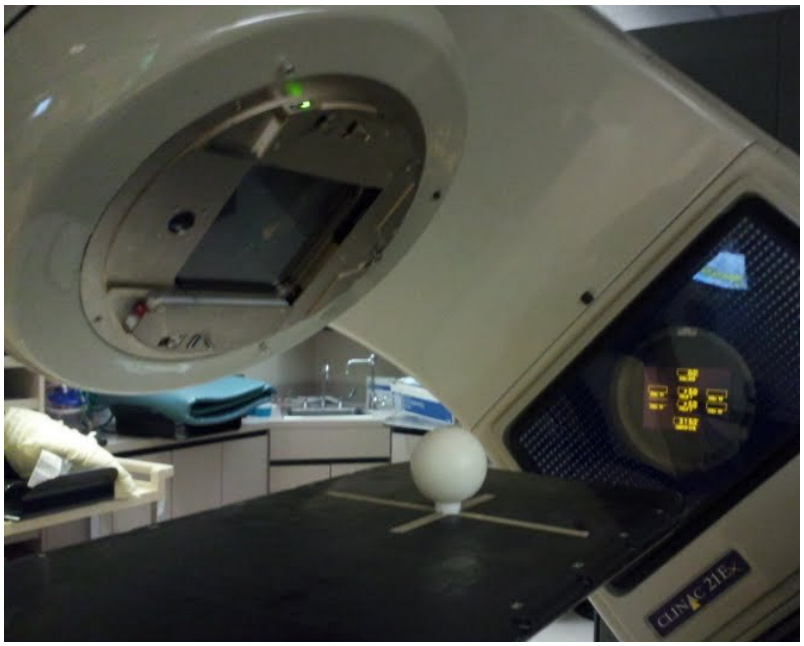

Figure 2.8 Spherical phantom positioned for 45° OSLD irradiations

2.3.1.2 Coplanar 18 MV Irradiations

The second set of spherical phantom irradiations were performed using an 18 MV photon beam, and the response of the OSLD in the face-on orientation was compared to the response of several angles around the dosimeter in the edge-on orientation. The OSLD angles irradiated can be seen in Figure 2.9. The edge-on irradiations were performed every 90° around the dosimeter.

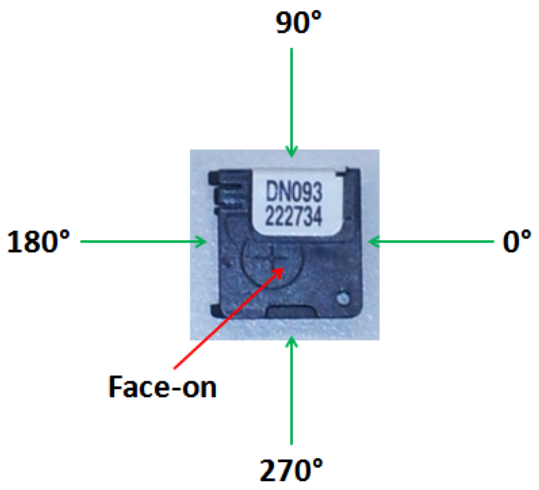

Figure 2.9 Diagram of OSLD and angles for 18 MV coplanar irradiations

Three OSLD were irradiated at each angle, and the average response for each edge-on angle was normalized to the average response for the face-on irradiation. The gantry and couch angles used for the coplanar 6 MV irradiations discussed in Section 2.3.1.1 were also used for this set of irradiations. For the angle on the inferior half of the dosimeter (270°), the OSLD was again rotated within the phantom to eliminate the effects of the treatment couch and rails.

2.3.1.3 Non-coplanar 6 MV Irradiations

The final set of spherical irradiations was designed to simulate a cone of beam angles similar to the angles that might be delivered in a prostate CyberKnife treatment. The irradiations were performed using a 6 MV photon beam. The response of the dosimeter at varying irradiation angles was normalized to the response of the OSLD in the face-on orientation. The angles irradiated can be seen in Figure 2.9. The angles investigated in the coplanar beam orientation ranged from 0° to 180°, as seen on the left in Figure 2.10. In the non-coplanar beam arrangement, a 90° range of angles centered about the top of the OSLD were investigated, with irradiations every 15° as seen on the right

in Figure 2.10. Three OSLD were irradiated at each angle. The couch rotation was set to 0° for all angles, and the gantry was rotated about the phantom.

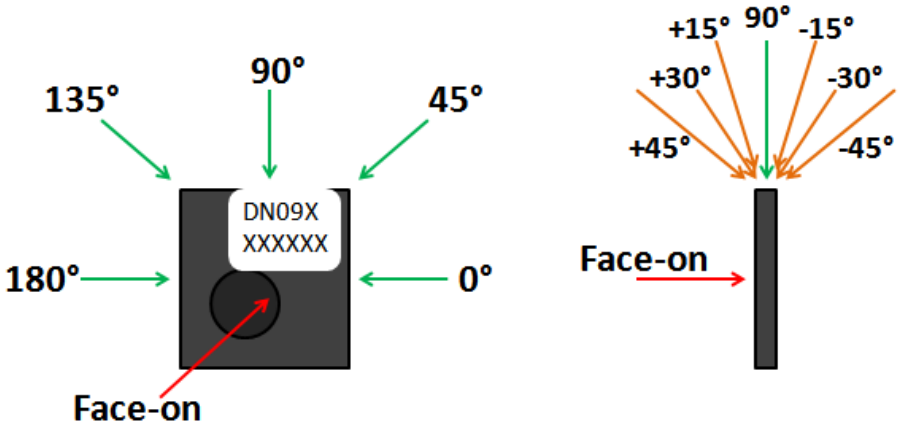

Figure 2.10 Diagram of OSLD and angles for 6 MV non-coplanar irradiations

2.3.2 Pelvic Phantom Irradiations

To study the angular dependence of the OSLD in full phantom conditions for treatment plans of increasing angular beam delivery, the pelvic phantom described in Section 2.1.2 was irradiated. The four treatment plans of increasing angular beam delivery are discussed in Section 2.2.3, consisting of three coplanar treatments (4-field box, IMRT, and VMAT) and one non-coplanar treatment (CyberKnife). The coplanar treatment plans were delivered on a Varian 21EX linear accelerator calibrated using the AAPM TG-51 protocol. The non-coplanar treatment was delivered on the CyberKnife G4 Robotic Radiosurgery System at St. Luke's Radiation Therapy and CyberKnife facility in Houston, TX as shown below in Figure 2.11. Each plan met the dose prescription and critical normal tissue constraints outlined in Section 2.2.2, planned to deliver a target dose of 6 Gy. The OSLD batch 06K10 used in this study was only commissioned for linearity corrections up to a dose of 3.5 Gy, so the coplanar treatment plans were scaled to deliver a target dose of 3 Gy. The new OSLD batch, 16K12 was then commissioned at the RPC to higher dose levels, allowing the original dose prescription to be met. The CyberKnife treatment and the institution trials, discussed later in Section 2.3.2.1, incorporated the new 16K12 OSLD batch, so the original dose prescription of 6 Gy was maintained for these deliveries.

Figure 2.11 CyberKnife irradiation of pelvic phantom

For the treatment plans delivered on the Varian 21EX linacs, the phantom was positioned at the head of the couch in the head first, supine orientation. The lasers were aligned to the simulation isocenter using the bb's and the tape marks, and the positioning of the phantom was checked periodically throughout the treatment delivery. The positioning of the phantom for the CyberKnife treatment delivery was accomplished using the fiducials implanted within the phantom shell and the CyberKnife's image guidance system. The positions of the fiducials are at known coordinates within the phantom. The image guidance system uses two orthogonal fixed x-ray imaging units to image the phantom before and throughout treatment delivery, and these images are compared to previously generated digitally reconstructed radiographs (DRRs) to determine the positioning and target location, and make any necessary adjustments to the phantom position by moving the treatment couch.

Each treatment plan was delivered three times, each time loading new dosimeters into the phantom before the next irradiation. The dosimeters included in each treatment deliver varied by plan. For the 4-field treatment, the dosimeters loaded into the phantom included TLD in the target and femoral heads, and OSLD in the target volume. The same dosimeters were loaded into the

VMAT and CyberKnife treatments as well. For the IMRT deliveries, the dosimeters included TLD and OSLD loaded in the same manner as the other treatments, as well as radiochromic film in both the coronal and sagittal planes through the target volume.

During the delivery of the VMAT treatment plans, the rails of the treatment couch were moved in and out, as the gantry rotated about the phantom. For the delivery of the first arc, with the gantry rotating about the phantom in the clockwise direction, the rails were out between the angles 181° and 220°. At this point, the rails were moved in to the center of the couch as the gantry rotated from 220° to 140°. From 140° to 180°, completing the first arc, the rails were moved back out. The second arc began at 180° and rotated about the phantom in the counter-clockwise direction, and the rails were moved in and out during the same angles as for the first arc. This technique was employed to reduce the effect of the rails on the dose delivered to the phantom.

2.3.2.1 Institution Trials

As an additional check, the RPC pelvic phantom was sent to two institutions for irradiation. For each institution, the phantom was sent according to RPC credentialing protocol, including instructions for simulation, planning, and treatment delivery, and the dosimeters traditionally sent (TLD and radiochromic film). The only change to the standard credentialing process was the inclusion of two OSLD, batch 16K12, within the dosimetric insert, as they had been placed during all previous irradiations of the pelvic phantom. One institution performed the RPC credentialing protocol for prostate IMRT, and the second institution performed a prostate CyberKnife irradiation. Both of these institution trials used the standard RPC prostate dose prescription and normal structure constraints.

2.3.3 Energy Correction Irradiations

Using the slab phantom discussed in Section 2.1.3, a set of irradiations was performed to investigate the energy dependence of the OSLD in full phantom conditions, and determine an energy correction factor. The irradiations were performed on a Varian 21EX linac using 6 MV and 18 MV photon beams. A TG-51 calibration was performed in a large water phantom. The surface of the water in the phantom was set to 100 cm SSD, with a field size of 10 x 10 cm^2, gantry angle of 0° and collimator rotation of 0°. After performing the calibration, the water phantom was replaced with the slab polystyrene phantom with the same setup conditions as for the calibration. Both the calibration and the slab phantom irradiation measurements were made with an Exradin A12 (Standard Imaging, Middleton, WI) ionization chamber calibrated by the MD Anderson Cancer Center ADCL. Within

the slab phantom, the ion chamber was positioned at a depth of 10 cm. Three readings were taken per beam energy, delivering 200 MU per reading.

The readings made for each energy by the ion chamber in the slab phantom at a depth of 10 cm were used to calculate the dose rate (cGy/MU) to muscle at depth using the AAPM TG-21 protocol[24]. The protocol calculates the dose rate to water at the depth of d_{max} from measurements made in a non-water phantom. The dose rate was corrected to dose in muscle using a 0.99 correction, and the depth was corrected from d_{max} to 10 cm using the $\%dd_{10}$ for the Varian 21EX.

An estimate of the MU needed to deliver 100 cGy to a depth of 10 cm within the polystyrene phantom was made by using the percent depth dose (%dd) in water information for the linac at the particular energy. The desired dose was divided by the $\%dd_{10}$ for both 6 MV and 18 MV. Using the slab with the modification for OSLD, a dosimeter was placed at 10 cm depth within the phantom and irradiated to the desired MU. Irradiations were performed for both batches 06K10 and 16K12 OSLD. Five OSLD were irradiated for each batch and energy combination, irradiating 20 nanoDots total. The response of the OSLD positioned at 10 cm depth within the slab phantom was measured for each dosimeter. The ratio of the dosimeter response at the investigated energy weighted by the expected dose delivered to the response from cobalt-60 weighted by its expected dose was found using Equation 2.2 shown below:

$$\frac{E}{^{60}\mathrm{Co}} = \frac{(Avg\ Corr\ Rdg\ \cdot\ K_F\ \cdot\ K_L)_E / D_E}{(Avg\ Corr\ Rdg\ \cdot\ K_F\ \cdot\ K_L)_{^{60}\mathrm{Co}} / D_{^{60}\mathrm{Co}}}$$

Equation 2.2 Ratio of dosimeter responses to correct for energy dependence

The terms *Avg Corr Rdg*, K_F, and K_L are the same as defined in Section 2.5. The term D_E is the expected dose delivered to the dosimeters at the investigated energies (6 MV and 18 MV), which was calculated by multiplying the MU delivered, by the dose rate to muscle at a depth of 10 cm as calculated using TG-21. The terms in the denominator of Equation 2.2 all refer to the OSLD previously irradiated in cobalt-60 as standards and read during the same session as the OSLD irradiated in the slab phantom to establish system sensitivity. The expected dose delivered to the standard dosimeters, $D_{^{60}\mathrm{Co}}$, was calculated using an RPC spreadsheet that accounts for the decay of the source, irradiation setup, and length of irradiation. The linearity correction factor for the dosimeters irradiated to 100 cGy (standards) is defined to be one.

This ratio was calculated for each irradiated dosimeter. Considering setup and calibration errors, we can assume that the irradiations of two batches per energy were actually like irradiations of

the same batch twice. This assumption is valid based on the RPC OSLD mini-phantom experience. The ratios of the dosimeter responses were grouped for the 06K10 and 16K12 batches by energy, and an average ratio was calculated per energy (10 dosimeter ratios per energy). The inverse of the averaged ratios for 6 MV and 18 MV was taken to get the energy correction factors for OSLD in full phantom conditions.

2.4 RPC TLD Dosimetry

The TLD used in this study were double-loaded cylindrical capsules containing LiF TLD-100 powder (Quantaflux, LLC, Dayton, OH) from batch B11, each load containing approximately 20 mg of powder. The RPC has already extensively studied the characteristics of this batch of TLD. The correction factors determined by the RPC are used to calculate the absorbed dose to the TLD using Equation 2.3:

$$Dose = Avg\ Rdg \cdot S \cdot K_F \cdot K_L \cdot K_E$$

Equation 2.3 TLD dose calculation

The term *Avg Rdg* is the average signal measured per unit mass of the powder. The average reading from the powder is multiplied by *S*, the system sensitivity, and several correction factors unique to the TLD batch: K_F, K_L, and K_E. These factors correct for fading (K_F), linearity of the response with dose (K_L), and the energy dependence (K_E) of the dosimeters.

2.4.1 TLD Batch Correction Factors

The fading of the TL signal is corrected using the following equation:

$$K_F = \frac{N}{a \cdot e^{-bX} + c \cdot e^{-dX}}$$

Equation 2.4 TLD fading correction factor

where $N = 1.3493$, $a = 1.2815$, $b = 0.00010885$, $c = 0.067810$, $d = 0.071908$, and X is the number of days since irradiation. The TLD are typically read 14 days after irradiation, but no sooner than day 14.

The RPC protocol for calculating the linearity correction is to perform six iterations of the calculation to arrive at a final linearity correction value. The correction for the linearity of the response with dose, for a range of doses from 1 to 40 Gy, is calculated using Equation 2.5:

$$K_L = a \cdot raw\ dose^2 + b \cdot raw\ dose + c$$

Equation 2.5 TLD linearity correction

For 'low dose' irradiations, the response has been shown to be linear, and the constants for K_L are as follows: a = 0, b = -0.000335, and c = 1.1004995. For 'high dose' irradiations, the response of the dosimeter exhibits supra-linearity, and the constants become a = 2.55207e-8, b = -2.22110e-4, and c = 1.064337. The *raw dose* is calculated using Equation 2.6:

$$raw\ dose = Avg\ Rdg \cdot S \cdot K_F$$

Equation 2.6 TLD raw dose calculation

where the terms *Avg Rdg*, *S*, and K_F are the same as those discussed previously.

The energy correction factors have been measured for each batch of TLD for a range of beam energies for several of the anthropomorphic QA phantoms by the RPC. Energy correction factors for ^{60}Co, 6 MV, and 18 MV photon beams are 1, 1.03, and 1.07, respectively.

2.4.2 System Sensitivity

The dosimetry system is the combination of the dosimeters, phantom, and the reader. The system must be calibrated for each reading session because the reader may experience changes in sensitivity, which is monitored by reading "standards" and "controls". The standard dosimeters are irradiated to a known dose from a cobalt-60 unit, and these dosimeters are read at the beginning and end of a reading to determine the system sensitivity for the session. The system sensitivity, *S*, is defined as the expected dose delivered to the standard dosimeters, divided by the average reading, as well as fading and linearity corrections. The control dosimeters are also irradiated by a cobalt-60 unit, to a different known dose, and are read at the beginning, end, and periodically throughout the session. The purpose of reading the controls is to check the constancy of the system, and track changes in sensitivity over time.

2.5 RPC OSLD Dosimetry

The OSLD used in this study were nanoDot™ dosimeters from the InLight® OSL system (Landauer, Inc., Glenwood, IL). The nanoDot dosimeter contains a 5 mm diameter disk-shaped sensitive volume of Al_2O_3:C, 0.2 mm thick. The disk is enclosed in a light-tight plastic case shown in Figure 2.12, measuring 10 x 10 x 2 mm^3. The position of the sensitive volume is indicated on the

case by the circle with the center marked by the cross hairs. Each dosimeter has a unique barcode that is scanned prior to being read, and allows for the recording of the associated counts.

Figure 2.12 nanoDot OSLD from Landauer, Inc.

The dosimeters are created in batches, and sent to the RPC where the characteristics of the batch and each dosimeter are carefully studied. The dosimeters used in this study came from batches 06K10, and 16K12, named according to RPC convention. The dose to the OSLD is calculated using Equation 2.7:

$$Dose = Avg\ Corr\ Rdg \cdot S \cdot K_F \cdot K_L \cdot K_E$$

Equation 2.7 OSLD dose calculation

The term *Avg Corr Rdg* is the average counts from the reader, accounting for depletion of the signal, multiplied by the element correction factor (*ECF*), as shown below in Equations 2.8 and 2.9. The element correction factor is discussed in Section 2.5.1.

$$Avg\ Corr\ Rdg = Avg\ Rdg \cdot ECF$$

Equation 2.8 Element corrected average reading

Each dosimeter is read three times in a row, making $n = 3$ in Equation 2.9, and all dosimeters from an irradiation session are read in the same reading session.

$$Avg\ Rdg = \frac{\sum_{i=1}^{n}(Counts_i \cdot DC_{i-1})}{n}$$

Equation 2.9 Readings averaged and depletion corrected

The system sensitivity, *S*, described in Section 2.4.2, is determined by the same method for OSLD as for TLD. The average corrected reading is multiplied by the system sensitivity factor, and several batch correction factors (K_F, K_L, and K_E). These batch correction factors are similar in meaning to the correction factors used for TLD dosimetry, but the calculation methods differ.

2.5.1 Element Correction Factor

The sensitivity of an individual OSLD varies compared to the population of OSLD within the batch of dosimeters, and is corrected for in the dose calculation by the element correction factor (*ECF*). Each OSLD within a batch are irradiated to a known dose and then read. The response of a single dosimeter at the particular dose level is then divided by the average response of the entire population of dosimeters within the batch, resulting in the ECF for that particular OSLD. The ECF is determined at a dose of 25 cGy, and verified at other dose levels. The sensitivity of OSLD have been shown to change with accumulated dose, as discussed in Section 1.3.2, but the RPC has verified that for accumulated doses of less than 10 Gy, the average ECF over cycles of irradiation and annealing compared to the first ECF determined for the dosimeter are within 0.6% [25]. No dosimeter used in this study received an accumulated dose greater than 10 Gy.

2.5.2 OSLD Batch Correction Factors

The fading of the OSL signal after irradiation is corrected using Equation 2.10 for both batches 06K10 and 16K12:

$$K_F = \frac{1}{1.005 \cdot d^{-0.0072}}$$

Equation 2.10 OSLD fading correction factor

where *d* is the number of days since irradiation. The RPC OSL dosimetry protocol requires that the dosimeters be read no sooner than five days post-irradiation.

The correction for the linearity of the response is calculated using Equation 2.11, which is the same as the equation for TLD, but with different constants and the raw dose is calculated in Equation 2.12 using the average reading that has been corrected by the ECF. The RPC protocol for calculating the linearity correction is to perform six iterations of the calculation to arrive at a final linearity correction value.

$$K_L = a \cdot raw\ dose^2 + b \cdot raw\ dose + c$$

Equation 2.11 OSLD linearity correction

$$raw\ dose = \ Avg\ Corr\ Rdg\ \cdot S\ \cdot K_F$$

Equation 2.12 OSLD raw dose calculation

As discussed in Section 1.3.2, the linearity of the response of the dosimeter changes with dose. The linearity correction varies between batches. For the 06K10 batch, the OSLD were commissioned and a linearity correction factor was found for doses up to 3.5 Gy. The response of the dosimeter is linear in this dose region, and the constants are a = 0, b = -0.00011579, and c = 1.0116. The commissioning of the OSLD batch 16K12 measured linearity beyond what was studied for the previous batch. For doses up to 15 Gy, the response of the 16K12 dosimeters is supra linear and the constants are a = 8.34622e-8, b = -2.67355e-4, and c = 1.0259.

The energy correction factors have been studied for both batches of OSLD under reference point geometry, for use in calculating doses from OSLD irradiated in the RPC mini-phantoms. The energy correction factors for the nanoDot dosimeters have not yet been studied under full phantom conditions. As described in Section 2.3.3, irradiations were performed to determine energy correction factors for the OSLD in full phantom.

2.5.3 microStar™ Reader

The microStar™ Reader (Landauer, Inc., Glenwood, IL), shown in Figure 2.13, is currently used by the RPC to read OSLD, and was used for this study. The reader is connected to a computer, which is used to control the reader and record data from the dosimeters into a database. The reader uses an array of 38 LED to stimulate the dosimeter, and operates in CW-OSL mode as described in Section 1.3.3. The LED are set to expose the detector for 7 seconds, according to RPC protocol. A 'strong beam' uses all 38 LED for reading low dose dosimeters, and a 'weak beam' uses 6 LED for reading dosimeters with high doses; a single LED illuminates the dosimeter before readout to determine the dose range[6]. The signal from dosimeters that have been irradiated to greater than 200 cGy saturate the optical detector circuits when illuminated with the strong beam, but using the weak beam, the dosimeters can receive a dose up to about 15 Gy before the optical detector is saturated[15].

The light produced by the LED bank in the reader is filtered by an OG-515 (Melles Griot, Rochester, NY) band-pass filter. Prior to reaching the PMT, the stimulation and luminescence photons are differentiated using a combination of Schott BG-12 (Schott, Mainz, Germany) and Hoya

B-370 (Hoya, San Jose, CA) colored glass filters. The LED and OG-515 filter combination has a peak transmission near 530 nm, and the combination of the PMT filters have a transmission peak at 385 nm[26].

Figure 2.13 microStar reader, adapter, and control computer

Before reading the OSLD, the reader is turned on and allowed to warm up at least 30 minutes prior to the session. Several quality control checks are performed on the reader, measuring the electrical noise of the system, the counts measured from just the LED, and the counts measured from a calibration source in the detector. The system sensitivity is determined and monitored according to the procedure described in Section 2.4.2. To begin reading the OSLD, the barcode of the dosimeter is scanned and it is inserted into the adapter shown in Figure 2.13. The adapter holds the nanoDot in place within the drawer of the reader, and when the drawer is shut, the adapter opens the dosimeter to expose the active volume to the light source. The counts measured by the PMT are recorded, and the OSLD can be removed from the reader.

2.5.4 Signal Depletion

The finite decrease in charge stored by the dosimeter with each reading was referred to in Section 1.3.2, and RPC OSL dosimetry includes a correction to account for this signal depletion. The depletion correction for the m^{th} reading (DC_m) is calculated using Equation 2.13:

$$DC_m = \frac{1}{a \cdot m^2 + b \cdot m + c}$$

Equation 2.13 OSLD depletion correction

where a = -5.148e-6, b = -1.277e-3, c = 1, and for a dosimeter read three times, m = {0…2}.

2.5.5 Optical Bleaching

The optical bleaching (annealing) of the OSLD at RPC is performed using the cabinet shown below in Figure 2.14. Within the cabinet, there are four 54-watt fluorescent bulbs; two bulbs are fixed at the top of the cabinet and two are positioned at the bottom. To remove any UV photons from the light, a filter is placed around each bulb. Positioned centrally between the top and bottom light sources lies a clear acrylic shelf on which the OSLD are placed. The dosimeters are opened, and the active volume is exposed to the light for 24 hours before they are closed and removed from the box.

Figure 2.14 Cabinet for optical bleaching of OSLD at the RPC

2.6 RPC Film Dosimetry

Radiochromic film is favorable for measuring relative dose distributions because of their high spatial resolution, insensitivity to visible light, they are nearly tissue equivalent, and they color directly, eliminating the need for processing. The image formation occurs as a dye-forming or

polymerization process, and the image is stable over a range of temperatures. The humidity during irradiation also has little impact on the film[27].

Gafchromic EBT2 film (Ashland, Wayne, NJ) was used in this study, from lot number A0521102 with an expiration date of May 2013. The RPC uses radiochromic film as a part of the remote audit program, and has already investigated the dose response of this lot of film and performed a film calibration for the dose range of 0 to 30 Gy. The dose-response curve generated by the RPC for this batch of film fits the third-order polynomial shown below in Equation 2.14, establishing a relationship between dose and optical density (*OD*):

$$Dose = 29.898 \cdot OD^3 - 13.588 \cdot OD^2 + 6.7634 \cdot OD$$

Equation 2.14 Calibration curve for Gafchromic EBT2 film, lot # A05261102

For each IMRT irradiation in this study, the pieces of film were cut from the same sheet using a template, and all sheets of film were from the same film lot. One piece was cut for the coronal film, and the sagittal film was cut in two parts. Each piece of film was marked for orientation. The care and evaluation of the film was performed according to the recommendations of AAPM TG-55, which include storing the film in a dark and dry place at room temperature, visually inspecting the film before irradiation, careful handling of the film, and reading the film at least 48 hours after irradiation to minimize the effects of self-development[27].

The active layer of the EBT2 film is situated between two polyester layers, making it possible to be submerged in water for short time periods, and includes a yellow marker dye to minimize differences in film responses due to small variations in thickness of this layer. This marker dye also has the benefit of making the EBT2 film less sensitivity to ambient light. When the film is irradiated, the elements in the active layer react and form a blue polymer that appears green due to the presence of the yellow marker dye. The irradiated film has an absorption peak at 636 nm, and 585 nm. According to the manufacturer, the film is designed for a wide dose range (1 cGy to 40 Gy), and has an effective atomic number of 6.84, demonstrating a difference in response of about 10% in the keV to 6 MV photon energy range. A recent study investigating the energy dependence and dose response of the EBT2 films found that the energy dependence of the film was lower than that suggested by the manufacturer, showing that the response of the film varied by approximately 4.5% over an energy range of 75 kVp to 18 MeV photons[28]. This study also reported that the self-development of the film was the fastest during the first 48 hours after the film was irradiated.

2.6.1 Film Scanning

To evaluate the dose distribution measured, the films were scanned using a CCD100 Microdensitometer (Photoelectron Corporation, Lexington, MA) as shown below in Figure 2.15. The scanner uses an LED light bed, with a wavelength of 665 nm, and a CCD camera placed above the film to measure and record the transmission of light. The height of the CCD was set so that the camera focused on a 200 x 200 mm^2 area where the films would be placed, and the remaining area of the light was covered with a black mask. This system is contained within a cabinet to prevent measurement of room light. A blank piece of film from the same lot was scanned and used to measure the 'flat field', and then a grid of known size and spacing was scanned to assign a spatial calibration. Following these calibrations, the films from the IMRT irradiations were scanned in a consistent orientation. The coronal film was scanned, and then the two pieces of the sagittal film were placed together and scanned. The images were saved as 16-bit .FIT files.

Figure 2.15 Setup of microdensitometer used for film scanning

2.6.2 Registration

The measured dose distribution from the film is compared to the reported dose distribution from the treatment planning system (TPS), and to do this, the film and the plan must be registered to the same phantom coordinate system. Using a MATLAB (The MathWorks, Inc., Natick, MA) program known as the Computational Environment for Radiotherapy Research (CERR) (J.O. Deasy and Washington University, St. Louis, MO), the treatment plan can be registered to the phantom coordinate system. From the TPS, the plan, CT image set, composite dose information, and structures are all exported in DICOM-RT format into CERR. On the CT images, a set of registration points are identified, which registers the plan to the phantom. Using another MATLAB program, RPCFILM, the films can be registered to the phantom coordinate system. The .FIT files created after scanning the film, as discussed in Section 2.6.1, are opened in RPCFILM. The phantom type and number are identified, and the pinpricks are identified on the image. The location of the pinpricks are unique to each phantom, and this registers the film to the phantom coordinate system. After both the film and the treatment plan have been registered to the phantom coordinate system, RPCFILM evaluates the goodness of fit and calculates RMS error values for the film registration and plan registration, called 'RMS Error' and 'RMS 3D', respectively. To minimize error, the RPC prefers an 'RMS Error' of 0.3 mm or less for one piece of film, such as the coronal film in this study, or 0.5 mm or less for two pieces of film, such as the sagittal films in this study. The limit for 'RMS 3D' is set at 1 mm.

The dose-response curve for the film batch is then used to calculate the measured film dose from the OD values. The film doses are then normalized to the TLD dose measured in the PTV. For this study, film analysis was performed only for the three IMRT irradiations as well as for the two institution trials (one IMRT, one CyberKnife). For each irradiation, the films were normalized to the PTV TLD doses, as well as to the corrected PTV OSLD doses and then compared, as discussed in later sections.

2.7 Dosimetric Evaluation

To evaluate the ability of the OSLD to measure on average the same dose as the TLD, the TLD and OSLD dose measurements from the pelvic phantom irradiations were compared in several ways. The absolute doses from the TLD and OSLD, the dose profiles normalized by the TLD and OSLD doses, and the gamma analysis of the film normalized to both TLD and OSLD were compared.

2.7.1 Absolute Dose

For the pelvic phantom irradiations, the dose measured in the target volume for the TLD and the OSLD were compared. The locations of the TLD and OSLD within the target can be seen below in Figure 2.16. The doses measured by the two TLD within the target were calculated using the method described in Section 2.4, and then averaged. The dose measured by the two PTV OSLD were calculated using the method described in Section 2.5, averaged, and then multiplied by a correction factor obtained from the spherical phantom for the appropriate irradiation. The OSLD dose multiplied by the correction factor is referred to as the corrected OSLD dose. The TLD dose was compared to the OSLD dose, as stated in the hypothesis. A ratio of TLD dose to corrected OSLD dose for each pelvic phantom irradiation was calculated, and the average TLD to OSLD dose ratio was calculated. The TLD dose within the femoral heads was not compared to any OSLD doses, as there were no OSLD placed within the structure.

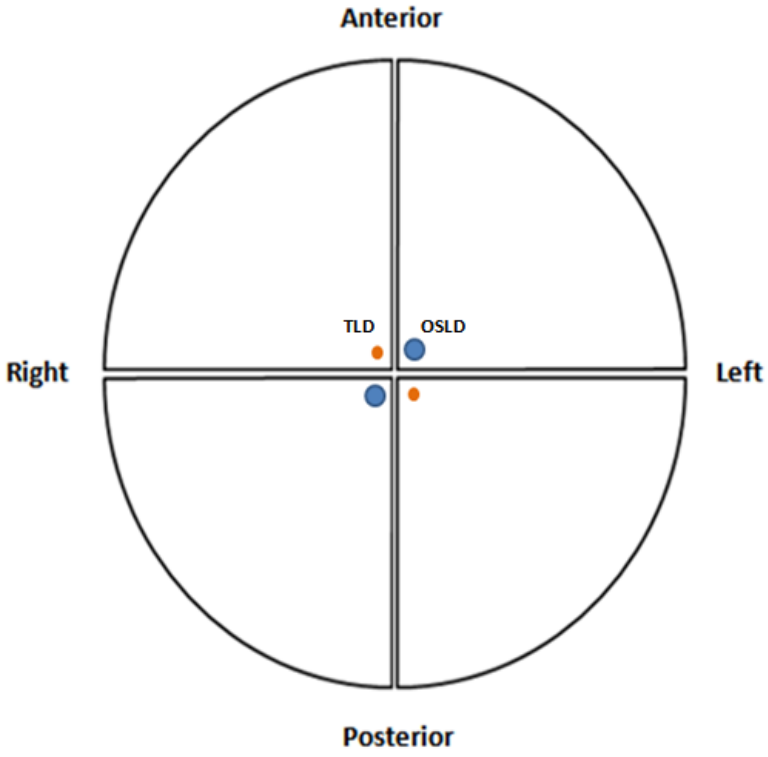

Figure 2.16 Diagram of inferior view of the dosimetry insert showing positions of TLD and OSLD active volumes within the target

2.7.2 Dose Profiles

Using the RPCFILM program, dose profiles through the PTV were obtained for both the coronal and sagittal films. For the coronal films, dose profiles were recorded in the lateral and superior-inferior directions. The lateral profile was taken through the PTV, and the superior-inferior profile was taken through the PTV and the bladder. On the sagittal films, dose profiles were recorded in the anterior-posterior (AP) and superior-inferior directions. The AP profile was taken through the PTV as well as through the rectum. The superior-inferior profile included the dose through the PTV and through the bladder. The superior-inferior dose profile for the sagittal films was offset from the center in the AP direction by 2 mm to avoid the gap where the two pieces of the sagittal film were positioned together for scanning. The film was sampled every 0.3 mm to create the dose profiles, and a 3 mm moving average was used to smooth the data obtained for the profiles.

The dose profiles were created after the film was normalized to the TLD target doses and the corrected OSLD target doses. Each profile was plotted displaying the dose calculated by the TPS, the normalized film dose, and either the TLD dose or the corrected OSLD dose. The dose profiles resulting from both the TLD and OSLD normalized doses were compared.

2.7.3 Gamma Analysis

Gamma analysis is a quantitative method described by Low *et al.*[29] for comparing dose distributions measured by film to those generated by the treatment plan, using the measured distribution as the reference information. This technique evaluates the dose difference between measured and calculated, and the distance to agreement (DTA), combining the comparisons into a single numerical index called the gamma (γ) index. A set of criteria for dose difference and DTA are established for acceptance, each having equal significance in the calculation of the index. The acceptance criteria for dose difference and DTA form an ellipsoid surface, with the measurement point at the origin. For each pixel, the dose difference and DTA are calculated and a vector is formed from the origin to the calculated point. If the magnitude of the normalized vector is less than or equal to one, the calculated point lies within the ellipsoid, passing the criteria with $\gamma \leq 1$.

For this study, the Matlab program RPCFILM was used to perform the gamma analysis for each plane of film within the phantom. The criteria established for the RPC pelvic phantom is 7% dose difference and 4 mm DTA (7%/4 mm) for both the sagittal and coronal films, with at least an 85% pixel pass rate. RPCFILM includes a masking tool which allows for the designation of areas on the film to not be included in the analysis, such as pin pricks, the junction of the two sagittal films, or

any other film imperfections or artifacts. An example of area masking on a sagittal film can be seen below in Figure 2.17. RPC protocol for the pelvic phantom analysis is to use a 10 x 10 cm^2 area of the film for evaluation.

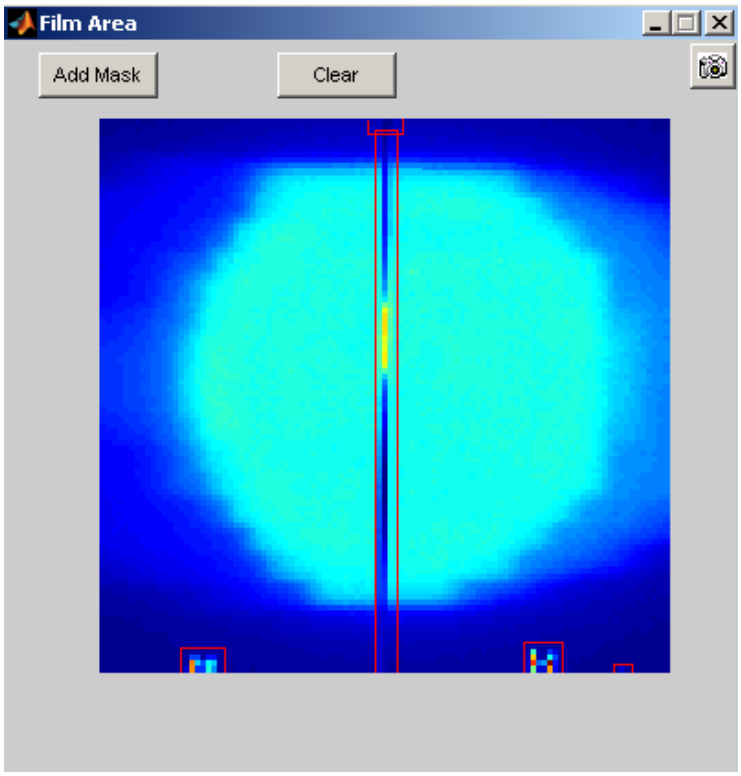

Figure 2.17 Masks applied to a sagittal film before gamma analysis

As discussed in Section 2.6.2, the films are normalized to the TLD target dose before analysis is performed. For this study, the films were also normalized to the corrected OSLD target dose and an additional gamma analysis was completed. The gamma results from the TLD normalization and OSLD normalization were compared.

Chapter 3 Results and Discussion

3.1 Treatment Planning

Four treatment plans of increasing angular beam delivery were developed as discussed in Section 2.2, each meeting the dose prescription and normal tissue constraints outlined in the RPC prostate IMRT credentialing protocol. For the three treatment plans developed in Pinnacle, the PTV, prostate, bladder, rectum, and femoral heads are represented by the purple, blue, yellow, green, and pink contours, respectively. The CyberKnife plan developed in MultiPlan displays the PTV, prostate, bladder, rectum contours as orange, coral, light blue, and green. The femoral heads are displayed as the pink and dark blue contours, representing the left and right femoral heads. The four treatment plans and their dose-volume histograms (DVH) are displayed below for the same CT slice, at the level of the simulation isocenter. As discussed in Section 2.3.2, the three coplanar treatment plans delivered a target dose of 3 Gy, while the CyberKnife plan delivered a target dose of 6 Gy.

3.1.1 Four Field Box

The isodose lines and the DVH generated by the 4-field treatment plan in the pelvic phantom can be seen below in Figure 3.1. The prescription dose of 3 Gy covers 99% of the PTV and 100% of the prostate volume. The normal tissue constraints are met, but the 4-field treatment does deliver a higher dose to the critical structures than the subsequent plans.

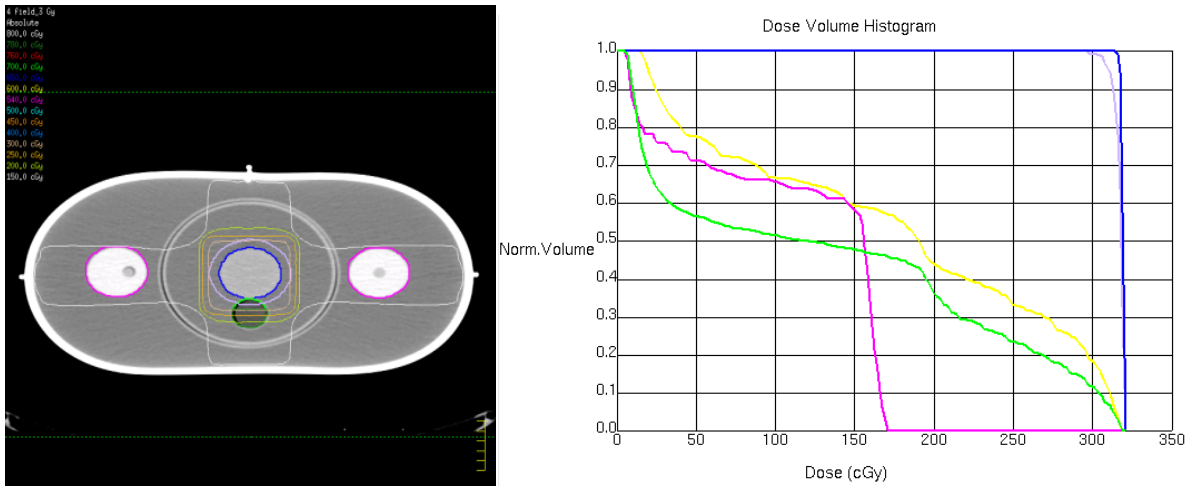

Figure 3.1 Four field isodose coverage (left) and DVH (right) for the prostate phantom. The PTV, prostate, bladder, rectum, and femoral heads are displayed as purple, blue, yellow, green, and pink, respectively.

3.1.2 IMRT

The IMRT treatment plan for the pelvic phantom isodose plot and DVH can be seen in Figure 3.2. The target prescription dose of 3 Gy covers 99% of the PTV and achieves complete coverage of the prostate volume. As seen in the DVH, the dose to the femoral heads, bladder, and rectum are all lower than for the 4-field box treatment.

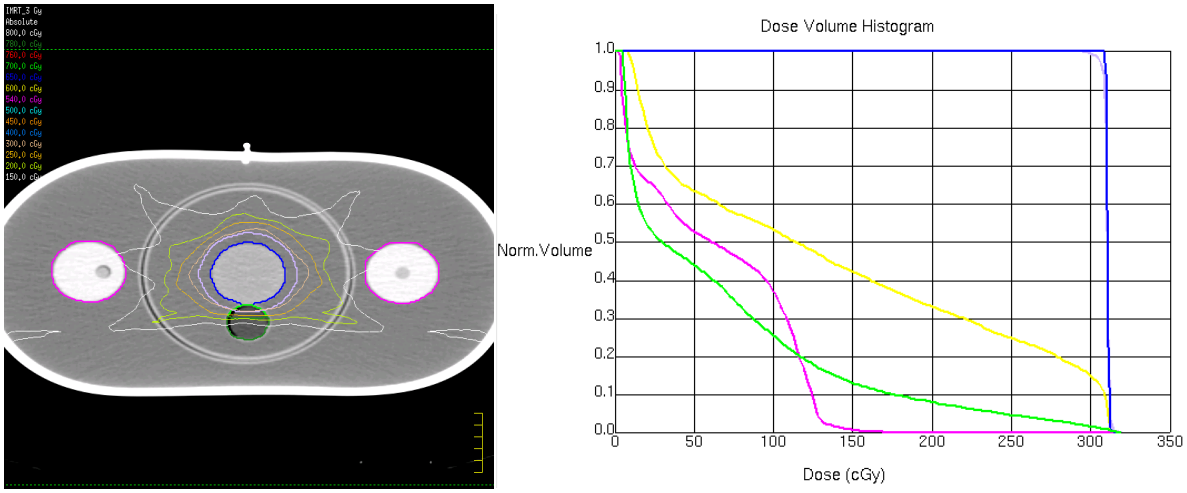

Figure 3.2 IMRT isodose coverage (left) and DVH (right) for prostate phantom. The PTV, prostate, bladder, rectum, and femoral heads are displayed as purple, blue, yellow, green, and pink, respectively.

3.1.3 VMAT

The isodose coverage and DVH generated for the pelvic phantom VMAT treatment plan can be seen below in Figure 3.3. The prescription dose of 3 Gy covers 99% of the PTV and 100% of the prostate, meeting the dose prescription outlined previously. Similar to the IMRT treatment, the doses received by the normal structures are lower compared to the 4-field treatment.

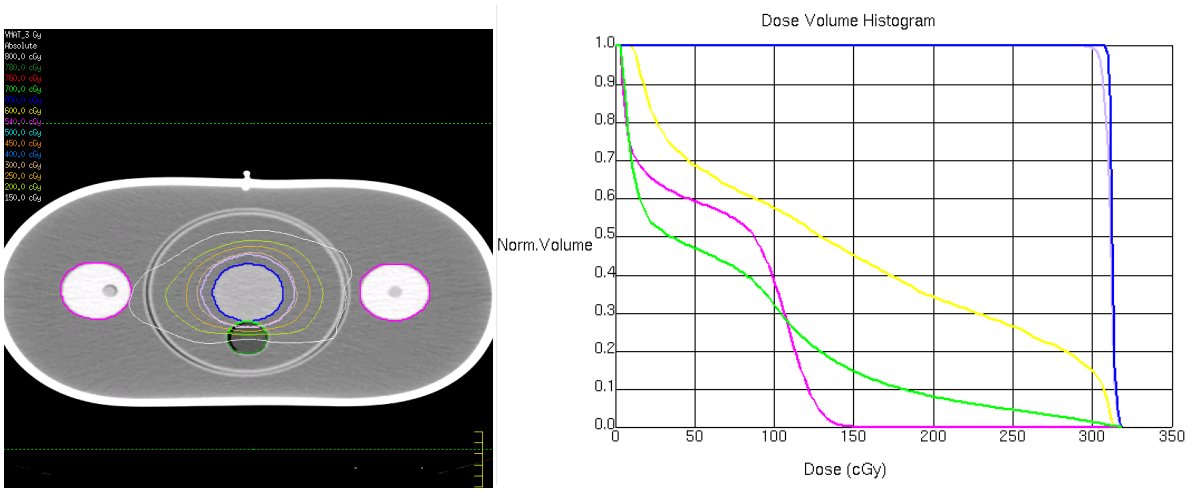

Figure 3.3 VMAT isodose coverage (left) and DVH (right) for prostate phantom. The PTV, prostate, bladder, rectum, and femoral heads are displayed as purple, blue, yellow, green, and pink, respectively.

3.1.4 CyberKnife

The isodose lines and DVH generated by the CyberKnife plan developed in MultiPlan for the pelvic phantom can be seen below in Figure 3.4. The prescription dose of 6 Gy covers 99.8% of the PTV and 100% of the prostate volume. The bladder and rectal dose were higher for the CyberKnife treatment than for either the IMRT or VMAT treatment plans.

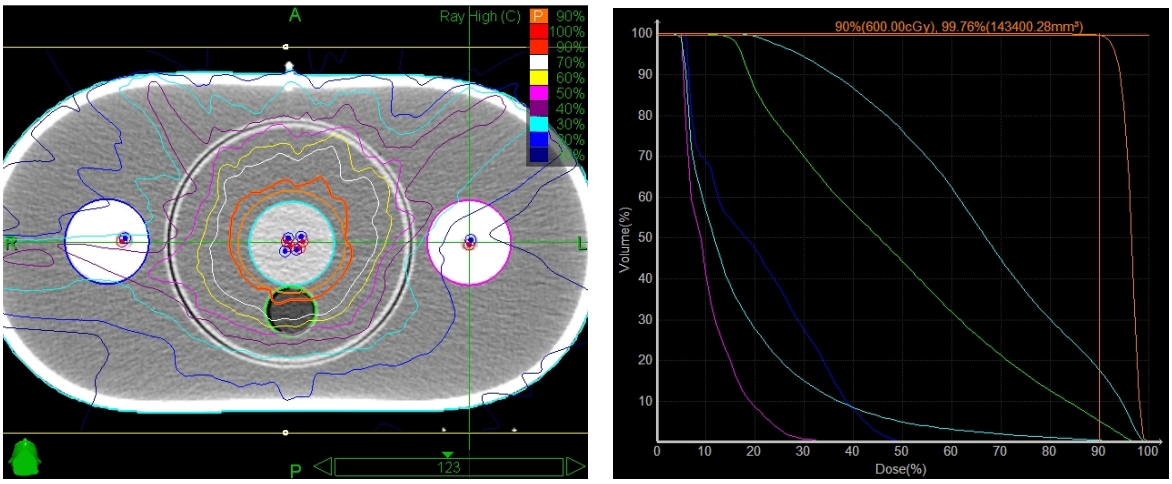

Figure 3.4 CyberKnife isodose coverage (left) and DVH (right) for prostate phantom. The PTV, prostate, bladder, and rectum are displayed as orange, coral, light blue, and green. The left and right femoral heads are represented by the pink and blue contours, respectively.

3.2 Phantom Irradiations

3.2.1 Spherical Phantom Irradiations

The irradiations of the spherical phantom were carried out according to the setup described in Section 2.3.1. The MU needed to deliver 100 cGy to a depth of 5 cm on CAX, for a field size of 5 x 5 cm^2 for photon beams of energy 6 MV and 18 MV were calculated using Equation 2.1, and are shown below in Equations 3.1 and 3.2, respectively. For both beam energies, there is no off-axis factor (*OAF*) and there were no trays or wedges attenuating the beam. The depth factor used for these calculations was Tissue Maximum Ratio (TMR), since the phantom irradiation was performed using the SAD technique. The MU necessary to deliver the desired dose at 6 MV was calculated to be 114 MU, and 101 MU at 18 MV.

$$MU = \frac{100\ cGy}{1.03\ \frac{cGy}{MU} \cdot\ 0.905\ \cdot 0.962\ \cdot 0.983} = 114\ MU$$

Equation 3.1 MU calculation for 6 MV spherical phantom irradiation

$$MU = \frac{100\ cGy}{1.067\ \frac{cGy}{MU} \cdot\ 1.001\ \cdot 0.943\ \cdot 0.982} = 101\ MU$$

Equation 3.2 MU calculation for 18 MV spherical phantom irradiation

The dose delivered to each OSLD was calculated using Equation 2.7. The normalized OSLD responses for the coplanar 6 MV spherical phantom irradiations can be seen below in Figure 3.5. The error bars for each data point represent the standard error (SE). The null hypothesis of the one-way ANOVA test was rejected (p-value = 0.000), showing that the mean of at least one angle response was different from the other mean responses. The Fisher's LSD test determined that the response of the dosimeter at the face-on angle was statistically significantly different from all other angles at the α=0.05 level

An additional ANOVA was performed including only the edge-on angular responses, and the resulting p-value of 0.124 shows that the null hypothesis cannot be rejected. The responses at these angles cannot be from different populations, therefore the responses can be grouped together. Knowing this, the normalized responses for all edge-on angles were averaged, and the average was calculated to be 0.961 and is indicated on the graph as the red horizontal line.

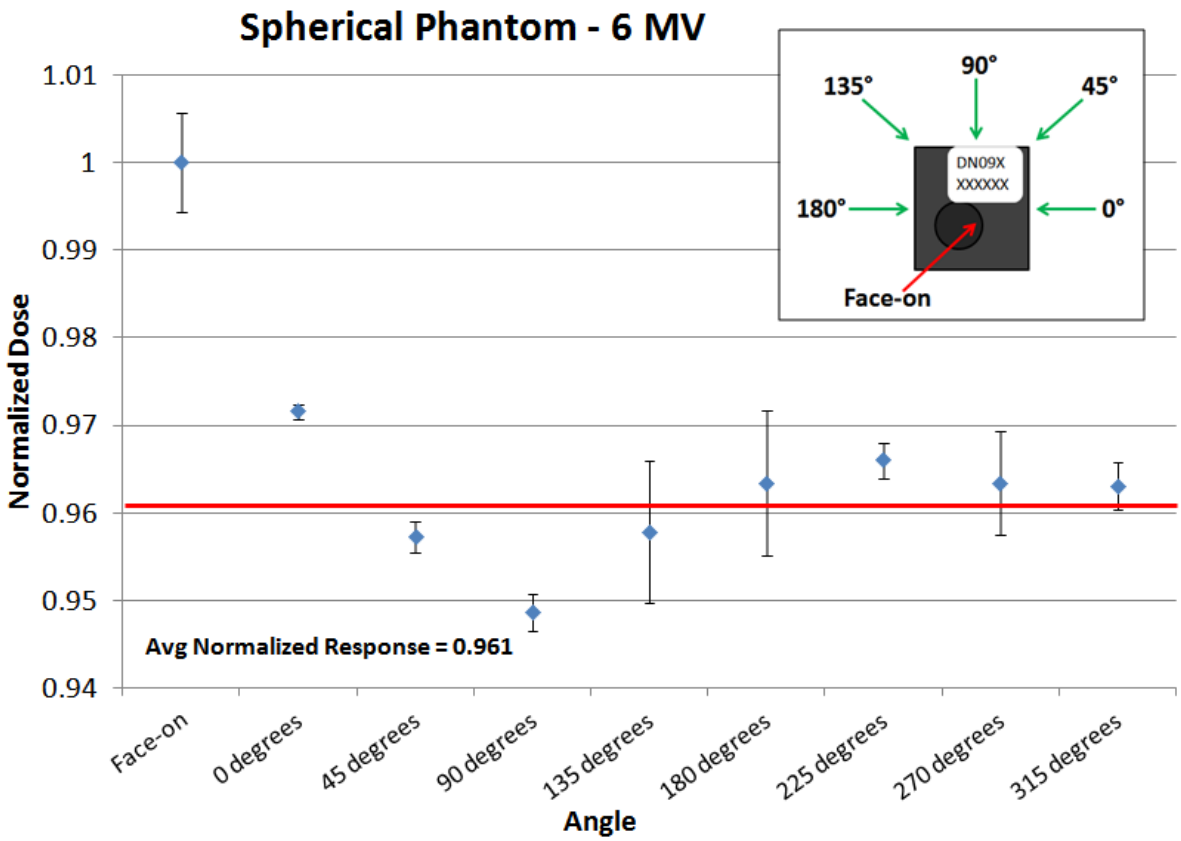

Figure 3.5 OSLD response for coplanar 6 MV spherical phantom irradiations

For the coplanar 18 MV spherical phantom irradiations, the normalized OSLD responses can be seen below in Figure 3.6. The error bars represent the standard error for each angular response. The noticeably larger error for the average dose at 180° is due to one of the three OSLD irradiated at that angle being either a bad OSL, or there was an error in the irradiation of the dosimeter, so that data was not included in the calculation of the average dose, nor the standard error. The responses of the dosimeters at the varying angles were found to be statistically significantly different (p-value = 0.006) after running one-way ANOVA. The Fisher's LSD test showed that the OSLD response for the face-on angle was statistically significantly different from the edge-on angular responses. A second ANOVA test, comparing only the edge-on angular responses showed that there is no difference in response between the angles (p-value = 0.425). The average edge-on normalized OSLD response, indicated by the red horizontal line on the graph, was calculated to be 0.981.

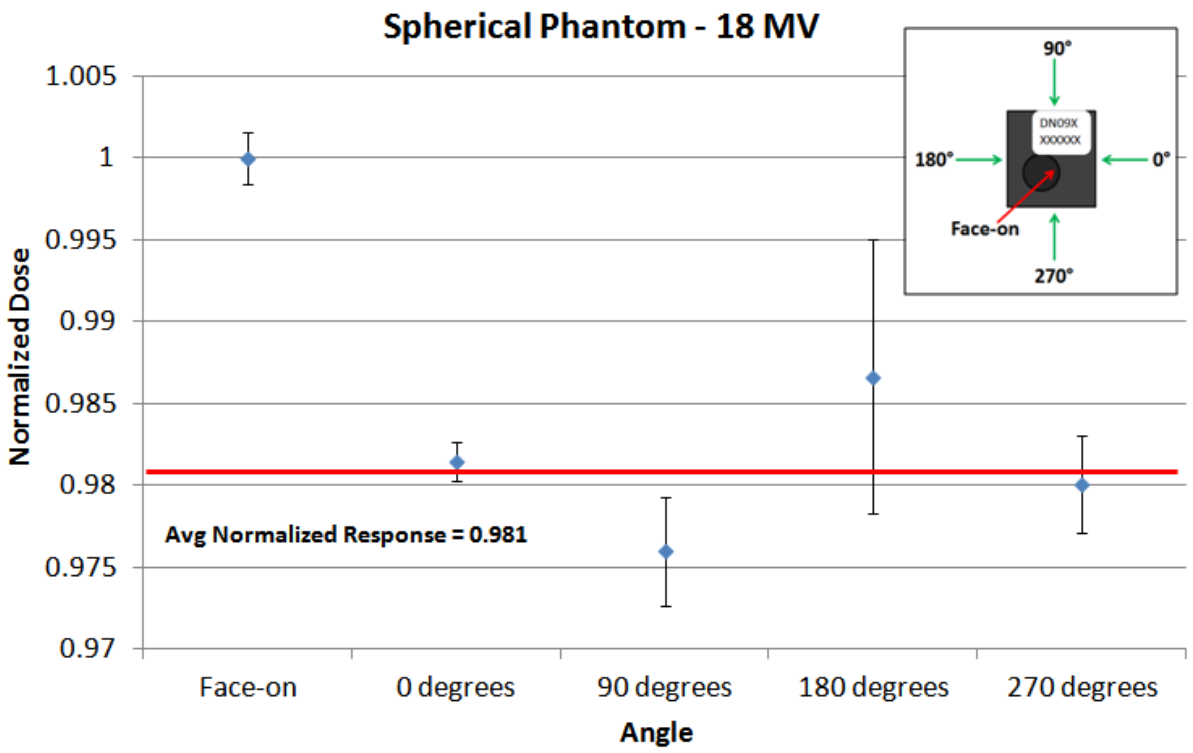

Figure 3.6 OSLD response for coplanar 18 MV spherical phantom irradiations

The normalized OSLD responses from the non-coplanar 6 MV spherical phantom irradiations, specific to CyberKnife, can be seen in Figure 3.7. The error bars for each data point represent the standard error. A statistically significant difference was found between the different angles irradiated (p-value = 0.000), and the Fisher's LSD test determined that the response of the dosimeter at the face-on angle was statistically significantly different from the responses for all remaining angles. An additional ANOVA was performed, excluding the face-on response, and the resulting p-value of 0.006 shows that the null hypothesis can be rejected and the responses of these angles are from different populations and the means of the angular responses are not equal. The average edge-on dosimeter response was still calculated, and found to be 0.963 as shown by the red horizontal line on the graph.

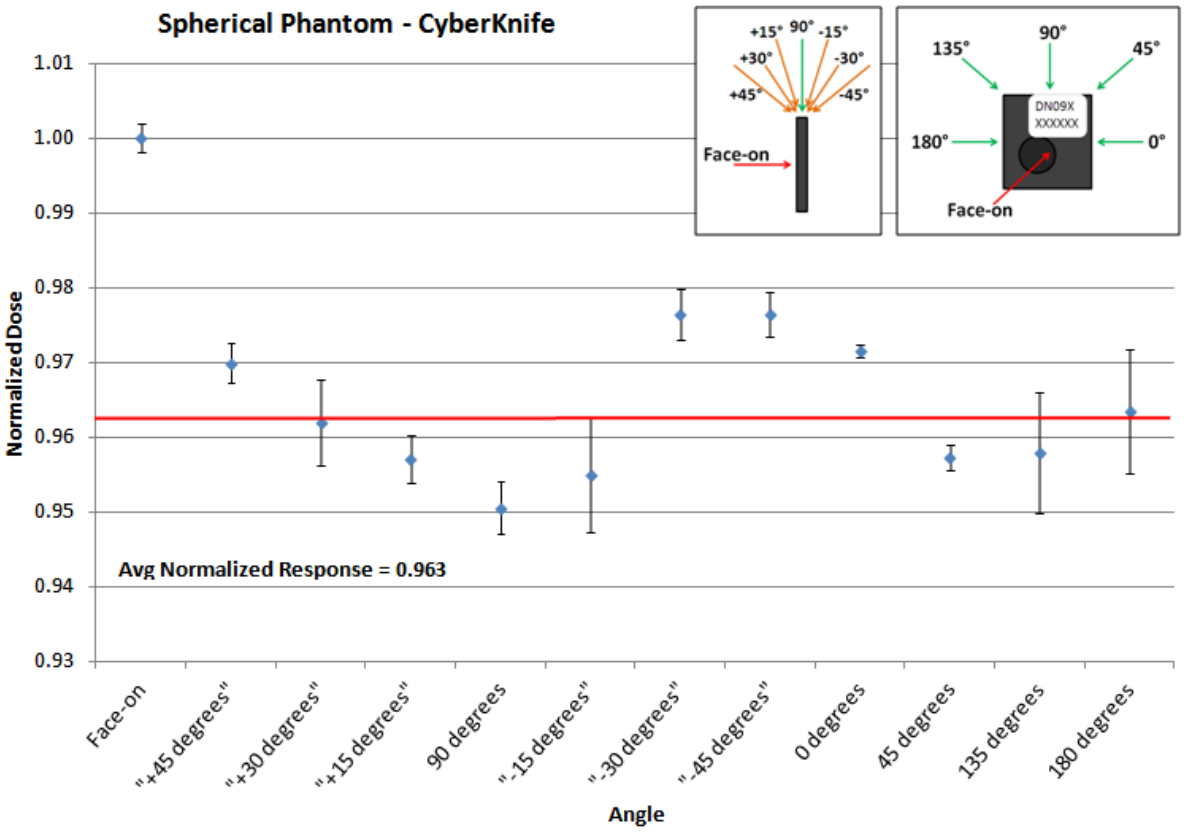

Figure 3.7 OSLD response for non-coplanar 6 MV spherical phantom irradiations

For each spherical phantom irradiation, the average normalized response of the dosimeters in the edge-on orientation was determined. The averaged doses measured by the dosimeters in the edge-on orientation relative to the doses measured when the beam was incident normally on the face of the dosimeter for the coplanar spherical phantom irradiations were 0.961 and 0.981, for 6 MV and 18 MV photon beams, respectively. These results demonstrate an under-response of the OSLD of approximately 4% for 6 MV, and 2% for 18 MV. The coplanar spherical phantom irradiation results are in agreement with the data published by Kerns *et al.*[3], which demonstrated a decrease in the OSLD response of 4% for 6 MV photon beams parallel to the surface of the dosimeter. The angular response at 6 MV of the nanoDot dosimeter normalized to the dosimeter response at 0° reported by Kerns can be seen below in Figure 3.8, demonstrating the approximately 4% decrease in response of the dosimeter for the edge-on irradiations (90° and 270°). It is important to note that the orientation of the nanoDot within the pelvic phantom for the Kerns study is not the same as the orientation used in this study, and as such, only the responses at 0°, 90°, and 270°are applicable for comparison.

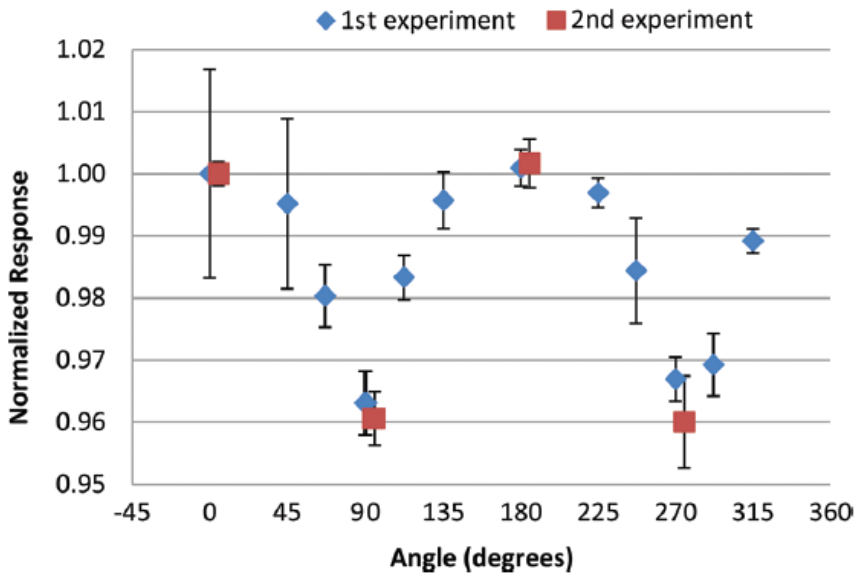

Figure 3.8 Angular response of OSLD at 6 MV normalized to response at 0°, error bars represent the coefficient of variation (Kerns *et al.*), copied with permission from AAPM.

The decrease in response of 2% for the 18 MV coplanar spherical phantom irradiations observed in this study is slightly higher than the decrease in response of 3% for the edge-on irradiations reported by Kerns, which can be seen below in Figure 3.9. The increased response observed in this study for 18 MV coplanar photon beams compared to the Kerns study, going from an under-response of 3% to 2%, could be attributed to differences in the phantoms used. The decrease in response of 2% for the OSLD was measured in the small, spherical phantom from this study, whereas the under-response of 3% reported by Kerns was measured in the RPC's pelvic phantom. The scatter conditions provided by the two phantoms are different, and as discussed in Section 1.1, the scatter component is important to the dose deposited in the OSLD. While the small differences in responses observed at 18 MV (2 % vs. 3%) may be due to the phantoms, the responses may be the same within experimental uncertainties. However, the trend of an increase in response from 6 MV to 18 MV photon beams that was shown by Kerns is supported by the results of this study.

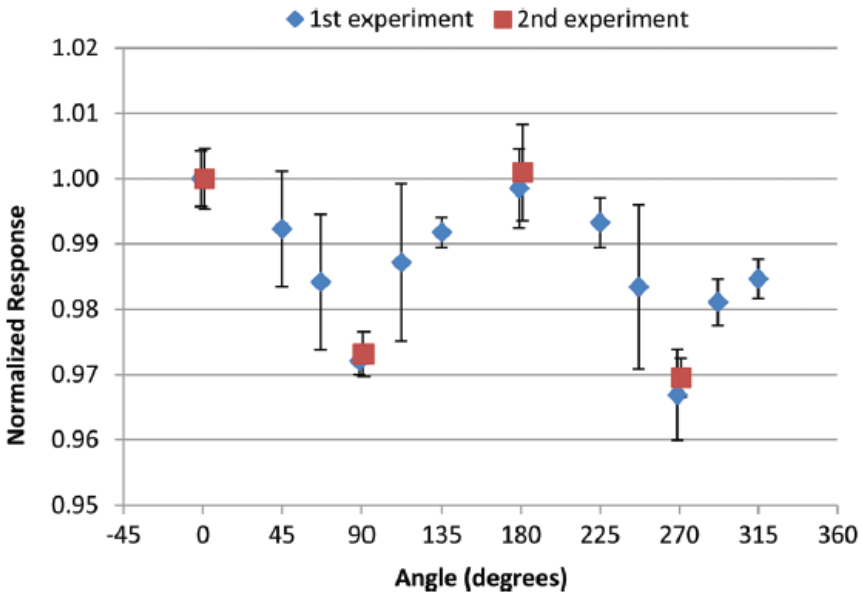

Figure 3.9 Angular response of OSLD at 18 MV normalized to the response at 0°, error bars represent the coefficient of variation (Kerns *et al*), copied with permission from AAPM.

The averaged dose measured by the dosimeters normalized to the dose measured in the face-on orientation for the non-coplanar 6 MV spherical phantom irradiations was 0.963, demonstrating a 4% under-response of the dosimeter. However, the ANOVA results indicate that the normalized responses at all the investigated non-face-on angles are not from the same population, so averaging the responses may not be an appropriate method of determining the angular response of the OSLD.

The inverse of the average normalized responses was then taken to determine the angular correction factors to be used for adjusting the OSLD measured dose for the pelvic phantom irradiations. The angular correction factors calculated can be seen below in Table 3.1. These factors were applied to the OSLD measured dose from the pelvic phantom irradiations, as shown in Section 3.3 for the absolute dose, dose profiles, and gamma analysis comparisons.

	Angular Correction	***Stdev***
Coplanar 6 MV	1.040	0.007
Coplanar 18 MV	1.019	0.004
Non-coplanar 6 MV	1.038	0.009

Table 3.1 Angular correction factors and standard deviations from spherical phantom irradiations

3.2.2 Pelvic Phantom Irradiations

Irradiations of the RPC pelvic phantom were carried out according to the setup discussed in Section 2.3.2. Each treatment plan was delivered three times, and the doses measured from both the TLD and the OSLD for each coplanar treatment plan (4-field, IMRT, VMAT) can be seen below in Figure 3.10. The error bars for each data point represent the standard error. The TLD dose was calculated using Equation 2.3, and the dose delivered to the OSLD was calculated using Equation 2.7. The doses measured by the two TLD in the PTV were averaged, as well as the doses from the two OSLD in the PTV, to represent a single dose delivered to the center of the PTV in the phantom. The OSLD measured dose, not corrected for angular dependence, is shown to be consistently lower than the doses measured by the TLD in the pelvic phantom for the coplanar irradiations. The under-response of the OSLD compared to the TLD is shown to be greater for the 6 MV IMRT and VMAT irradiations, than for the 18 MV 4-field irradiations, consistent with the spherical phantom results shown in Section 3.2.1. The average percent differences between the TLD measured dose and uncorrected OSLD measured dose for the 4-field, IMRT, and VMAT irradiations were calculated to be 1.9%, 3.0%, and 3.3%, respectively.

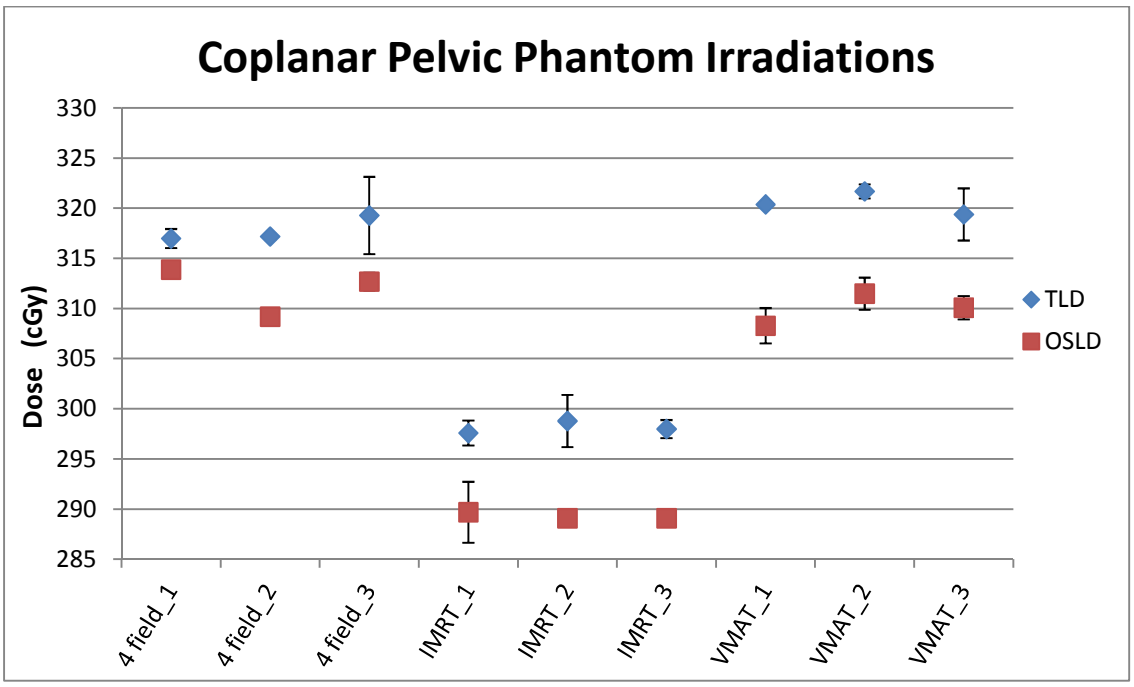

Figure 3.10 TLD and OSLD doses from 3 Gy coplanar pelvic phantom irradiations

The doses measured by the TLD and OSLD in the PTV of the pelvic phantom for the CyberKnife irradiations performed can be seen below in Figure 3.11. The data for the TLD doses and

OSLD doses are offset from each other in the x-direction for clear visualization of the data points and their associated errors. The error bars for each dose represent the standard error. Again, the TLD and OSLD doses were calculated using Equations 2.3 and 2.7, respectively. The doses measured by the two target TLD were averaged to represent a single dose delivered to the center of the prostate. The same averaging was done with the two target OSLD doses. In the pelvic phantom, the OSLD, not corrected for angular dependence, once again under-responded for the non-coplanar treatment as compared to the response of the TLD. The average percent difference between the TLD measured dose and uncorrected OSLD measured dose was calculated to be 1.1% for the three CyberKnife irradiations. However, the doses measured by the OSLD, not corrected for angular dependence, for the three CyberKnife irradiations were closer to the doses measured by the TLD than expected. Many of the beams in the CyberKnife deliveries were from angles superior and inferior to the edge-on angles, so the angular correction is not as great as for the gantry based, coplanar deliveries.

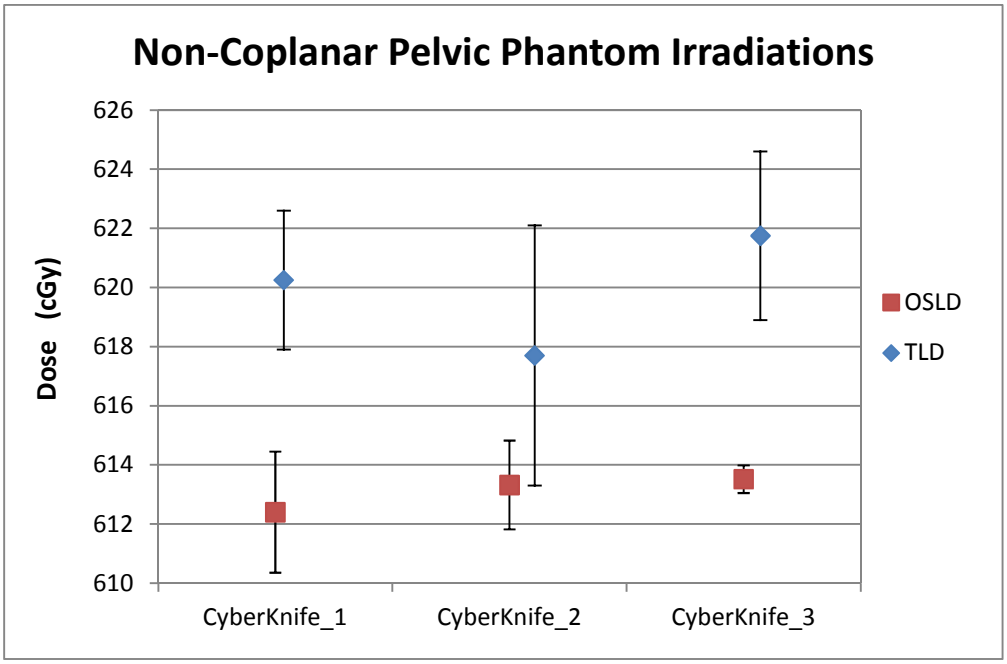

Figure 3.11 TLD and OSLD doses from the three 6 Gy non-coplanar pelvic phantom irradiations

As discussed in Section 2.3.2.1, the prostate phantom was sent to two different institutions to evaluate the response of the OSLD in the phantom. One institution delivered a standard prostate IMRT treatment, and the second institution delivered a CyberKnife treatment. The doses measured by the target TLD and OSLD in the pelvic phantom for both institution trials can be seen below in Figure 3.12. The error bars for each dose represent the standard error. The doses measured by the TLD were calculated using Equation 2.3, and the dose measured by the OSLD was calculated using

Equation 2.7. The doses from the two TLD were averaged, and the doses from the two OSLD were averaged to represent a single dose to the PTV. For each institution trial, the uncorrected OSLD dose was lower than the TLD dose. The percent differences between the TLD measured dose and uncorrected OSLD measured dose were 4.4% and 3.4% for the IMRT and CyberKnife institution trials, respectively. For the CyberKnife trial, the OSLD measured dose was much lower compared to the TLD measured dose and consistent with the response expected from the non-coplanar spherical phantom irradiations, but contrary to the CyberKnife results shown in Figure 3.11 (1.1% difference as compared to 3.4%). As mentioned previously, the majority of the beam angles for the CyberKnife irradiation were incident on the OSLD at angles superior and inferior to the edge-on angles, which would result in a lower angular correction than for the coplanar deliveries, but this was not observed for the CyberKnife trial.

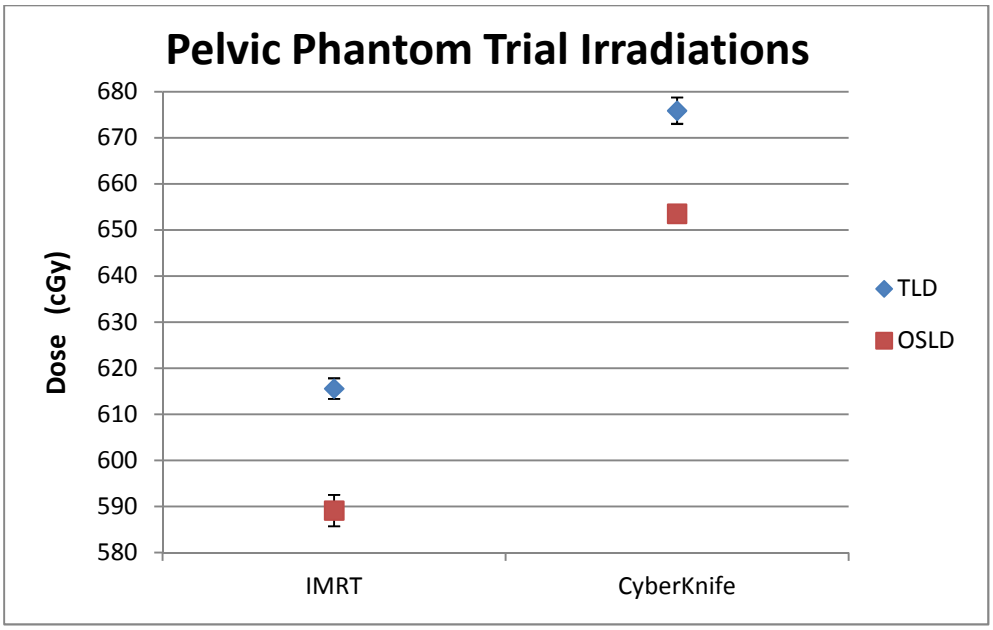

Figure 3.12 TLD and OSLD doses from 6 Gy institution trials

Comparison of the TLD and OSLD measured doses, as well as the corrected OSLD doses using the values presented in Table 3.1, is performed later in Section 3.3.1.

3.2.3 Energy Correction Irradiations

The irradiations necessary to determine the energy correction factors for OSLD in full phantom conditions were performed as described in Section 2.3.3. Ion chamber measurements in the polystyrene slab phantom were made at a depth of 10 cm, the depth where the OSLD would later be

placed, for the calculation of dose rate and dose delivered to the OSLD. Three ion chamber readings were made for the two beam energies, and the results can be seen below in Table 3.2.

Beam Energy	***Reading 1 (nC)***	***Reading 2 (nC)***	***Reading 3 (nC)***
6 MV	26.69	26.68	26.68
18 MV	31.85	31.84	31.84

Table 3.2 Ion chamber measurements in slab phantom at depth of 10 cm for 6 MV and 18 MV photon beams

These ion chamber readings were used to calculate the dose rate to water at a depth d_{max} using the TG-21 protocol, and making corrections for the dose rate to muscle at a depth of 10 cm. The dose rate to water at d_{max} was calculated to be 1.016 $\frac{cGy}{MU}$ for 6 MV, and 1.027 $\frac{cGy}{MU}$ for 18 MV. The TG-21 worksheets for the two beam energies can be found in the Appendix, in Section 5.1. The calculations for the dose rate to muscle at a depth of 10 cm for beam energies 6 and 18 MV can be seen below in Equations 3.3 and 3.4, respectively.

$$\dot{D}_{muscle}(at\ 10\ cm) = 1.016\ \frac{cGy}{MU} \cdot 0.99 \cdot \frac{66.3}{100} = 0.667\ \frac{cGy}{MU}$$

Equation 3.3 Dose rate to muscle at a depth of 10 cm for 6 MV photon beam

$$\dot{D}_{muscle}(at\ 10\ cm) = 1.027\ \frac{cGy}{MU} \cdot 0.99 \cdot \frac{80.7}{100} = 0.821\ \frac{cGy}{MU}$$

Equation 3.4 Dose rate to muscle at a depth of 10 cm for 18 MV photon beam

The MU estimated to deliver 100 cGy to a depth of 10 cm in the phantom was calculated for 6 MV and 18 MV, and can be seen in Equations 3.5 and 3.6, respectively. These MU settings were used to deliver approximately the desired dose to the OSLD at depth in the polystyrene phantom, as the %dd data is specified to water.

$$MU = \frac{100\ cGy}{66.3/100} = 151\ MU$$

Equation 3.5 MU calculation to deliver approximately 100 cGy to OSLD for 6 MV photon beam

$$MU = \frac{100\ cGy}{80.7/100} = 124\ MU$$

Equation 3.6 MU calculation to deliver approximately 100 cGy to OSLD for 18 MV photon beam

The ratio of the dosimeter response at the designated energy to the response for cobalt-60 was calculated as described in Section 2.3.3. Standard dosimeters were read for both the 06K10 and 16K12 OSLD batches, for which the expected dose delivered is 100 cGy. The average corrected reading (*Avg Corr Rdg*) for the 06K10 standards was calculated to be 434,931, which represents the raw PMT counts that have been depletion corrected and multiplied by the ECF for each dosimeter, as described in Section 2.5. The average corrected reading for the 16K12 standards was calculated to be 366,210. The fading correction factor (K_F) was calculated for all OSLD using Equation 2.10, and the fading correction factor for the standards from batch 06K10 can be seen below in Equation 3.7. The fading correction factor for batch16K12 standards, which were read 7 days after irradiation, was calculated using this same equation to be 1.009064.

$$K_F = \frac{1}{1.005 \cdot 6^{-0.0072}} = 1.007945$$

Equation 3.7 Fading correction factor for dosimeters read 6 days post-irradiation

The expected dose delivered to the standard dosimeters was calculated using the RPC spreadsheet, and was found to be 100.095 cGy.

For each dosimeter irradiated, the average corrected reading, fading correction factor, and linearity correction factor was calculated. The linearity correction factor was calculated using Equation 2.11 for both 06K10 and 16K12 dosimeters. The expected dose delivered to the standard dosimeters for 6 MV and 18 MV was calculated as shown below in Equations 3.8 and 3.9, respectively.

$$D_{6\ MV} = 151\ MU \cdot 0.667\ \frac{cGy}{MU} = 100.72\ cGy$$

Equation 3.8 Expected dose delivered to OSLD for 6 MV photon beam

$$D_{18\ MV} = 124\ MU \cdot 0.821\ \frac{cGy}{MU} = 101.8\ cGy$$

Equation 3.9 Expected dose delivered to OSLD for 18 MV photon beam

The ratio of dosimeter responses, calculated using Equation 2.2, was calculated for each irradiated OSLD. The ratios of the five 06K10 OSLD irradiated at 6 MV, and the ratios of the five 16K12 OSLD irradiated at 6 MV were averaged to produce an energy correction factor for the OSLD at 6 MV. The same averaging was done for the five 06K10 dosimeters and five 16K12 dosimeters irradiated at 18 MV. The inverse of the two ratios, one for each of the two beam energies, was taken to calculate the energy correction factors. The energy correction factors for OSLD in full phantom conditions, calculated for photon beam energies 6 MV and 18 MV can be seen below in Table 3.3. These energy correction factors were used in the calculation of OSLD dose as described in Section 2.5.

Beam Energy	***K_E***	***Stdev***
6 MV	1.02	0.010
18 MV	1.08	0.011

Table 3.3 Energy correction factors for OSLD in full phantom conditions

The calculated energy correction factors for OSLD in full phantom conditions are very close to the correction factors for TLD in full phantom, 1.03 and 1.07 for 6 MV and 18 MV photon beams, respectively. A decrease in response of the OSLD for the energies of 6 MV and 18 MV was observed, with a higher decrease for the 18 MV beams, as also observed for TLD. This result is consistent with the results of Viamonte *et al.* [13] in that there was a decrease in response of the OSLD at higher energies. Viamonte showed that for dosimeters calibrated in a ^{60}Co beam, there was an observed decrease in sensitivity of 4%, although a 4% decrease in response was observed in this study for neither 6 MV nor 18 MV.

3.3 Dosimetric Evaluation

3.3.1 Absolute Dose

Four treatment plans were developed and delivered to the RPC pelvic phantom. The three coplanar treatment plans included a 4-field box, IMRT, and VMAT. The one non-coplanar plan was a CyberKnife treatment. The phantom was irradiated three times for each plan to determine the ability of the OSLD to measure an equivalent dose to the TLD dose measurements. Each delivery included two TLD in the femoral heads, two TLD in the PTV, and two OSLD in the PTV. The OSLD in the PTV were located adjacent to the TLD, offset from the center of the target by approximately the same distance as the TLD. Only the average doses measured by the TLD and

OSLD in the PTV are reported and compared. The doses measured by the OSLD were calculated using Equation 2.7, and the TLD measured doses were calculated using Equation 2.3. The ratio of the average TLD dose to the average OSLD dose was calculated for each plan. The ratios of the TLD dose to uncorrected OSLD dose for the coplanar treatment plans can be seen below in Table 3.4. The average TLD to OSLD dose ratio and standard deviation for all coplanar deliveries in the table below was calculated to be 1.028 ± 0.008. With the exception of the dose ratio for the treatment delivery '4 field_1' the OSLD dose differs from the TLD dose by greater than 1%.

	TLD Dose (cGy)	***OSLD Dose (cGy)***	***TLD/OSLD***
4 field_1	317.0	313.9	1.010
4 field_2	317.2	309.2	1.026
4 field_3	319.3	312.7	1.021
IMRT_1	297.6	289.7	1.027
IMRT_2	298.8	289.1	1.034
IMRT_3	298.0	289.1	1.031
VMAT_1	320.4	308.3	1.039
VMAT_2	321.7	311.5	1.033
VMAT_3	319.4	310.1	1.030

Table 3.4 TLD to OSLD dose ratios for coplanar treatment plans

The angular correction factors determined from the spherical phantom irradiations, shown in Table 3.1, were applied to the OSLD calculated doses. The correction factor for coplanar 18 MV treatments of 1.019 was applied to the 4-field measured OSLD doses. The coplanar 6 MV correction factor of 1.040 was applied to the measured doses for the IMRT and VMAT deliveries. The ratios of the TLD dose to angular corrected OSLD dose for the coplanar treatment plans can be seen below in Table 3.5. The average TLD to corrected OSLD dose ratio and standard deviation for the coplanar deliveries was calculated to be 0.995 ± 0.006. For all coplanar treatment deliveries, the corrected OSLD dose is within 1% of the dose measured by the TLD, with the exception of 'IMRT_1'.

	TLD Dose (cGy)	*Corr OSLD Dose (cGy)*	*TLD/Corr OSLD*
4 field_1	317.0	319.9	0.991
4 field_2	317.2	315.1	1.007
4 field_3	319.3	318.6	1.002
IMRT_1	297.6	301.3	0.988
IMRT_2	298.8	300.7	0.994
IMRT_3	298.0	300.7	0.991
VMAT_1	320.4	320.6	0.999
VMAT_2	321.7	324.0	0.993
VMAT_3	319.4	322.5	0.990

Table 3.5 TLD to corrected OSLD dose ratios for coplanar treatment plans

The ratio of the TLD measured dose to the OSLD measured dose, without the angular correction, for the non-coplanar CyberKnife treatment deliveries can be seen below in Table 3.6. The average TLD to OSLD dose ratio and standard deviation for the non-coplanar treatments was calculated to be 1.011 ± 0.003. Each delivery resulted in an OSLD dose that differed from the TLD dose by approximately 1%.

	TLD Dose (cGy)	*OSLD Dose (cGy)*	*TLD/OSLD*
CK_1	620.3	612.4	1.013
CK_2	617.7	613.3	1.007
CK_3	621.8	613.5	1.013

Table 3.6 TLD to OSLD dose ratios for CyberKnife treatments

From the spherical phantom irradiations, the angular dependence correction factor of 1.038 for the non-coplanar 6 MV deliveries, specific to CyberKnife treatments, was applied to the OSLD doses. The ratios of the TLD measured dose to the angular corrected OSLD dose for the CyberKnife deliveries can be seen below in Table 3.7. The average TLD to corrected OSLD dose ratio and standard deviation was calculated to be 0.974 ± 0.003. Each CyberKnife treatment delivery resulted in a difference between the TLD dose and OSLD dose by greater than 1%.

	TLD Dose (cGy)	*Corr OSLD Dose (cGy)*	*TLD/Corr OSLD*
CK_1	620.3	635.7	0.976
CK_2	617.7	636.6	0.970
CK_3	621.8	636.8	0.976

Table 3.7 TLD to corrected OSLD dose ratios for CyberKnife treatments

The response of the OSLD compared to the TLD for the two institution trials was calculated by taking the ratio of the TLD dose to the OSLD dose, as done for the previous irradiations. The ratios of the doses for the institution trials, one IMRT delivery and one CyberKnife delivery, can be seen below in Table 3.8. The average TLD to OSLD dose ratio and standard deviation was calculated to be 1.040 ± 0.008. Each trial showed a response difference between the TLD and OSLD of greater than 1%.

	TLD Dose (cGy)	*OSLD Dose (cGy)*	*TLD/OSLD*
IMRT	615.6	589.1	1.045
CyberKnife	675.9	653.5	1.034

Table 3.8 TLD to OSLD dose ratios for the institution trials

Using the angular dependence correction factors employed previously, the corrected OSLD doses were calculated. The OSLD dose for the IMRT trial was multiplied by the angular correction factor of 1.040, and the CyberKnife trial OSLD dose was multiplied by the correction factor 1.038. The ratios of TLD dose to corrected OSLD dose for the two institution trials can be seen in Table 3.9. The average TLD to corrected OSLD dose ratio and standard deviation was calculated to be 1.001 ± 0.007. Both the IMRT and CyberKnife institution trials had OSLD angular corrected doses within 1% of the TLD measured doses.

	TLD Dose (cGy)	*Corr OSLD Dose (cGy)*	*TLD/Corr OSLD*
IMRT	615.6	612.1	1.006
CyberKnife	675.9	679.0	0.995

Table 3.9 TLD to corrected OSLD dose ratios for the institution trials

For each set of irradiations, with the exception of the three CyberKnife irradiations shown in Table 3.7, the applied angular correction factors corrected the OSLD dose to within 1% of the measured TLD dose, with very low error. The 6 MV non-coplanar angular correction factor, when applied to the OSLD measured dose from the CyberKnife institution trial, adequately corrected the

OSLD dose, so it is unclear as to why the correction factor failed to scale the OSLD dose appropriately for the other CyberKnife irradiations. CyberKnife treatments are very non-homogeneous in nature, so it is possible that even with the TLD and OSLD oriented in the phantom to be very close together, there could be large dose differences between the two types of dosimeters, making it difficult to compare the angular corrected OSLD dose to the TLD dose. The films present in the phantom at irradiation could be used to determine if large dose differences within the target were present, which was not possible for the three CyberKnife treatments in this study as there were no films included in the phantom for these irradiations. Another complication to the CyberKnife dose comparison is that the plans between different institutions could vary widely. The angular delivery of the MU from different plans could be very different, and result in differences in dose deposited in the OSLD.

The outcome of the absolute dose comparisons show that the coplanar 6 MV and 18 MV angular correction factors, when applied to the measured OSLD doses, yield equivalent results to the TLD measured doses, and can be used for the purpose of credentialing with the RPC's anthropomorphic QA phantoms.

3.3.2 Dose Profiles

The phantom irradiations contained film in the coronal and sagittal planes through the target for the three IMRT treatment deliveries, as well as for both institution trials, for the evaluation of the agreement between planned and measured doses. Each film was normalized to the TLD target doses, and again for the angular corrected OSLD target doses. The coronal film is evaluated by taking profiles through the PTV in both the lateral and superior-inferior directions. The sagittal film is evaluated by taking profiles through the PTV in the AP and superior-inferior directions. Selected profiles from the second IMRT delivery, 'IMRT_2', can be seen in the figures below. The lateral profile taken from the coronal film, normalized to the TLD and corrected OSLD doses can be seen in Figures 3.13 and 3.14, respectively. The AP profile recorded from the sagittal film, normalized to the TLD doses can be seen in Figure 3.15, and the profile from the film normalized to the corrected OSLD doses can be seen in Figure 3.16. The drop in measured dose at the center of the AP profile from the sagittal film is due to the gap where the edges of the two pieces of the film come together. The superior-inferior profiles taken from the sagittal film normalized to the TLD target doses and the angular corrected OSLD target doses can be seen in Figures 3.17 and 3.18, respectively. All other profiles for the IMRT and institution trial deliveries can be seen in the Appendix, in Section 5.2. The profiles display the institution reported doses from the TPS, the measured dose from the film

normalized to target dosimeter doses, and the point doses from the dosimeters in the target. These dose profiles were not evaluated for quantitative results, but rather as a qualitative analysis of the ability of the OSLD to measure equivalent dose to the TLD and provide similar results when normalizing film, when an angular dependence correction is made to the OSLD dose.

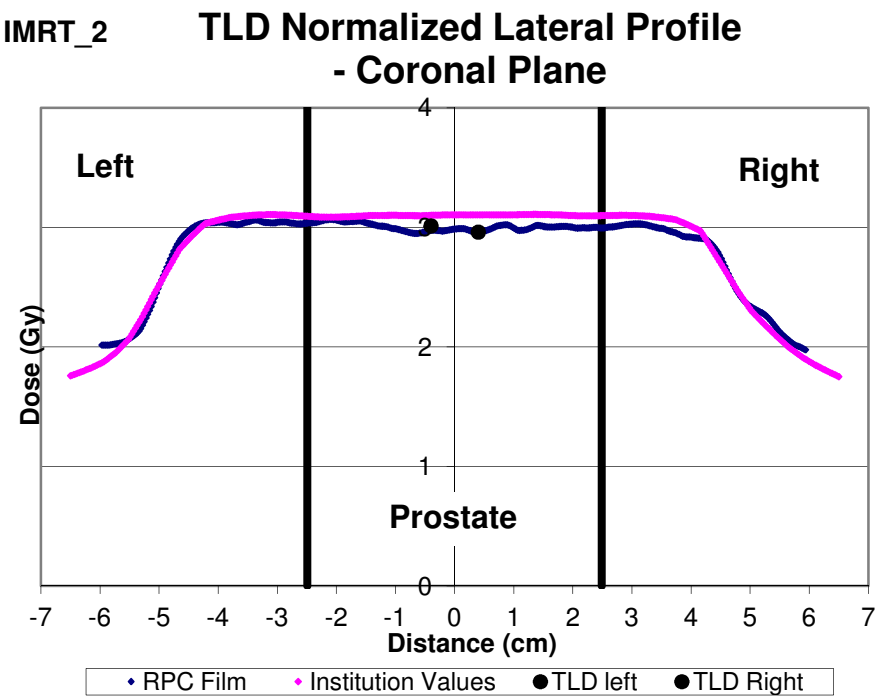

Figure 3.13 Lateral dose profile in coronal plane from IMRT_2 as planned by TPS and measured by film normalized to target TLD dose

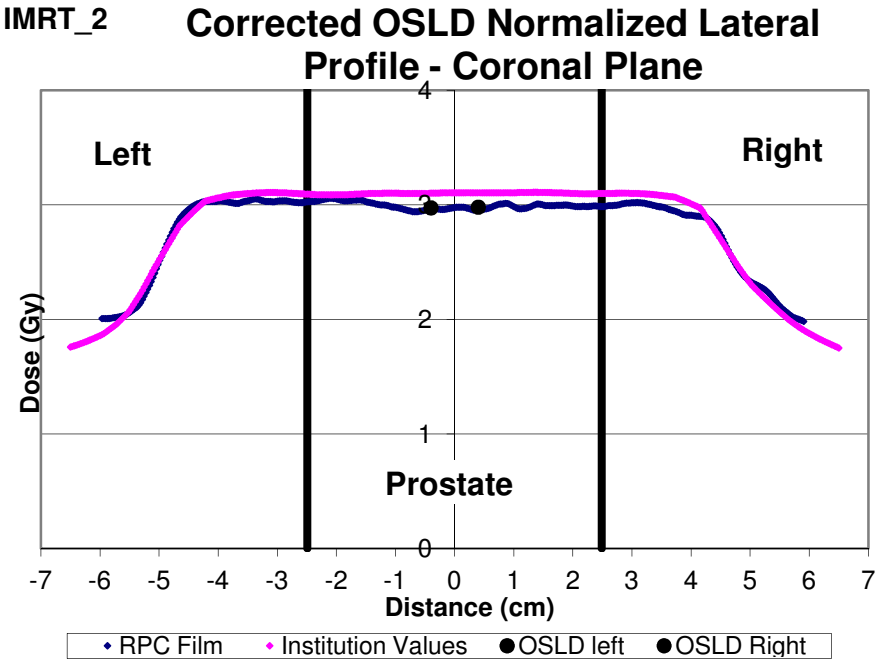

Figure 3.14 Lateral dose profile in coronal plane from IMRT_2 as planned by TPS and measured by film normalized to corrected target OSLD dose

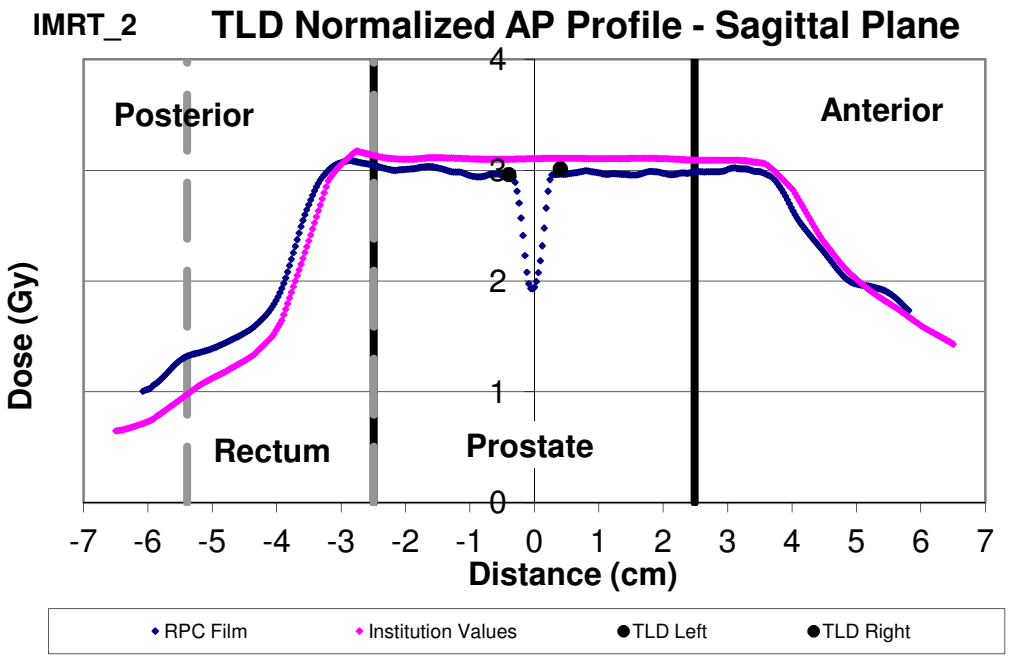

Figure 3.15 AP dose profile in sagittal plane from IMRT_2 as planned by TPS and measured by film normalized to target TLD dose

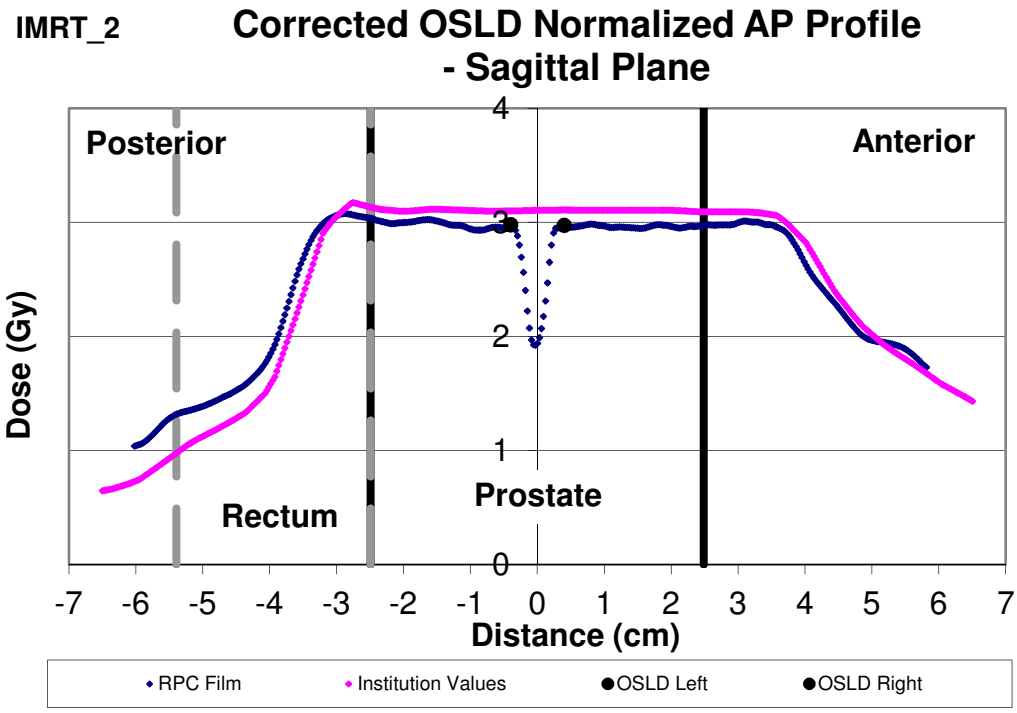

Figure 3.16 AP dose profile in sagittal plane from IMRT_2 as planned by TPS and measured by film normalized to corrected target OSLD dose

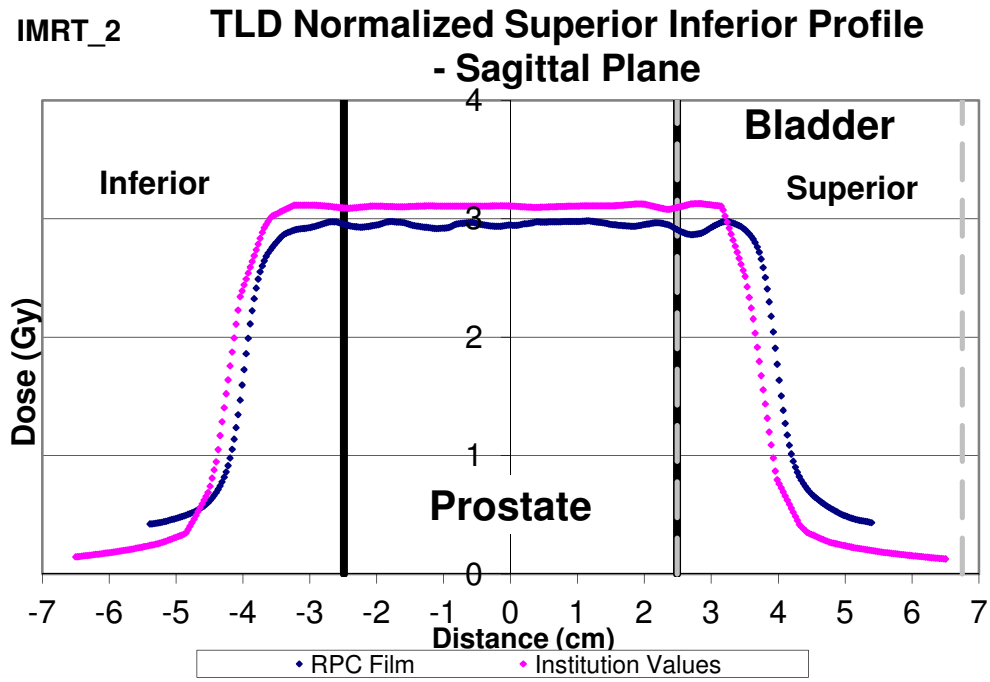

Figure 3.17 Superior-inferior dose profile in sagittal plane from IMRT_2 as planned by TPS and measured by film normalized to target TLD dose

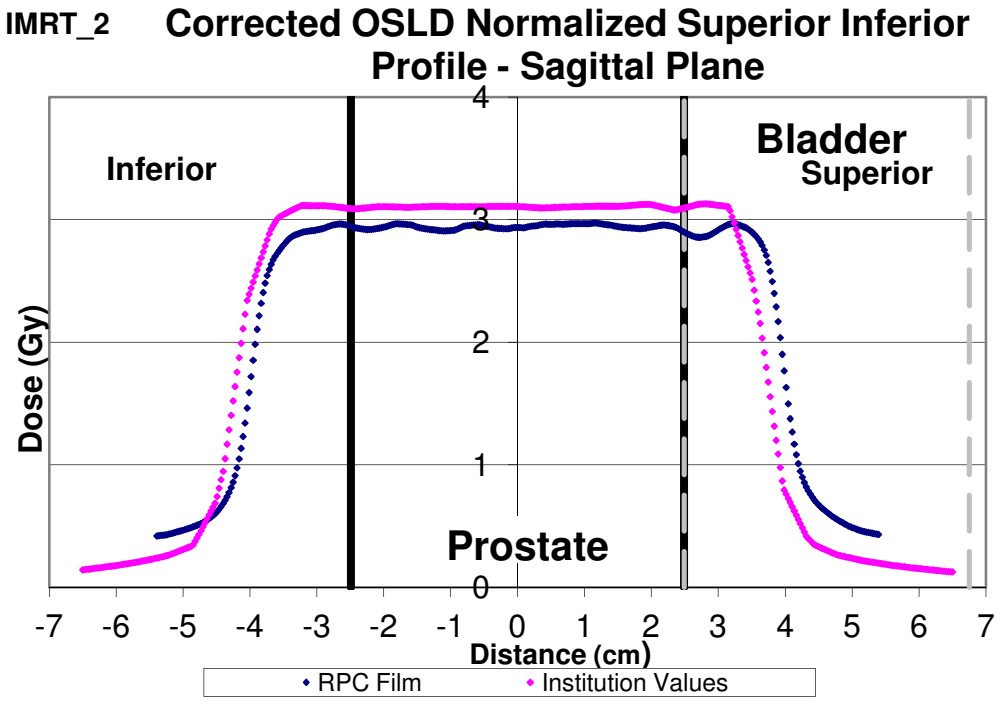

Figure 3.18 Superior-inferior dose profile in sagittal plane from IMRT_2 as planned by TPS and measured by film normalized to corrected target OSLD dose

For each film presented, the films normalized to the angular corrected OSLD target doses appear almost identical to the films normalized to the TLD target doses. While the normalized film profiles may not match up well to the institution reported profiles, as seen in the superior-inferior profiles from the sagittal films in Figures 3.17 and 3.18, the aim of this study is not to compare the OSLD doses or OSLD normalized film to the institution values, but rather to compare the TLD with the OSLD. These results validate that the film can be normalized to the angular corrected OSLD target doses for the purposes of credentialing with the RPC's anthropomorphic QA phantoms.

3.3.3 Gamma Analysis

Another method by which the ability of the OSLD, when a correction for the angular dependence is made, to measure equivalent dose to TLD measurements is evaluated was by comparing gamma analysis results for film normalized to both TLD doses and OSLD doses, as described in Section 2.7.3. The percent of pixels passing the 7%/4 mm gamma criteria for the three IMRT treatment deliveries is shown in Table 3.10. The pass rates for each film in the phantom normalized to the target TLD doses can be seen next to the pass rates for the films normalized to the angular corrected OSLD target doses. The percentage of pixels passing the same gamma criteria for the two institution trials can be seen in Table 3.11. For the purpose of this study, it is not necessary or important that the films pass the RPC gamma criteria of greater than 85% of pixels passing, but the significance rests in the ability of the OSLD normalized films to pass at the same rate as the TLD normalized films. For the three IMRT deliveries and the two institution trials, the gamma pass rates for the films normalized to both the TLD and the corrected OSLD are very close, if not the same. The low passing rates for the three IMRT deliveries can be attributed to the low dose delivered to the film. The RPC experience has shown that for a target dose of 3 Gy, the noise properties dominate the film, making accurate results difficult to obtain.

	Film	*TLD Gamma Pass Rate*	*OSLD Gamma Pass Rate*
IMRT_1	Coronal	82%	83%
	Sagittal	80%	81%
IMRT_2	Coronal	88%	88%
	Sagittal	85%	84%
IMRT_3	Coronal	82%	82%
	Sagittal	75%	75%

Table 3.10 Percent of pixels passing gamma analysis for IMRT deliveries in the coronal and sagittal films for a criteria of 7%/4 mm for film normalized to TLD dose and corrected OSLD dose

	Film	*TLD Gamma Pass Rate*	*OSLD Gamma Pass Rate*
IMRT	Coronal	100%	100%
	Sagittal	99%	99%
CyberKnife	Coronal	93%	93%
	Sagittal	94%	94%

Table 3.11 Percent of pixels passing gamma analysis for institution trials in the coronal and sagittal films for 7%/4 mm criteria for film normalized to TLD dose and corrected OSLD dose

The distribution maps, both color scale and binary, for the sagittal and coronal films with pixels passing the 7%/4 mm gamma criteria for the irradiation IMRT_2 can be seen below in Figure 3.19 through Figure 3.26. The gamma results are shown for both the TLD normalized films and the films normalized by the angular corrected OSLD doses. The gamma analysis results for the remaining IMRT deliveries and the institution trials are shown in the Appendix, in Section 5.3.

The gamma results for the coronal films from the second IMRT irradiation can be seen below, Figure 3.19 shows the coronal film normalized to the TLD target doses and Figure 3.20 shows the same film normalized to the corrected OSLD target doses. The same results, with the binary display of pixels passing can be seen below, Figure 3.21 is the result for the TLD normalized film and Figure 3.22 is the result for the angular corrected OSLD normalized film. The areas of pixels passing the gamma criteria for both the TLD and OSLD normalized films appear essentially the same.

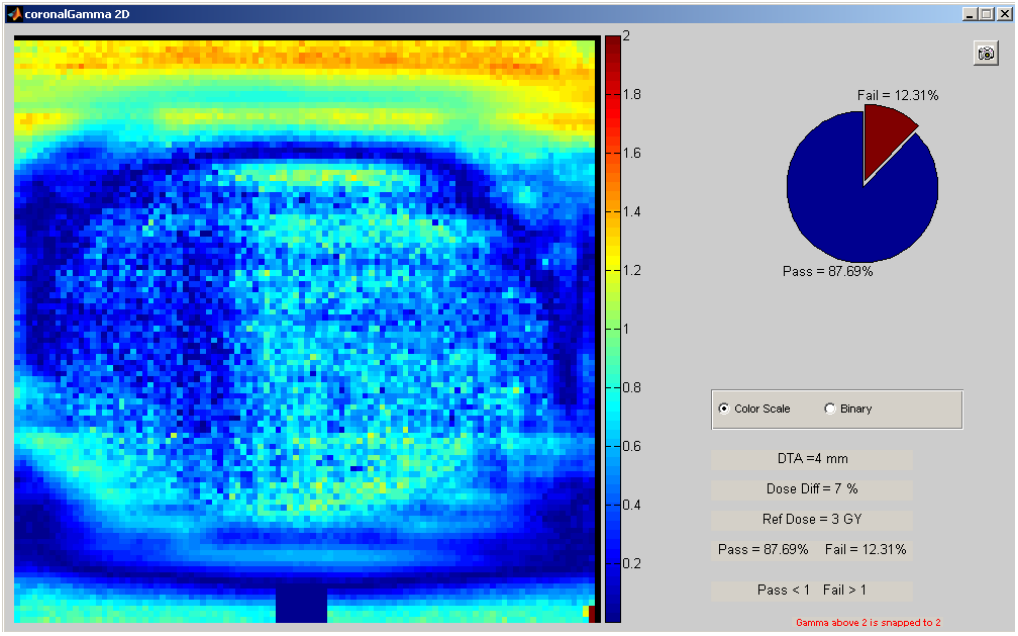

Figure 3.19 IMRT_2 color scale gamma results for coronal film normalized to target TLD dose

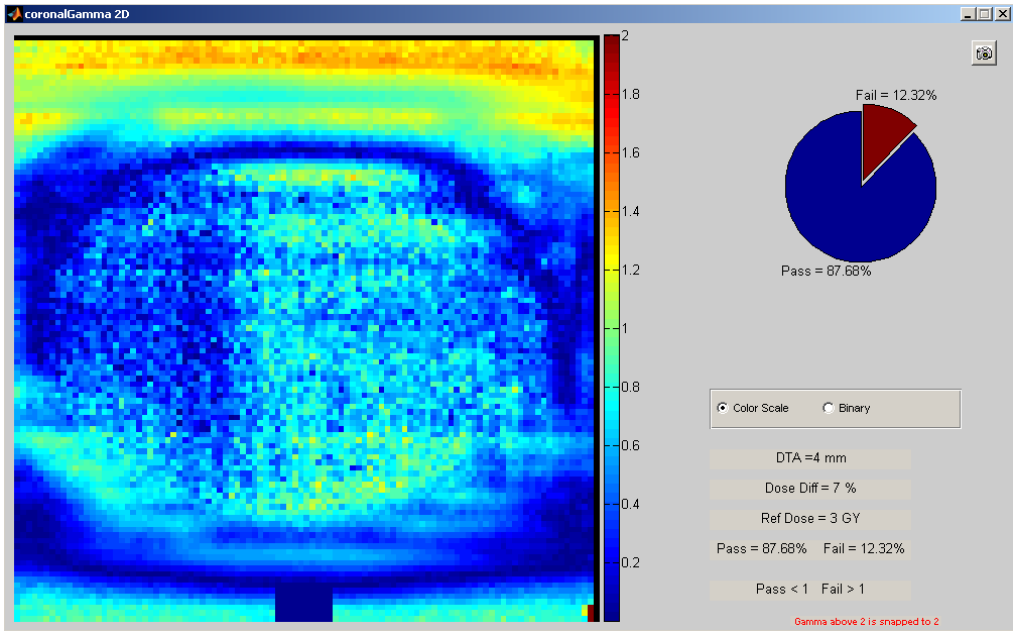

Figure 3.20 IMRT_2 color scale gamma results for coronal film normalized to corrected target OSLD dose

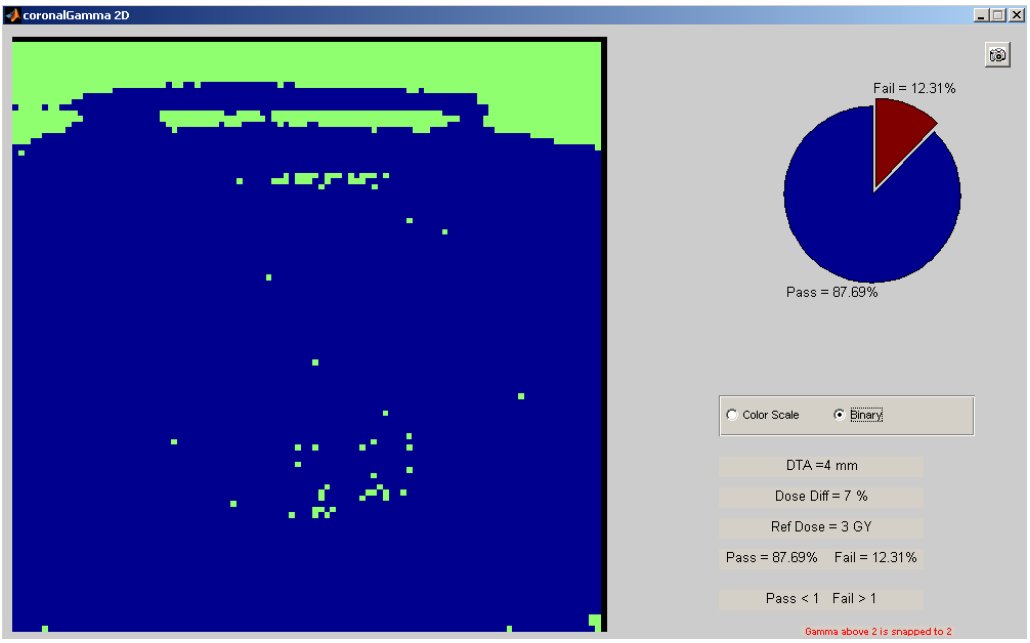

Figure 3.21 IMRT_2 binary gamma results for coronal film normalized to target TLD dose

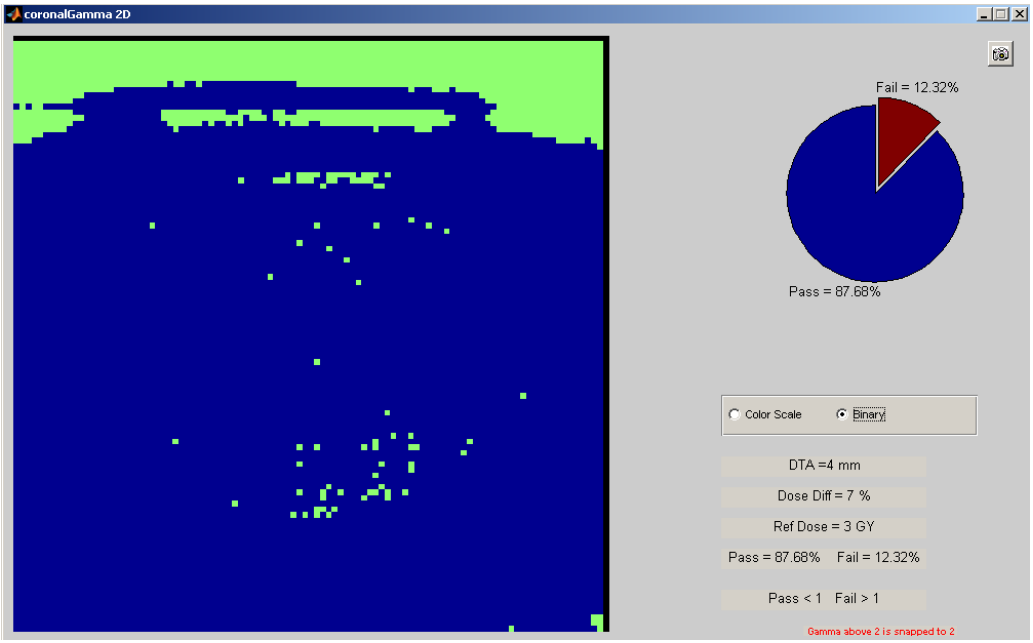

Figure 3.22 IMRT_2 binary gamma results for coronal film normalized to corrected target OSLD dose

The gamma results for the sagittal films from the second IMRT irradiation can be seen below, Figure 3.23 shows the sagittal film normalized to the TLD doses and Figure 3.24 shows the same film normalized to the corrected OSLD doses. The sagittal film gamma results shown in the binary

display, passing pixels appear blue and failing pixels appear green, can be seen below. Figure 3.25 is the result for the TLD normalized film and Figure 3.26 is the result for the angular corrected OSLD normalized film. The areas of pixels passing the gamma criteria for both the TLD and OSLD normalized films appear the same, with few variations.

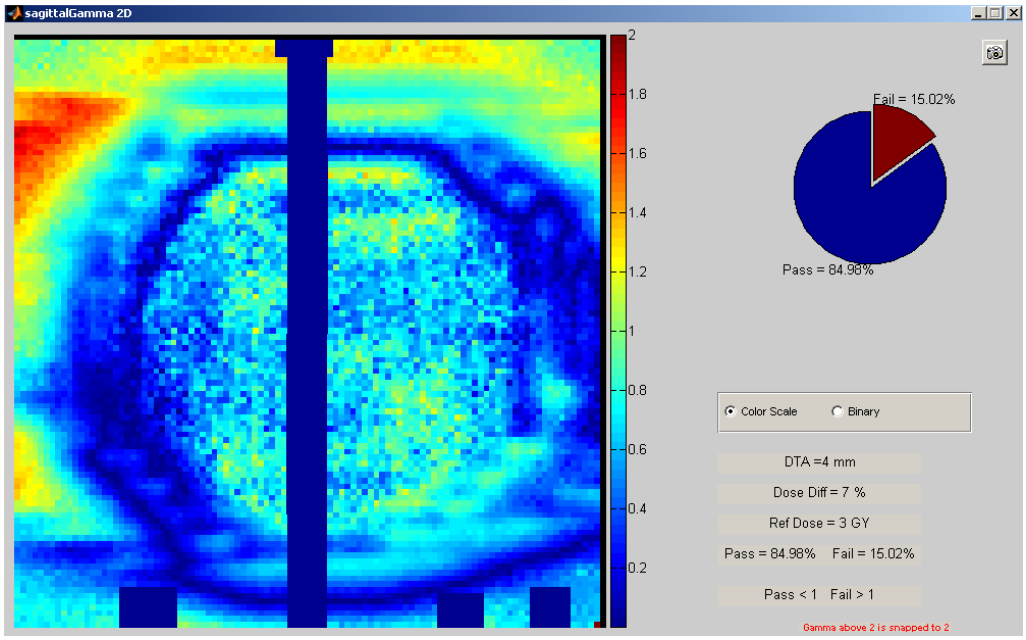

Figure 3.23 IMRT_2 color scale gamma results for sagittal film normalized to target TLD dose

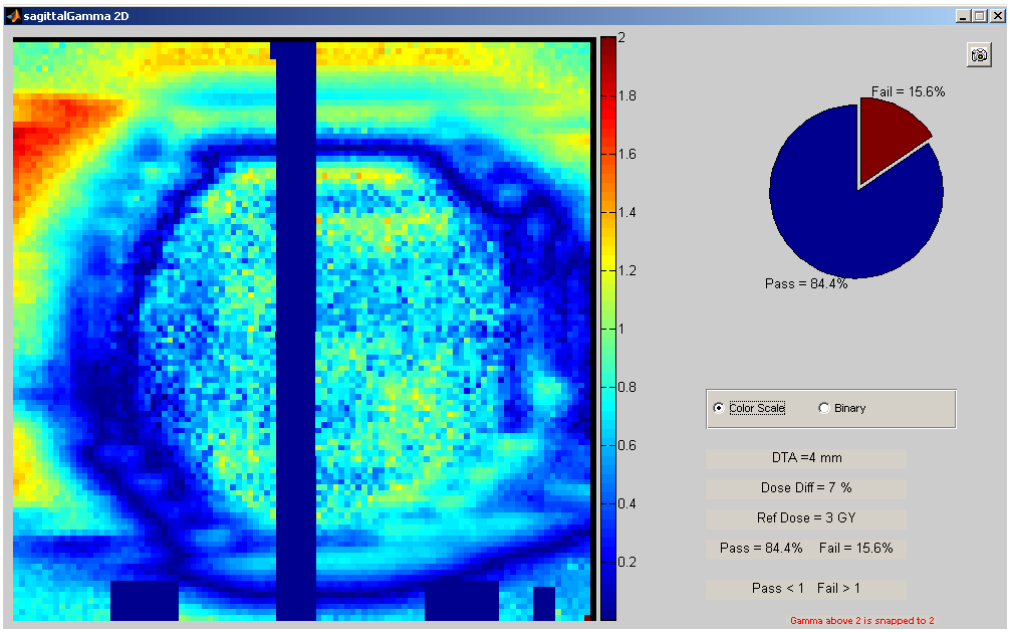

Figure 3.24 IMRT_2 color scale gamma results for sagittal film normalized to corrected target OSLD dose

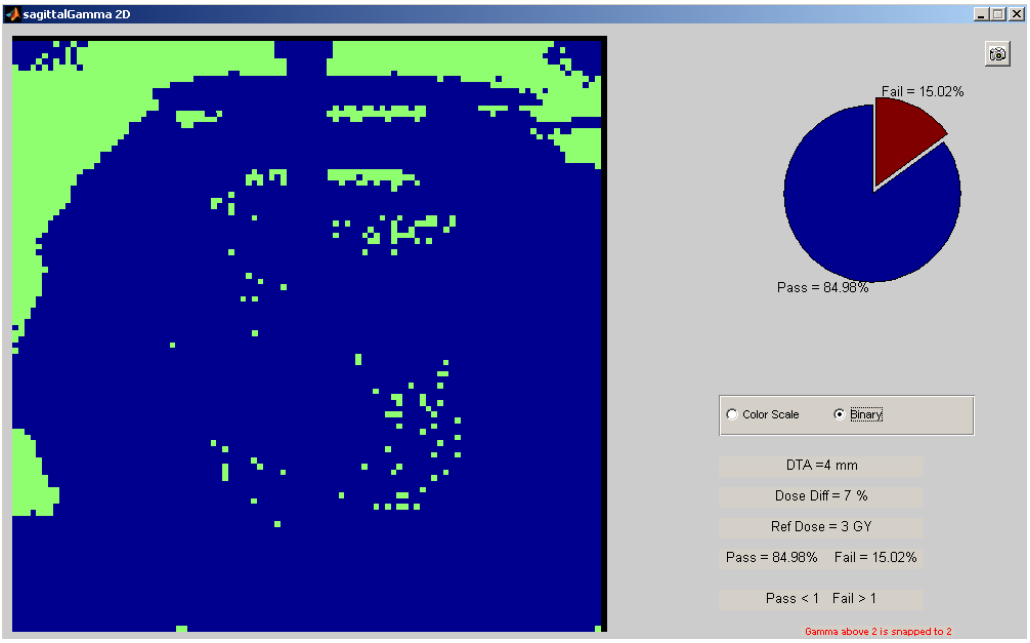

Figure 3.25 IMRT_2 binary gamma results for sagittal film normalized to target TLD dose

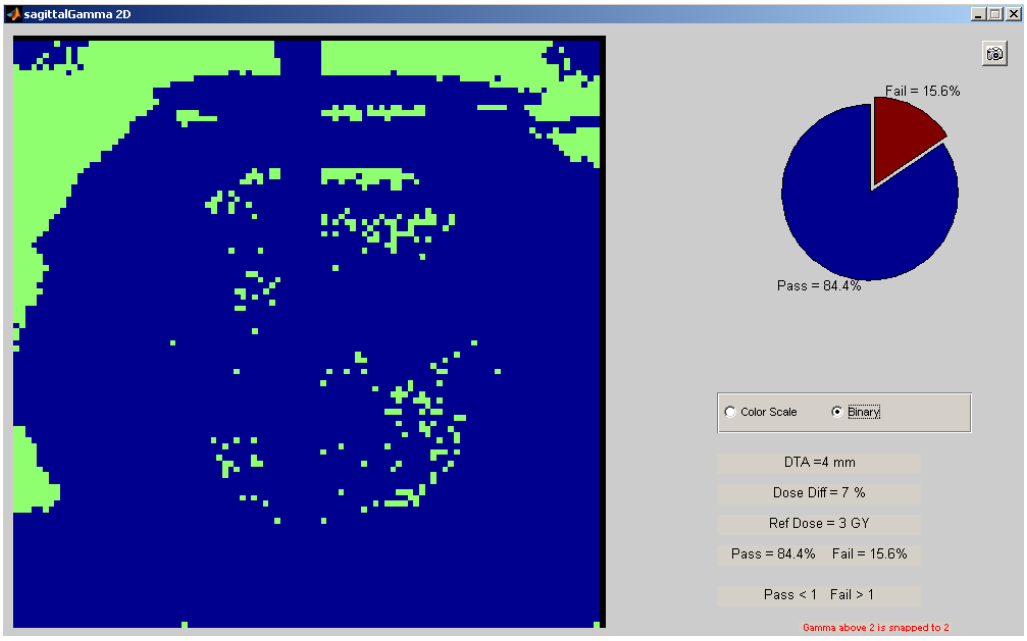

Figure 3.26 IMRT_2 binary gamma results for sagittal film normalized to corrected target OSLD dose

The results from the gamma analysis, comparing the pass rates and pixel distributions of the TLD normalized films and the corrected OSLD normalized films, demonstrate that the analysis of the films when normalized to the angular corrected OSLD target doses yields equivalent results to the

TLD normalized films. The films normalized to the angular corrected OSLD target doses can be used for the purpose of credentialing with the RPC's anthropomorphic QA phantoms.

Chapter 4 Conclusions

4.1 Conclusion

This study investigated the angular dependence of the nanoDot OSL dosimeters in the RPC pelvic phantom to effectively utilize the OSLD as a replacement for the TLD in the anthropomorphic QA phantoms. The replacement of TLD in the QA phantoms with OSLD would be beneficial to the RPC. The benefits of OSLD include shorter waiting periods post-irradiation, simpler and quicker readout procedures, minimal energy dependence, signal is not destroyed when they are read, allowing them to be read multiple times, and they are not affected by environmental changes. As the mini-phantom portion of the remote audit system has already made the switch to OSLD, the switch from TLD to OSLD in the anthropomorphic phantoms would further streamline the remote audit process and greatly improve efficiency.

OSLD were irradiated within a small, spherical polystyrene phantom to study the angular dependence of the dosimeters under the simplest of conditions for both 6 MV and 18 MV photon beams. The results of these irradiations lead to the determination of angular correction factors of 1.040 and 1.019 for coplanar treatments with beam energies 6 MV and 18 MV, respectively, and a correction factor of 1.038 for non-coplanar treatments at 6 MV, specific to CyberKnife treatments. Within the experimental uncertainties, the correction factors at 6 MV for the coplanar and non-coplanar treatments are essentially the same.

The irradiations of the RPC pelvic phantom included TLD, OSLD, and film for the IMRT and institution trials. The film was included in the select treatments in order to validate the use of OSLD dose, when the angular dependence has been corrected, to normalize the film for obtaining dose profiles or performing gamma analysis, and to show that the OSLD normalized film yields the same results as film normalized by the TLD doses. Comparisons of the absolute doses measured by the TLD and OSLD, the dose profiles generated by normalized films, and gamma analysis of the normalized films were all performed. The ratio of the doses measured by the TLD to the corrected OSLD measured dose was calculated to be 0.995 ± 0.006 for the coplanar treatment deliveries. The ratio of the TLD measured doses to the angular corrected OSLD doses for the non-coplanar treatment deliveries was calculated to be 0.974 ± 0.003. The institution trials served as a method to verify the ability of the angular correction factors established from the spherical phantom irradiations to correct the OSLD dose to within 1% of the TLD measured dose. The average ratio of the TLD to corrected OSLD dose for the two institution trials was calculated to be 1.001 ± 0.007. For all irradiations, the angular dependence correction factors determined in this study effectively corrected the OSLD

measured dose to within 1% of the TLD measured dose, with the exception of the three CyberKnife treatment deliveries.

Our hypothesis, that the incorporation of OSLD into the RPC phantom will measure on average an equivalent dose measurement as compared to the existing TLD measurements within ±1%, regardless of the angular dependence of the OSLD, was not supported. Based on the results of the study, the OSLD can be effectively used as a replacement for the TLD in the phantoms and measure an equivalent dose within 1%, only if the OSLD angular dependence is first corrected.

Caution is advised regarding the use of the angular dependence correction factor for the OSLD determined in this study for non-coplanar CyberKnife treatment deliveries. The discrepancies between the data from the three CyberKnife treatments delivered at St. Luke's compared to the CyberKnife irradiation for the institution trial were considerable, and the correction factor that worked so well when applied to the trial data, did not yield good results when applied to the original CyberKnife data. In addition, the statistical analysis of the OSLD responses from the non-coplanar 6 MV spherical phantom irradiations showed that averaging the normalized responses might not be the appropriate method of establishing the angular dependence correction factor. A single correction factor for the established angular dependence of the OSLD for CyberKnife irradiations may not be possible due to the high dose gradients and inherent inhomogeneities of the treatment, and that CyberKnife credentialing may need to be performed according to the current method of using TLD as the absolute dosimeter. If a switch from TLD to OSLD is pursued for CyberKnife credentialing using the anthropomorphic QA phantoms, further investigation of an appropriate angular dependence correction factor must be performed.

4.2 Future Work

The results of this study indicate that the modification of the collection of pelvic phantoms at the RPC could begin to include OSLD as a replacement for the TLD for coplanar treatment deliveries in both the PTV as well as in the femoral heads. An investigation of other anthropomorphic QA phantoms for which the inclusion of OSLD would be most appropriate, and how the modifications would be made could also be done. With the incorporation of the OSLD into the phantoms, the characterization of the energy correction factors for the OSLD in full phantom conditions must be completed for additional beam energies, both photon and electron beams.

It is also clear from this study that further research regarding the OSLD response for non-coplanar treatments, such as CyberKnife, and a possible correction factor for the OSLD angular

dependence in these situations, must be pursued. This further study of the dosimeter response for non-coplanar CyberKnife treatments might be more feasible when the RPC has credentialed a greater number of CyberKnife treatments using the existing method of mailable phantoms with TLD, but also including OSLD in the target volume and collecting data on the measured doses.

Chapter 5 Appendix

5.1 TG-21 Worksheets

Worksheet (1) for calculating the cavity-gas calibration factor N_{gas}

Name: JB Date: 3/22/2012

The cavity gas calibration factor is obtained from Eq. (6):

$$N_{gas} = N_X \frac{k\,(W/e) A_{ion}\, A_{wall}\, \beta_{wall}}{\alpha(\bar{L}/\rho)^{wall}_{air}(\bar{\mu}_{en}/\rho)^{air}_{wall} + (1-\alpha)(\bar{L}/\rho)^{cap}_{air}(\bar{\mu}_{en}/\rho)^{air}_{cap}}.$$

When chamber wall and buildup cap are of the same material, $\alpha = 1.00$.
When chamber wall and buildup cap are of different materials, α is obtained from Fig. 1.

1. (a) Chamber model and serial number: Exradin A12, SN 178
   (b) Cavity inside diameter: 6.2 mm
   (c) Wall material and thickness: 0.088 g/cm²
   (d) Buildup cap material and total wall plus cap thickness: 0.493 g/cm²
   (e) Polarizing potential: 300 V

2. (a) Calibration laboratory and date: MDACC ADCL 9/22/2010
   (b) Cobalt-60 exposure calibration factor at 22 °C and 1 atmosphere:
   $N_X =$ 5.259x10⁹ R/C
   or $N_X =$ _____ R/scale division

3. (a) Charge per unit mass of air per unit exposure: $k = 2.58 \times 10^{-4}$ C/kg R
   (b) Average energy per unit charge: $W/e = 33.7$ J/C
   (c) Absorbed dose/collision fraction of kerma: $\beta_{wall} = 1.005$

4. (a) Ion-collection efficiency (obtained from NBS or ADCL, Sec. III D): $A_{ion} =$ _____
   (b) Wall-correction factor (Tables II or III): $A_{wall} =$ _____
   (c) Fraction of ionization due to electrons from chamber wall (Fig. 1): $\alpha =$ _____
   (d) Stopping-power ratio, wall/air (Table I): $(\bar{L}/\rho)^{wall}_{air} =$ _____
   (e) Energy-absorption coefficient ratio, air/wall (Table I): $(\bar{\mu}_{en}/\rho)^{air}_{wall} =$ _____
   (f) Fraction of ionization due to electrons from buildup cap: $(1-\alpha) =$ _____
   (g) Stopping-power ratio, cap/air (Table I): $(\bar{L}/\rho)^{cap}_{air} =$ _____
   (h) Energy-absorption coefficient ratio, air/cap (Table I): $(\bar{\mu}_{en}/\rho)^{air}_{cap} =$ _____

5. Cavity-gas calibration factor at 22 °C and 1 atmosphere:
   $N_{gas} =$ 4.554x10⁹ Gy/C
   or $N_{gas} =$ _____ Gy/scale division

$\frac{N_{gas}}{N_X} = 0.8666$ specific to ion chamber

Worksheet (2) for calculating the dose to water at d_{max} from photon beams

Name: JB Date: 3/22/2012

1. Radiation source: ACB 5; Stated energy: 6 MeV
   Ionization ratio: 0.671 Nominal accelerating potential: 5 MV
   (Sec. IV B) (Fig. 3)
   TMR20/TMR10

2. Phantom material (med): polystyrene SSD: 100 cm
   Collimator field size: 10 x 10 cm²; Depth of measurement: 10 cm

3.1. Dose to phantom material per monitor unit [Eq. (9)]:

$$D_{med}/U = (\overline{M/U})\, N_{gas} (\overline{L}/\rho)^{med}_{air} P_{wall} P_{ion} P_{repl},$$

where U refers to accelerator monitor units, or time for a ^{60}Co unit.

3.2. The chamber temperature T = 23.5 °C and pressure P = 758.7 mmHg at the time of measurement. The chamber signal M is normalized to 22 °C and 1 atmosphere using the factor:

$$K_{TP} = \frac{T + 273\ °C}{295\ °C} \times \frac{760\ mmHg}{P} = 1.007$$

3.3. Mean chamber signal per monitor unit (at the higher collecting potential, and normalized to 22 °C and 760 mmHg)

avg read: $\left(\frac{26.69 + 26.68 + 26.68}{3}\right)\left(\frac{1.007}{200\ MU}\right)$

$(\overline{M/U})$ = _____ C/monitor unit

or $(\overline{M/U})$ = 0.1344 scale division/monitor unit nC/MU

3.4. Cavity-gas calibration factor:
Chamber model: Exradin A12 Wall material: C-552
Inner diameter: 6.2 mm Wall thickness: 0.088 g/cm²
N_{gas} = 4.554 x 10⁹ Gy/C or Gy/scale division.

3.5. Stopping-power ratio (Fig. 2, Table IV): $(\overline{L}/\rho)^{med}_{air}$ = 1.106

3.6. Wall correction factor [Eq. (10)]:

$$P_{wall} = \frac{[\alpha(\overline{L}/\rho)^{wall}_{air}(\bar{\mu}_{en}/\rho)^{med}_{wall} + (1-\alpha)(\overline{L}/\rho)^{med}_{air}]}{(\overline{L}/\rho)^{med}_{air}} = 0.9644$$

Fraction of ionization from chamber wall (Fig. 7): α = 0.40

If $\alpha \geq 0.25$, enter α and $(1-\alpha)$. $(1-\alpha)$ = 0.60
If $\alpha < 0.25$, enter $\alpha = 0$ and proceed to 4.

Stopping-power ratio (Fig. 2, Table IV): $(\overline{L}/\rho)^{wall}_{air}$ = 0.994

Energy-absorption coefficient ratio (Table IX):

$(\bar{\mu}_{en}/\rho)^{med}_{air}$ 1.072 ÷ $(\bar{\mu}_{en}/\rho)^{wall}_{air}$ 1.000 = $(\bar{\mu}_{en}/\rho)^{med}_{wall}$ 1.072

4. Ionization recombination correction (Sec. IV C and Fig. 4): P_{ion} = 1.003

5. Replacement (gradient) correction (Fig. 5): P_{repl} = 0.993

6. Dose to phantom material per monitor unit or per unit time,‖ at point of measurement: D_{med}/U = 0.6502 Gy/monitor unit

7.1. Dose to water per monitor unit, at d_{max} [Eq. (17)]:

$$D_{water}(\text{at } d_{max})/U = \frac{(D_{med}/U) \times ESC \times (\bar{\mu}_{en}/\rho)^{water}_{med}}{P/100}$$

7.2. Correction for excess scatter from acrylic phantoms (Table XIV): ESC = N/A polystyrene

7.3. Energy-absorption coefficient ratio (Table XII): $(\bar{\mu}_{en}/\rho)^{water}_{med}$ = 1.036

7.4. Percent depth dose at depth of measurement: P = 66.3 %

7.5. Dose to water per monitor unit, at d_{max}: $D_{water}(\text{at } d_{max})/U$ = 1.016 Gy/monitor unit

‖ Cobalt-60 units may have a nonlinear relationship between dose per unit time and time, especially for short exposure times. Corrections should be made using the method of Orton and Siebert (Ref. 58).

Dose to muscle/MU (@dmax) = 1.016 (0.99) = 1.006 cGy/MU

Worksheet (2) for calculating the dose to water at d_{max} from photon beams

Name: JB Date: 3/22/2012

1. Radiation source: ACB 5; Stated energy: 18 MeV
   Ionization ratio: 0.785 (Sec. IV B) Nominal accelerating potential: 17 (Fig. 3) MV
2. Phantom material (med): polystyrene SSD: 100 cm
   Collimator field size: 10 x 10 cm²; Depth of measurement: 10 cm

3.1. Dose to phantom material per monitor unit [Eq. (9)]:

$$D_{med}/U = (\overline{M/U})\, N_{gas} (\overline{L}/\rho)^{med}_{air} P_{wall} P_{ion} P_{repl},$$

where U refers to accelerator monitor units, or time for a ^{60}Co unit.

3.2. The chamber temperature $T =$ 23.5 °C and pressure $P =$ 758.7 mmHg at the time of measurement. The chamber signal M is normalized to 22 °C and 1 atmosphere using the factor:

$$\frac{T + 273\ °C}{295\ °C} \times \frac{760\ mmHg}{P} = 1.007$$

3.3. Mean chamber signal per monitor unit (at the higher collecting potential, and normalized to 22 °C and 760 mmHg)

$\frac{(31.85 + 31.84 + 31.84)}{3} / 200 \times (1.007)$

$(\overline{M/U}) =$ _____ C/monitor unit

or $(\overline{M/U}) =$ 0.1603 scale division/monitor unit nC/MU

3.4. Cavity-gas calibration factor:
Chamber model: Exradin A12 Wall material: C-552
Inner diameter: 6.2 mm Wall thickness: 0.088 g/cm²
$N_{gas} =$ 4.554×10^{9} Gy/C or Gy/scale division.

3.5. Stopping-power ratio (Fig. 2, Table IV): $(\overline{L}/\rho)^{med}_{air} =$ 1.079

3.6. Wall correction factor [Eq. (10)]:

$$P_{wall} = \frac{[\alpha(\overline{L}/\rho)^{wall}_{air}(\overline{\mu}_{en}/\rho)^{med}_{wall} + (1-\alpha)(\overline{L}/\rho)^{med}_{air}]}{(\overline{L}/\rho)^{med}_{air}} = 1.000$$

Fraction of ionization from chamber wall (Fig. 7): $\alpha =$ 0.18 → 0

If $\alpha \geq 0.25$, enter α and $(1-\alpha)$. $(1-\alpha) =$ 0.82 → 1
If $\alpha < 0.25$, enter $\alpha = 0$ and proceed to 4.

Stopping-power ratio (Fig. 2, Table IV): $(\overline{L}/\rho)^{wall}_{air} =$ 0.968

Energy-absorption coefficient ratio (Table IX):

$(\overline{\mu}_{en}/\rho)^{med}_{air}$ _____ ÷ $(\overline{\mu}_{en}/\rho)^{wall}_{air}$ _____ = $(\overline{\mu}_{en}/\rho)^{med}_{wall}$ _____

4. Ionization recombination correction (Sec. IV C and Fig. 4): $P_{ion} =$ 1.006
5. Replacement (gradient) correction (Fig. 5): $P_{repl} =$ 0.995
6. Dose to phantom material per monitor unit or per unit time,‖ at point of measurement: $D_{med}/U =$ 0.7884 Gy/monitor unit

7.1. Dose to water per monitor unit, at d_{max} [Eq. (17)]:

$$D_{water}(\text{at } d_{max})/U = \frac{(D_{med}/U) \times ESC \times (\overline{\mu}_{en}/\rho)^{water}_{med}}{P/100}$$

7.2. Correction for excess scatter from acrylic phantoms (Table XIV): ESC = N/A

7.3. Energy-absorption coefficient ratio (Table XII): $(\overline{\mu}_{en}/\rho)^{water}_{med} =$ 1.051

7.4. Percent depth dose at depth of measurement: $P =$ 80.7 %

7.5. Dose to water per monitor unit, at d_{max}: $D_{water}(\text{at } d_{max})/U =$ 1.027 Gy/monitor unit

‖ Cobalt-60 units may have a nonlinear relationship between dose per unit time and time, especially for short exposure times. Corrections should be made using the method of Orton and Siebert (Ref. 58).

Dose to muscle/MU @ d_{max} = 1.027 (0.99) = 1.017 cGy/MU

5.2 Dose Profiles

5.2.1 IMRT_1

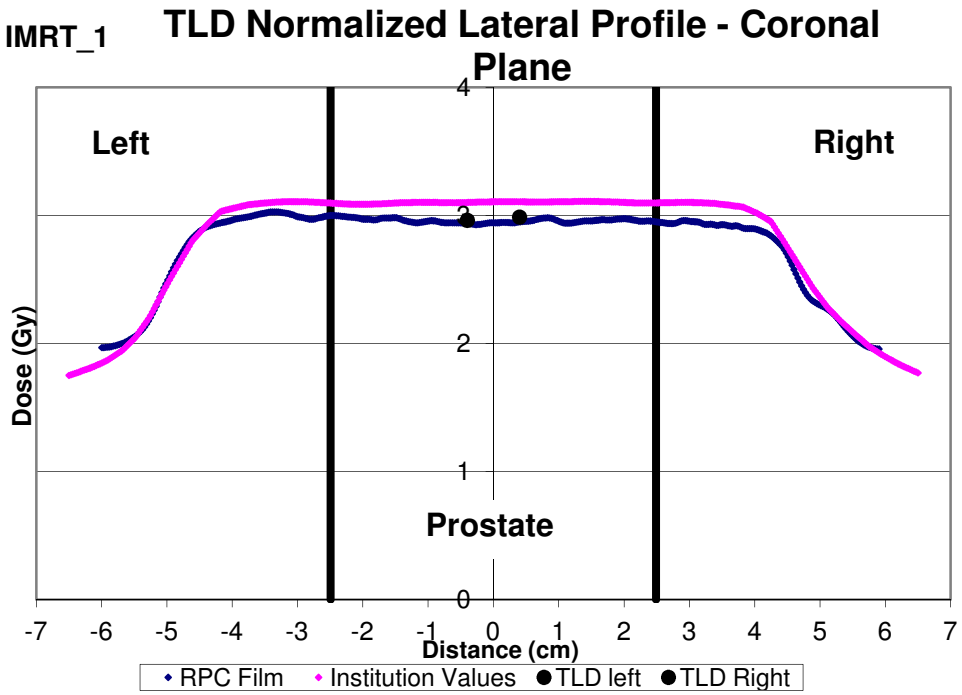

Figure 5.1 Lateral dose profile in coronal plane from IMRT_1 with film normalized to TLD dose

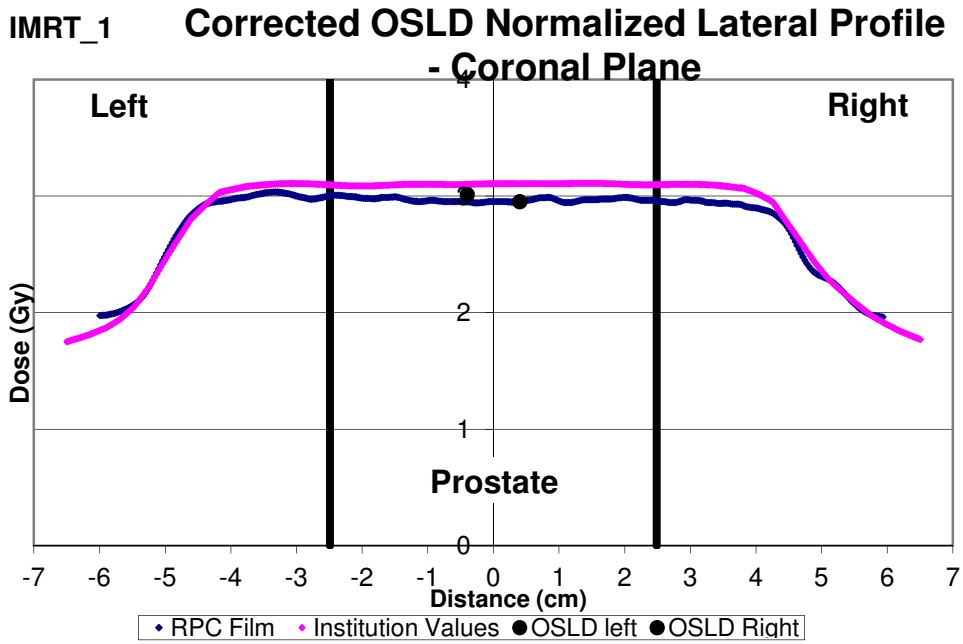

Figure 5.2 Lateral dose profile in coronal plane from IMRT_1 with film normalized to corrected OSLD dose

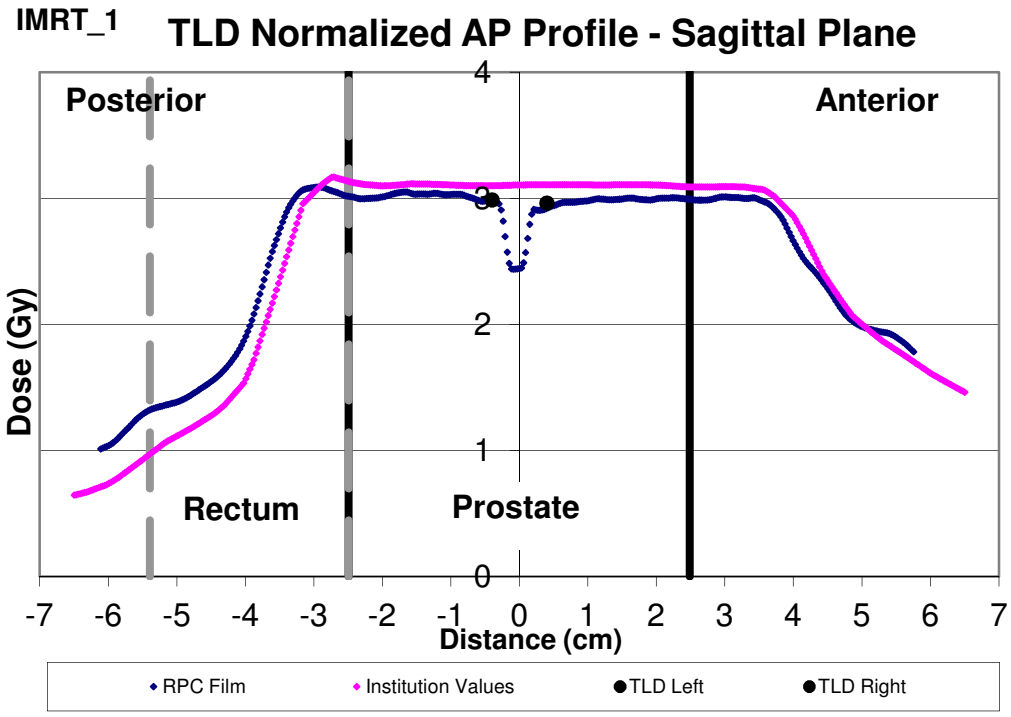

Figure 5.3 AP dose profile in sagittal plane from IMRT_1 with film normalized to TLD dose

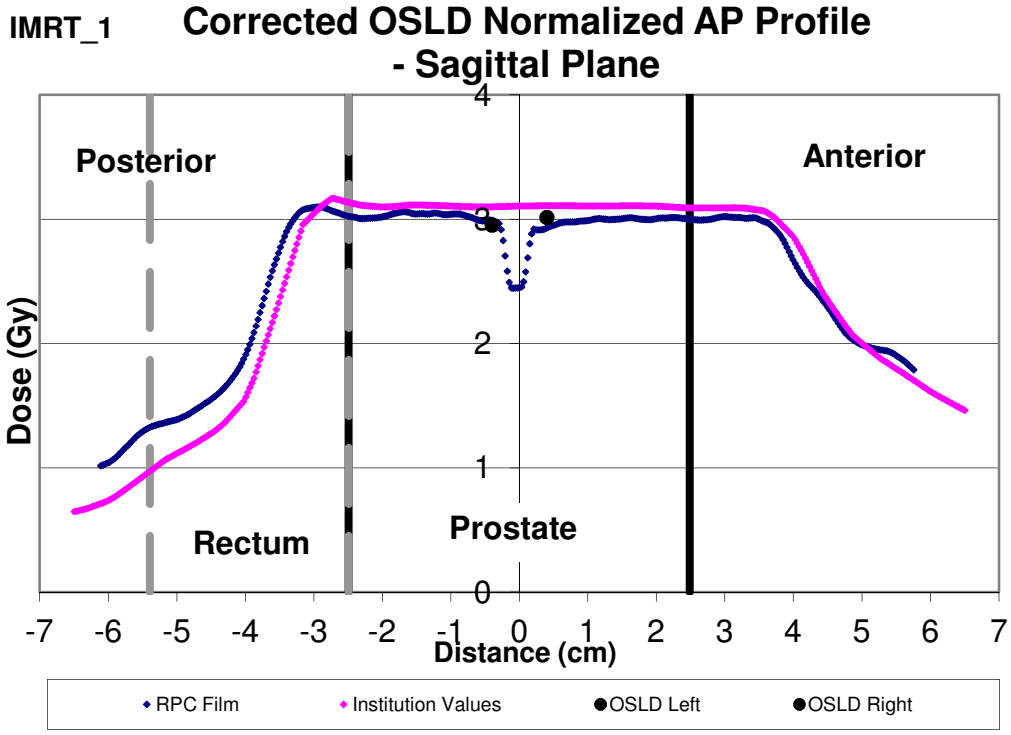

Figure 5.4 AP dose profile in sagittal plane from IMRT_1 with film normalized to corrected OSLD dose

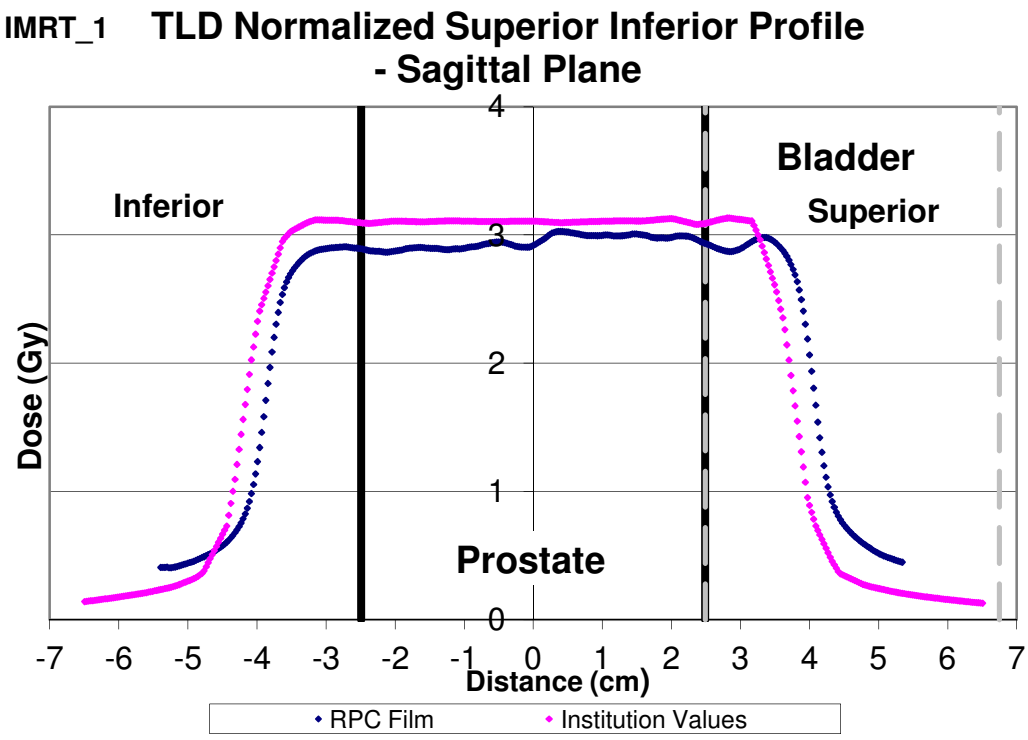

Figure 5.5 Superior-inferior dose profile in sagittal plane from IMRT_1 with film normalized to TLD dose

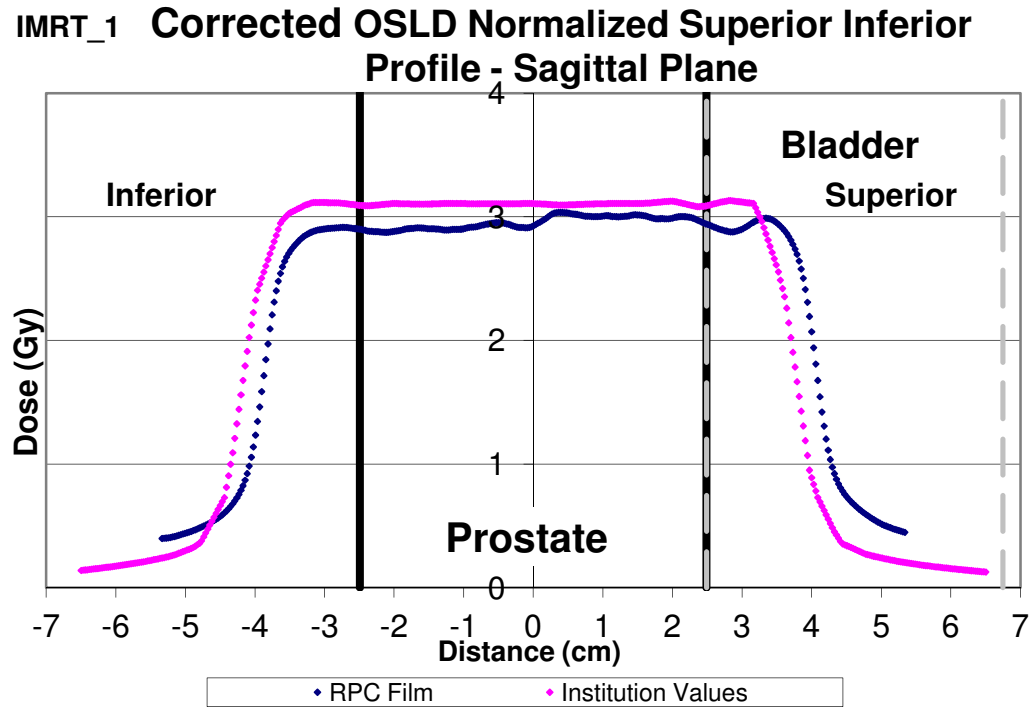

Figure 5.6 Superior-inferior dose profile in sagittal plane from IMRT_1 with film normalized to corrected OSLD dose

5.2.2 IMRT_3

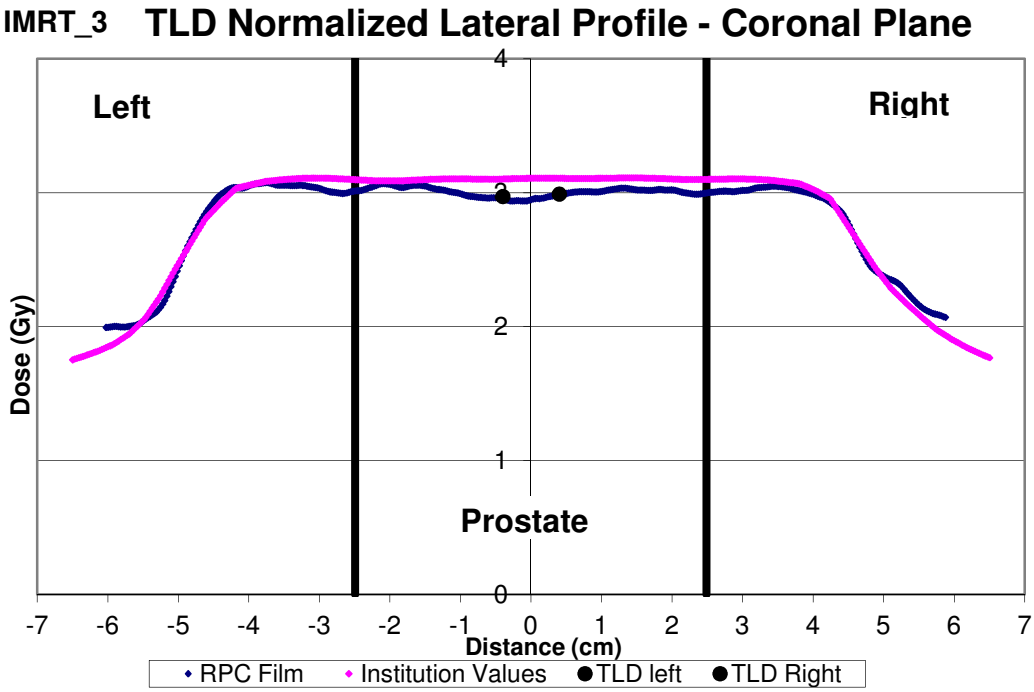

Figure 5.7 Lateral dose profile in coronal plane from IMRT_3 with film normalized to TLD dose

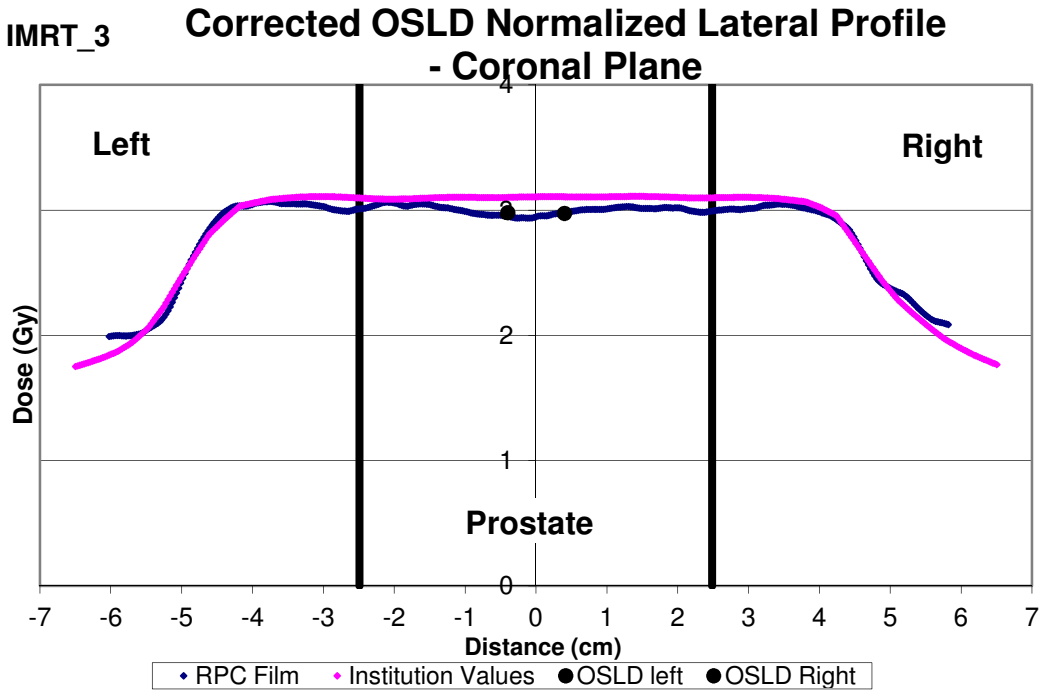

Figure 5.8 Lateral dose profile in coronal plane from IMRT_3 with film normalized to corrected OSLD dose

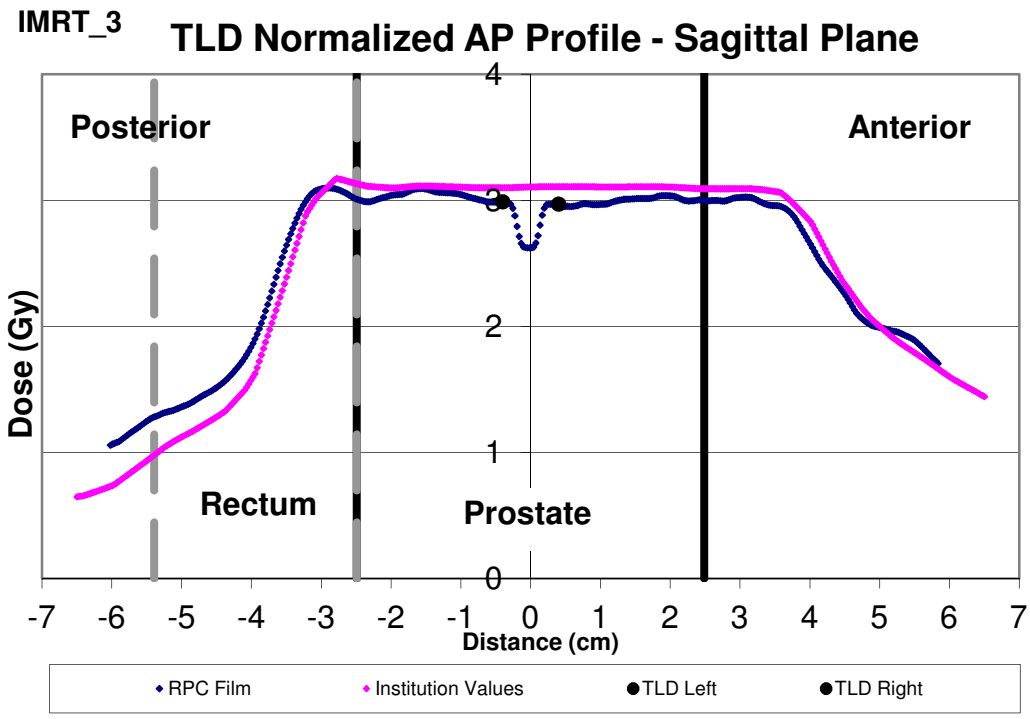

Figure 5.9 AP dose profile in sagittal plane from IMRT_3 with film normalized to TLD dose

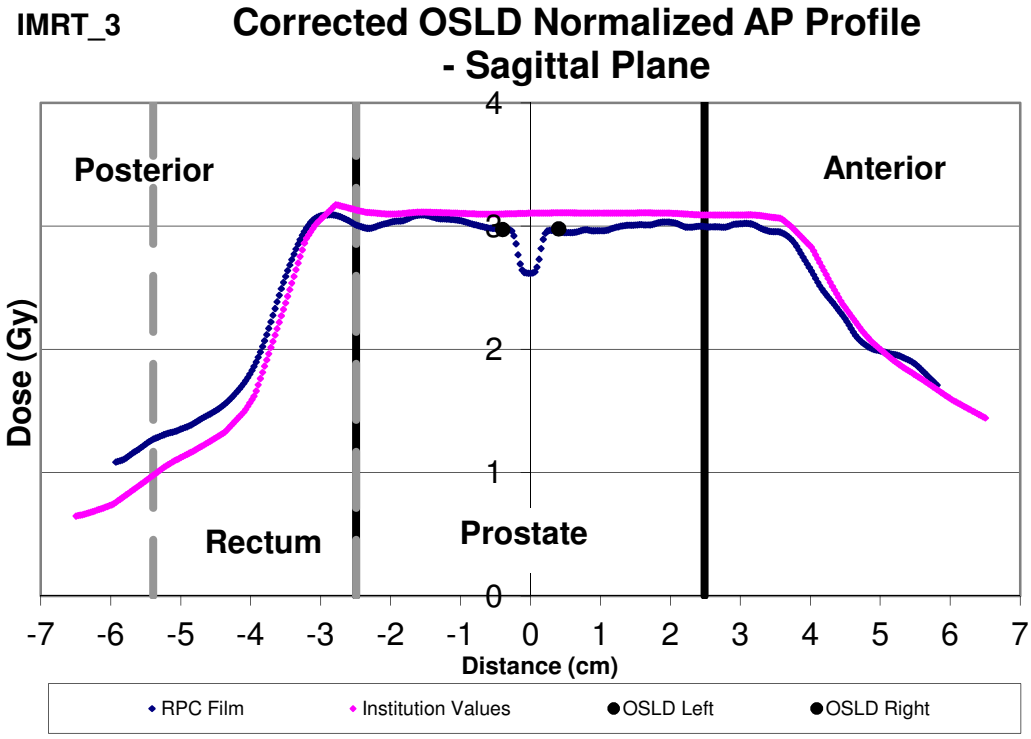

Figure 5.10 AP dose profile in sagittal plane from IMRT_3 with film normalized to corrected OSLD dose

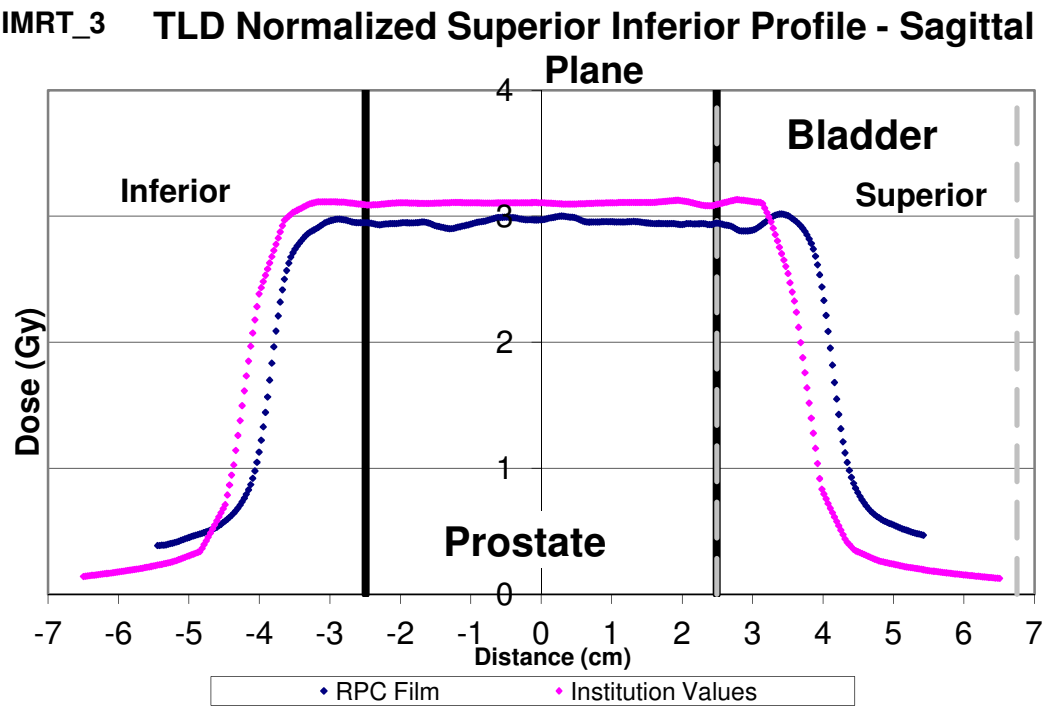

Figure 5.11 Superior-inferior dose profile in sagittal plane from IMRT_3 with film normalized to TLD dose

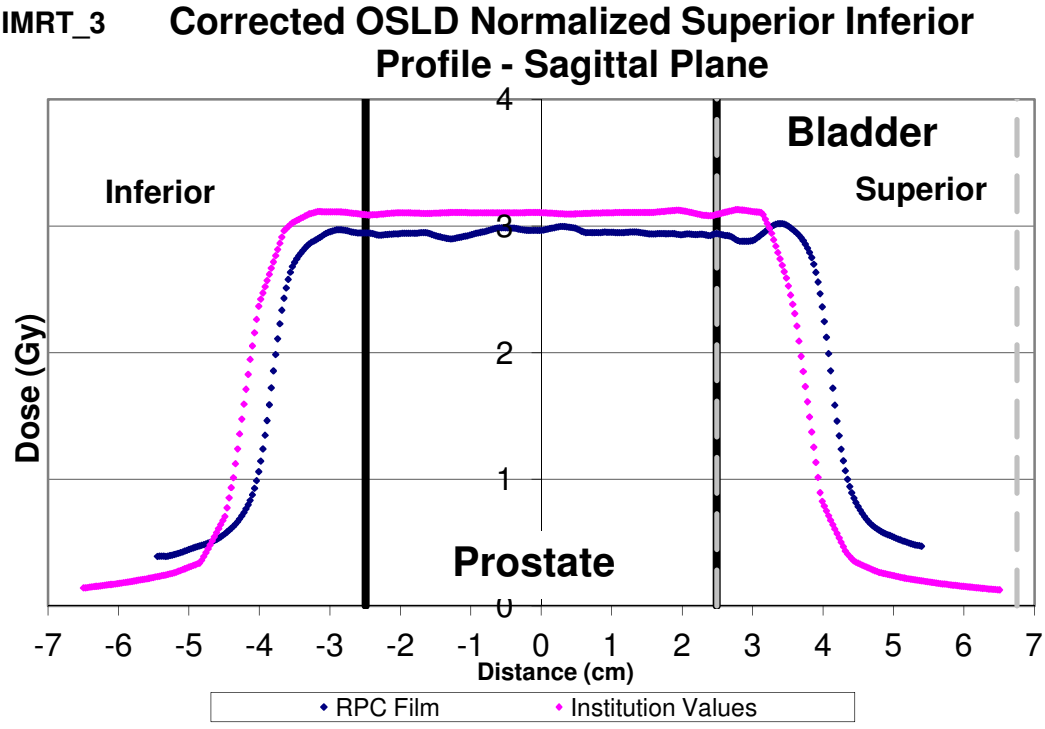

Figure 5.12 Superior-inferior dose profile in sagittal plane from IMRT_3 with film normalized to corrected OSLD dose

5.2.3 CyberKnife Trial

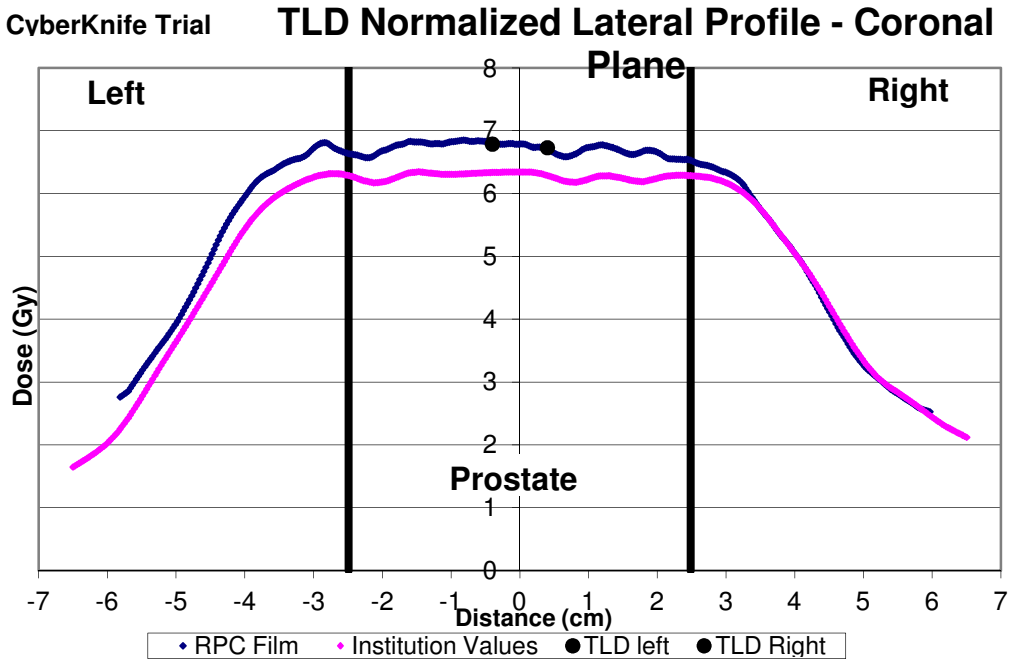

Figure 5.13 Lateral dose profile in coronal plane from CyberKnife trial with film normalized to TLD dose

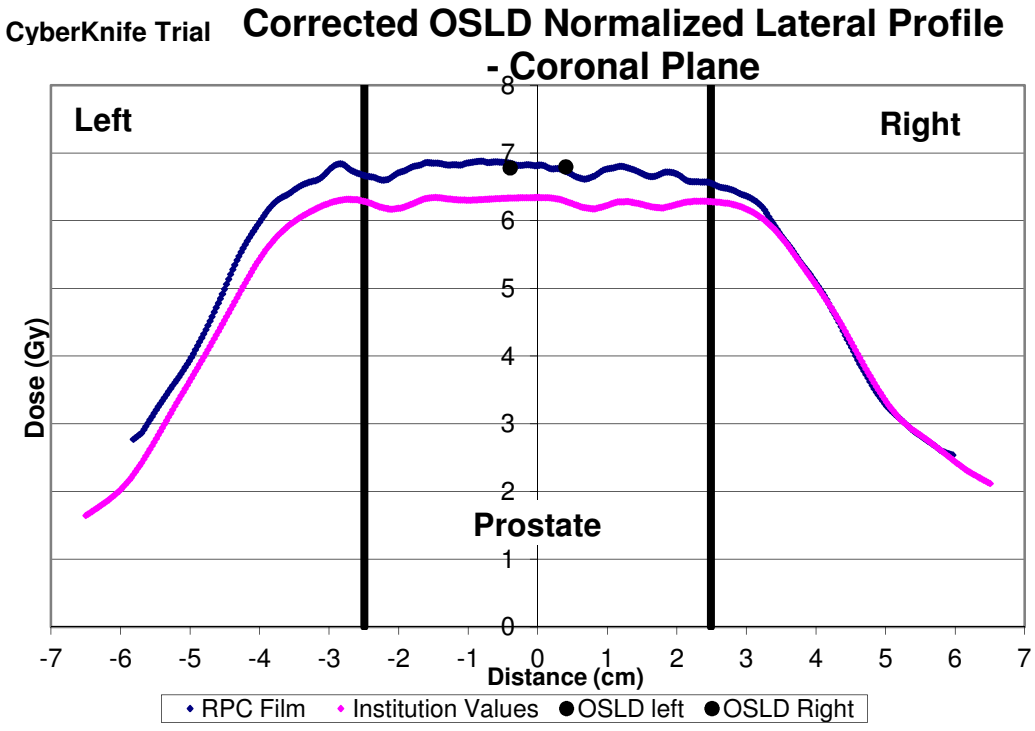

Figure 5.14 Lateral dose profile in coronal plane from CyberKnife trial with film normalized to corrected OSLD dose

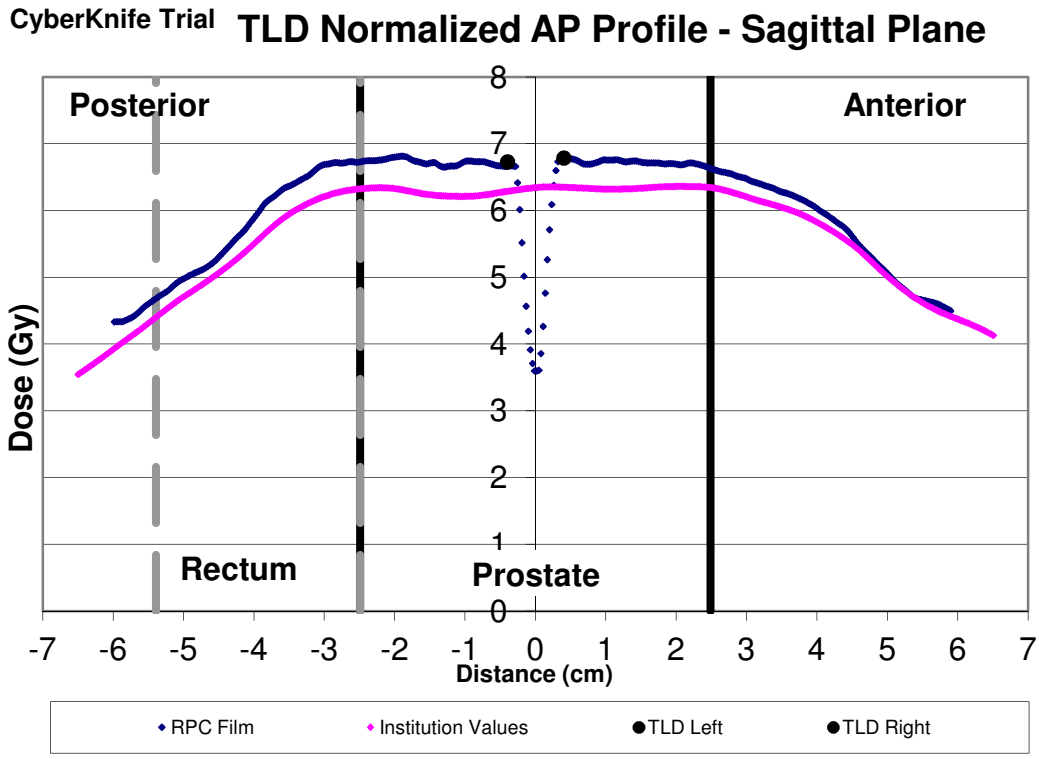

Figure 5.15 AP dose profile in sagittal plane from CyberKnife trial with film normalized to TLD dose

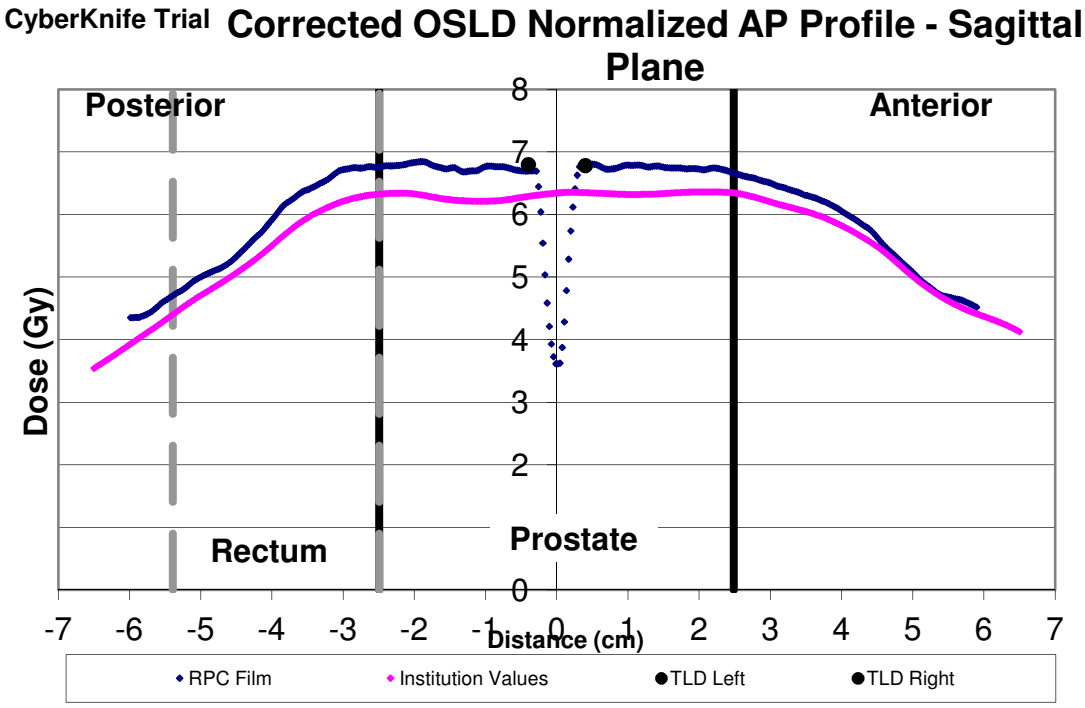

Figure 5.16 AP dose profile in sagittal plane from CyberKnife trial with film normalized to corrected OSLD dose

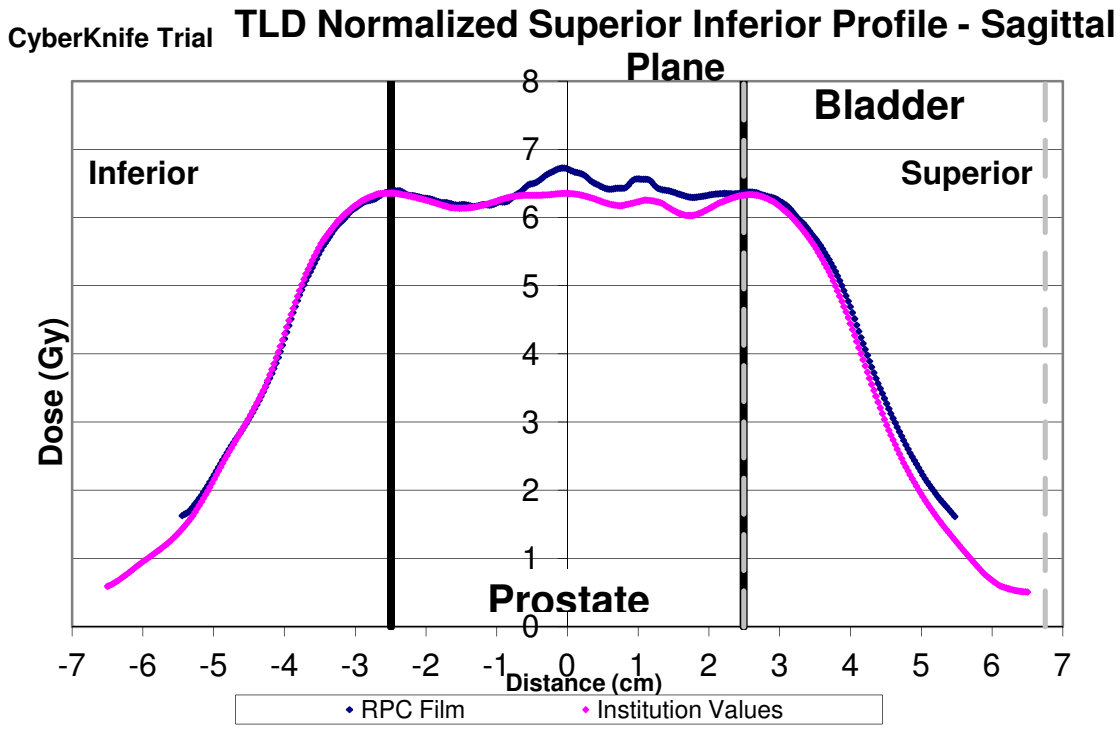

Figure 5.17 Superior-inferior dose profile in sagittal plane from CyberKnife trial with film normalized to TLD dose

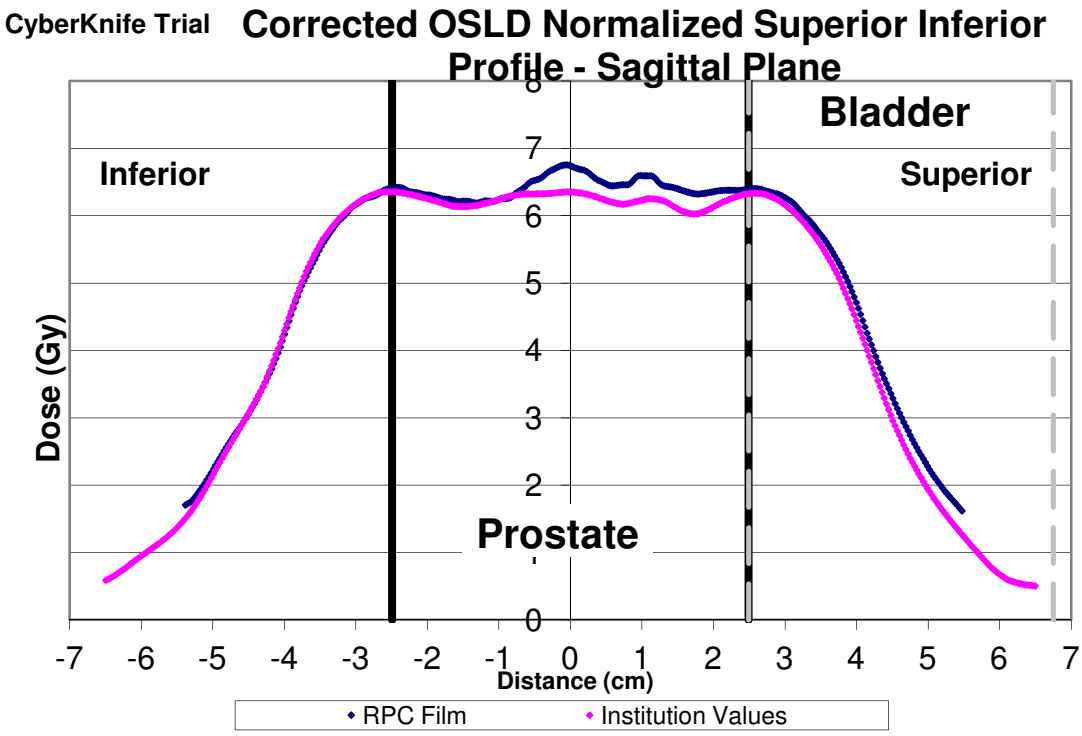

Figure 5.18 Superior-inferior dose profile in sagittal plane from CyberKnife trial with film normalized to corrected OSLD dose

5.2.4 IMRT Trial

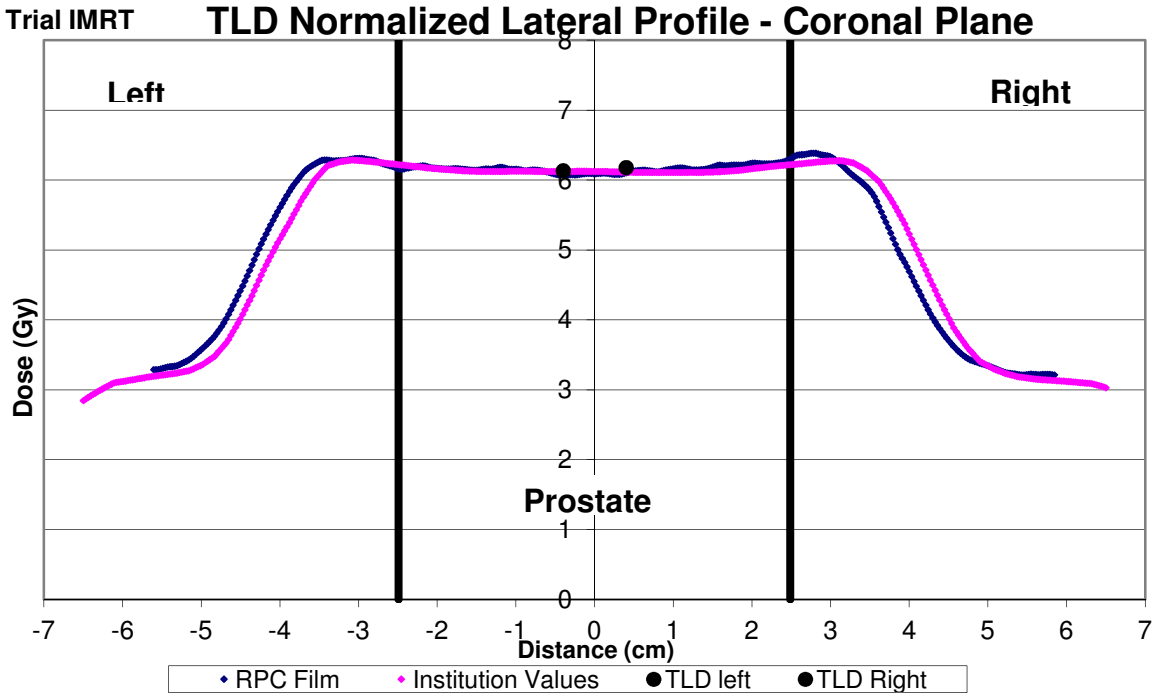

Figure 5.19 Lateral dose profile in coronal plane from IMRT trial with film normalized to TLD dose

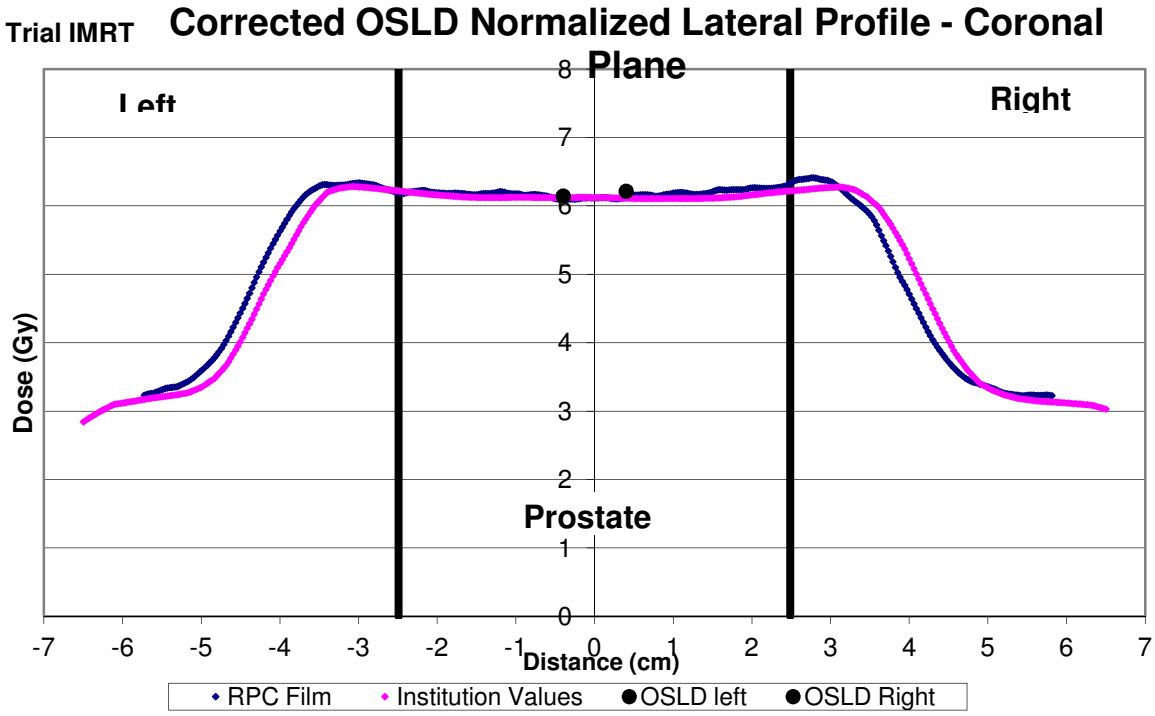

Figure 5.20 Lateral dose profile in coronal plane from IMRT trial with film normalized to corrected OSLD dose

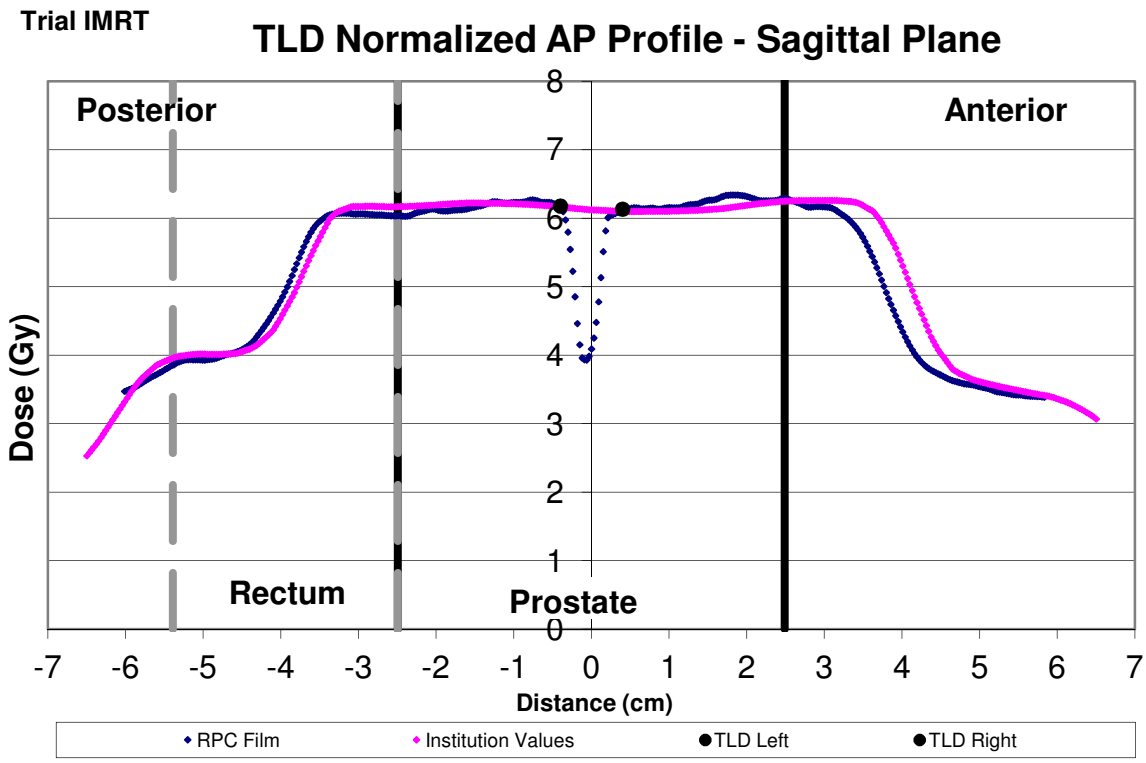

Figure 5.21 AP dose profile in sagittal plane from IMRT trial with film normalized to TLD dose

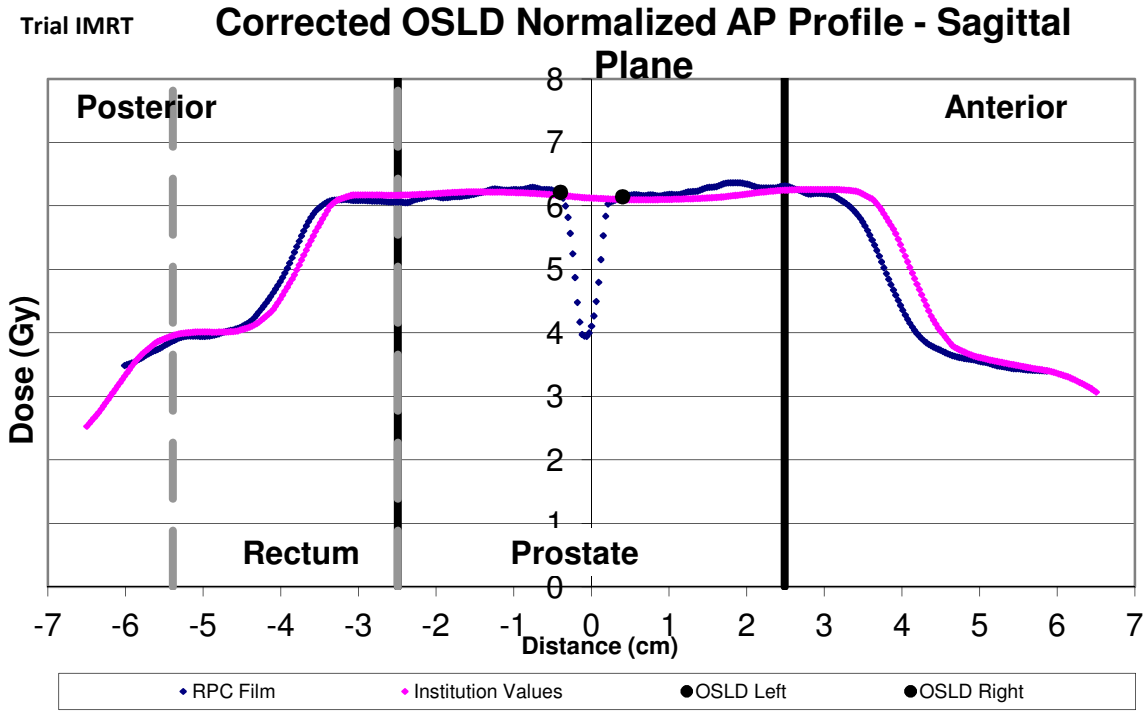

Figure 5.22 AP dose profile in sagittal plane from IMRT trial with film normalized to corrected OSLD dose

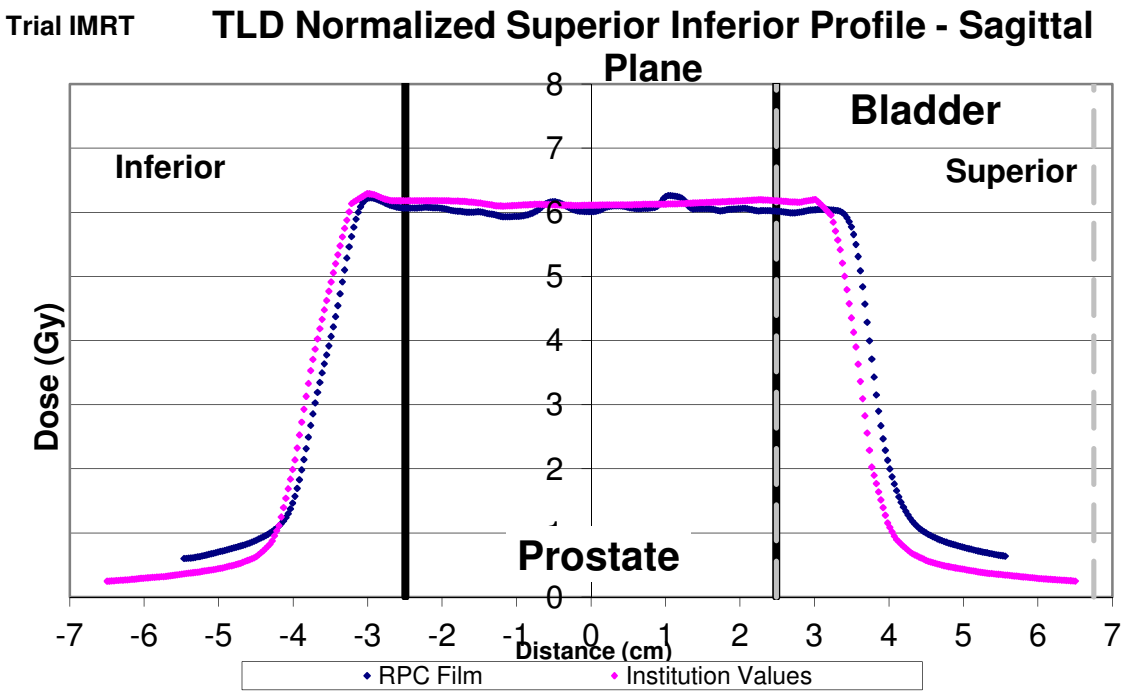

Figure 5.23 Superior-inferior dose profile in sagittal plane from IMRT trial with film normalized to TLD dose

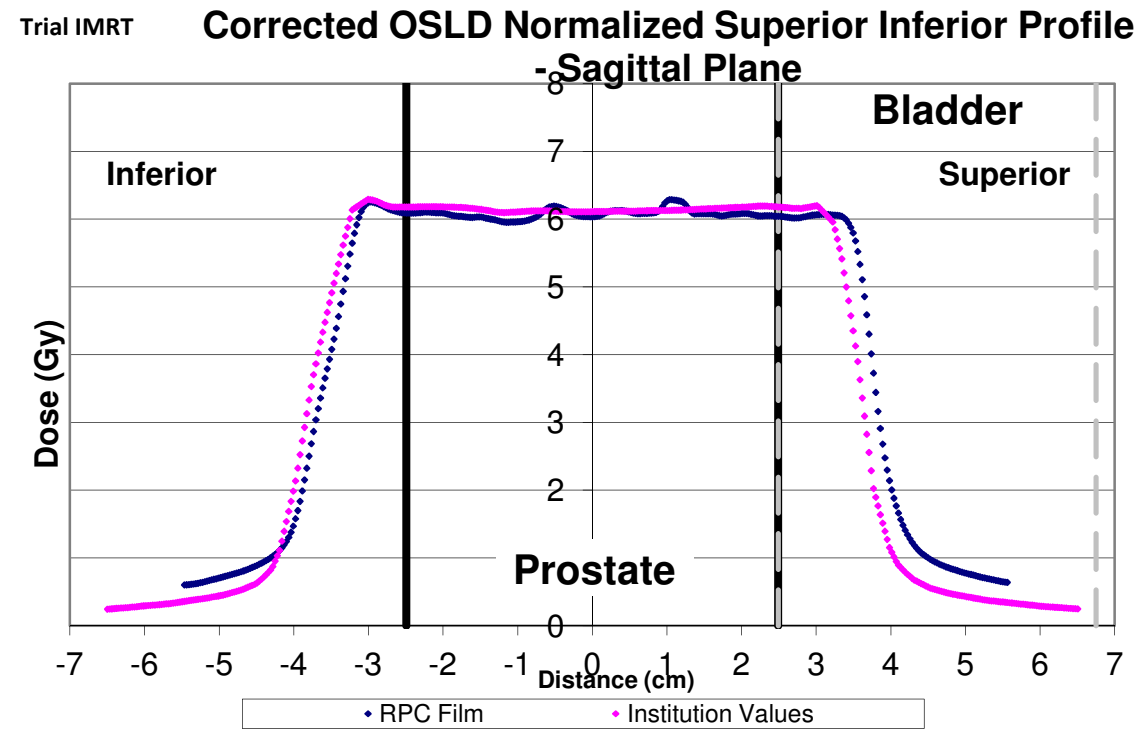

Figure 5.24 Superior-inferior dose profile in sagittal plane from IMRT trial with film normalized to corrected OSLD dose

5.3 Gamma Analysis

5.3.1 IMRT_1 Coronal Films

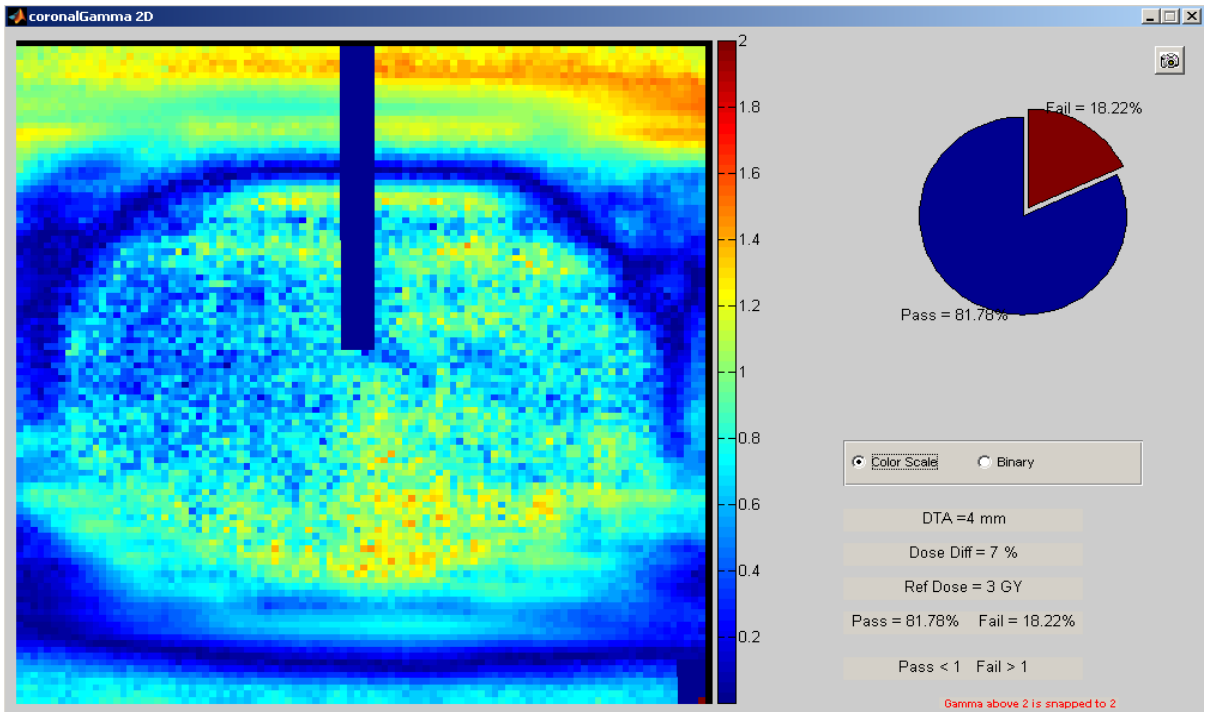

Figure 5.25 IMRT_1 color scale gamma results for coronal film normalized to TLD dose

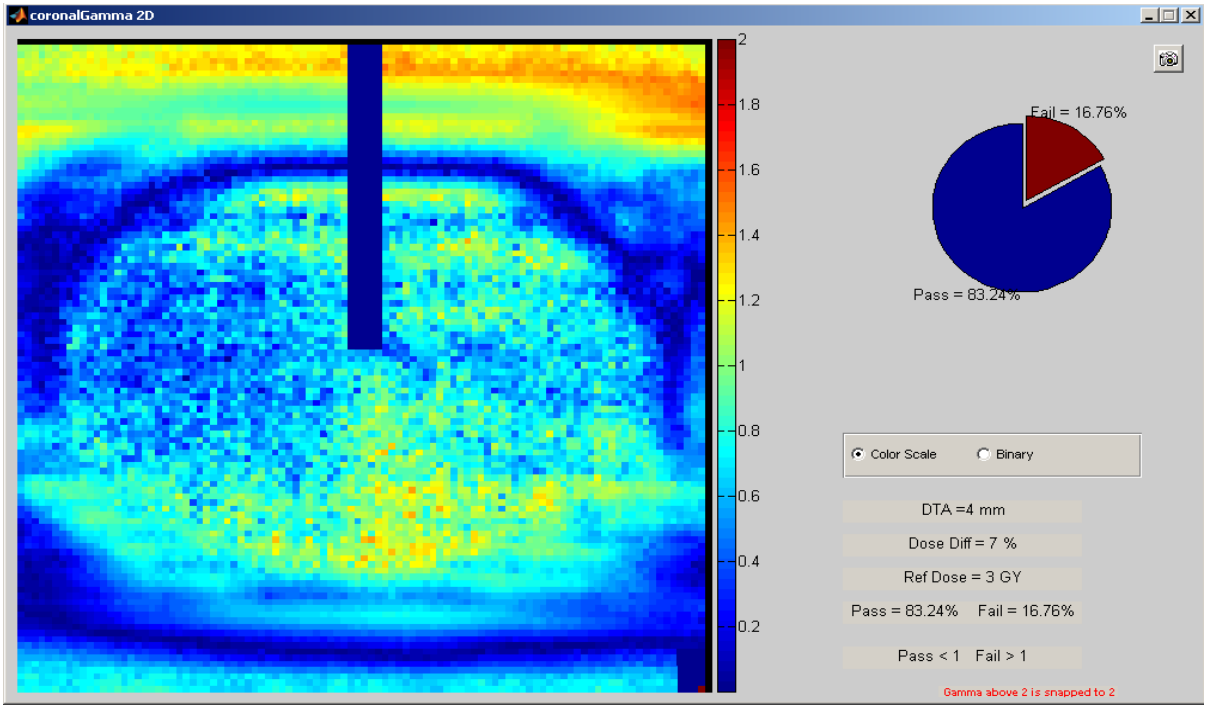

Figure 5.26 IMRT_1 color scale gamma results for coronal film normalized to corrected OSLD dose

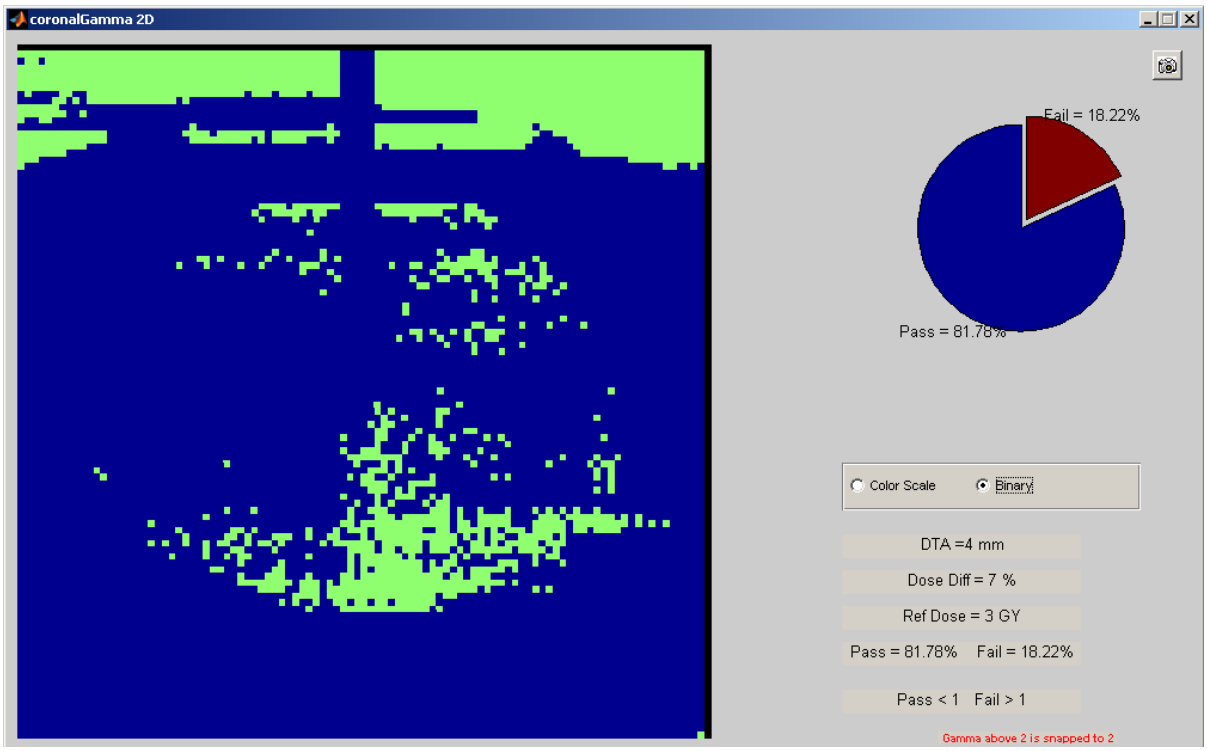

Figure 5.27 IMRT_1 binary gamma results for coronal film normalized to TLD dose

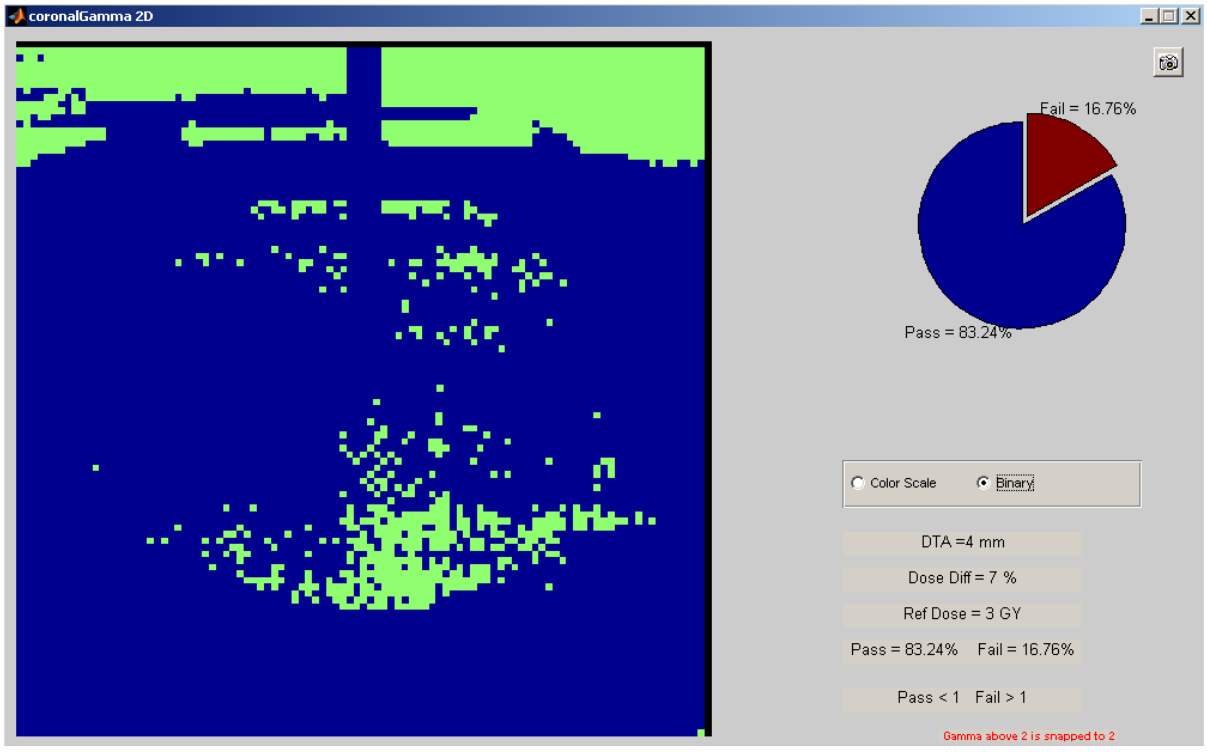

Figure 5.28 IMRT_1 binary gamma results for coronal film normalized to corrected OSLD dose

5.3.2 IMRT_1 Sagittal Films

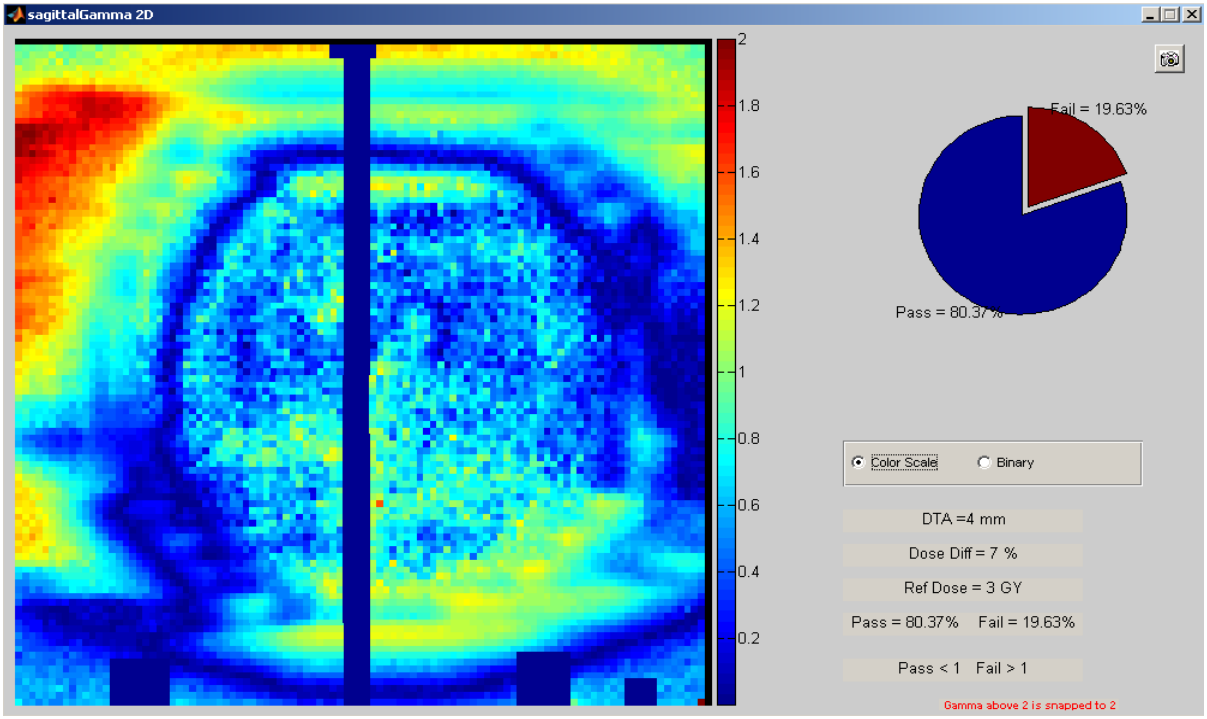

Figure 5.29 IMRT_1 color scale gamma results for sagittal film normalized to TLD dose

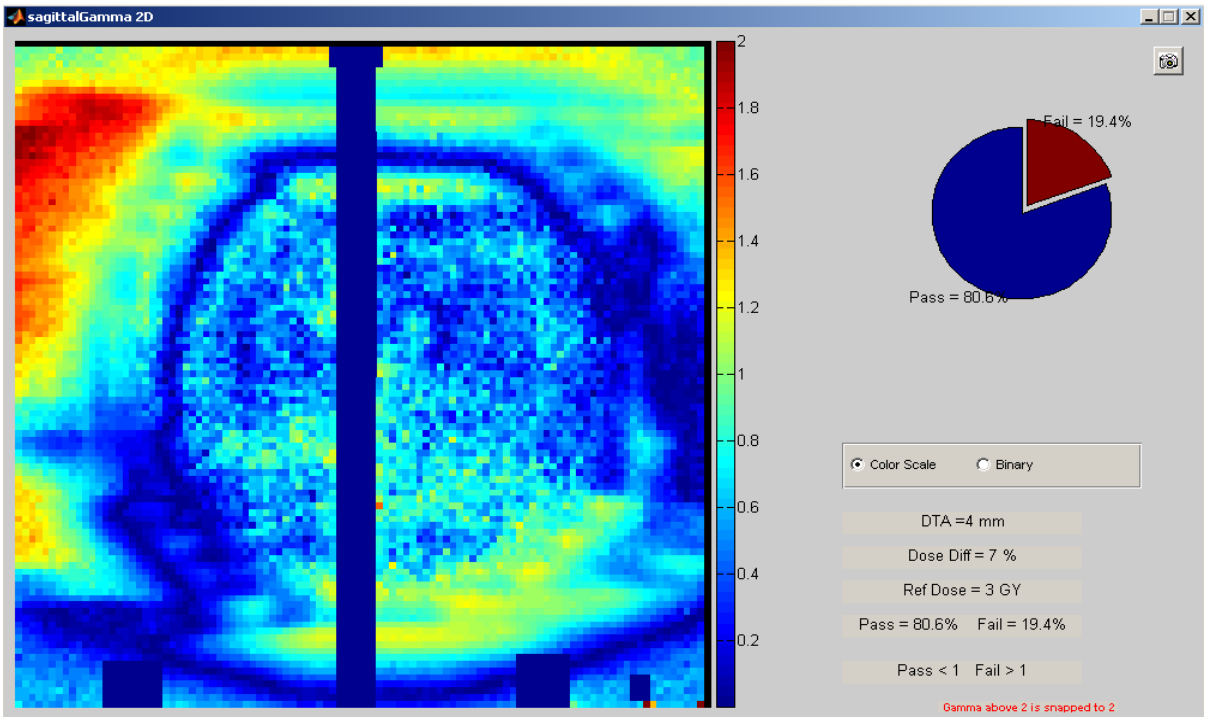

Figure 5.30 IMRT_1 color scale gamma results for sagittal film normalized to corrected OSLD dose

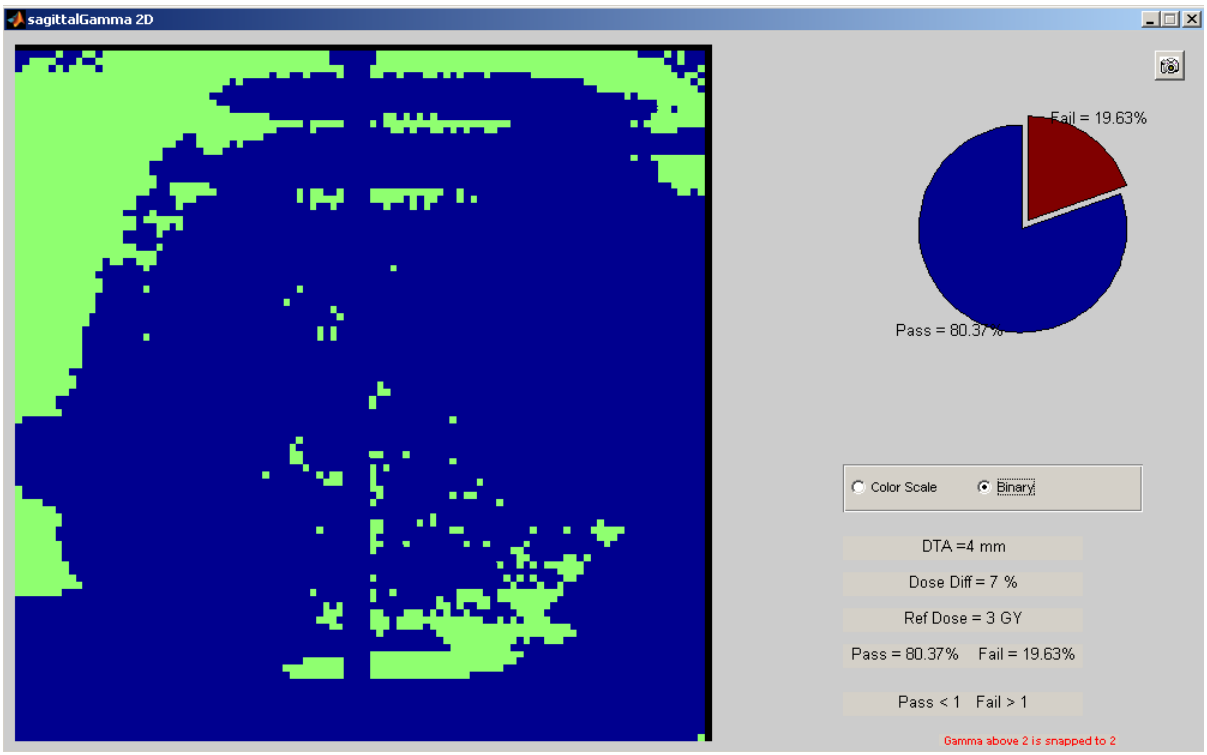

Figure 5.31 IMRT_1 binary gamma results for sagittal film normalized to TLD dose

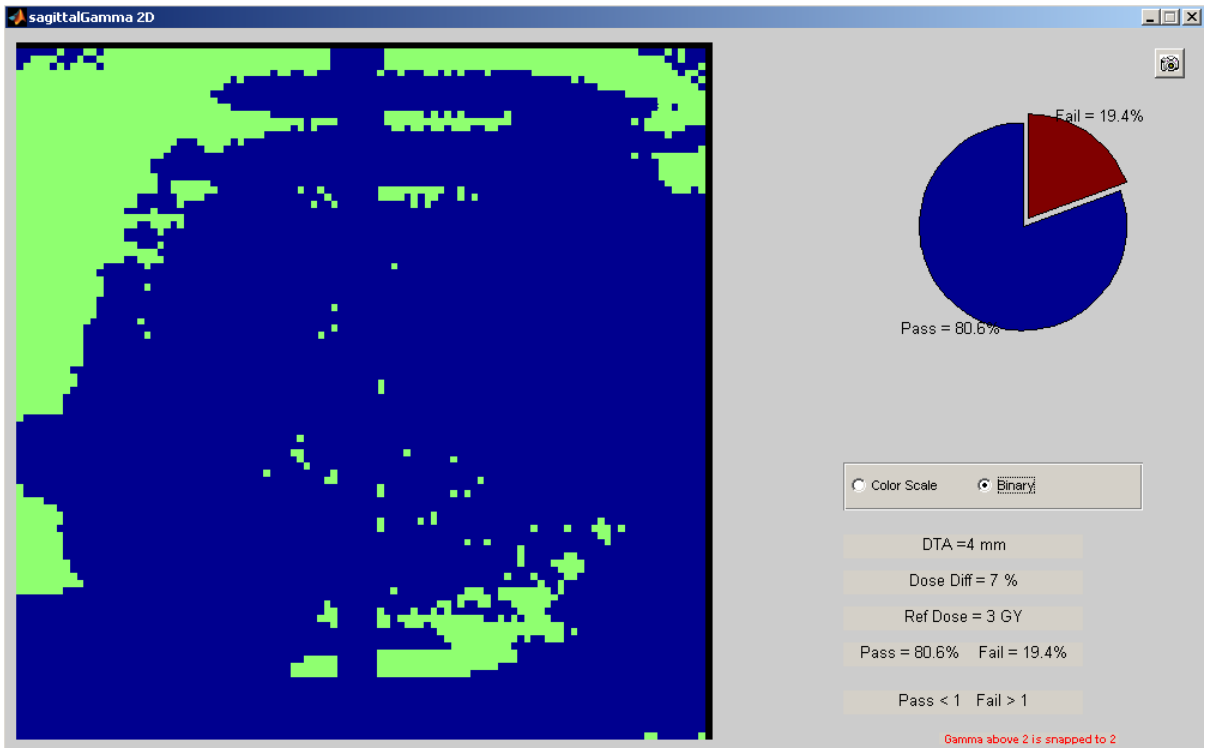

Figure 5.32 IMRT_1 binary gamma results for sagittal film normalized to corrected OSLD dose

5.3.3 IMRT_3 Coronal Films

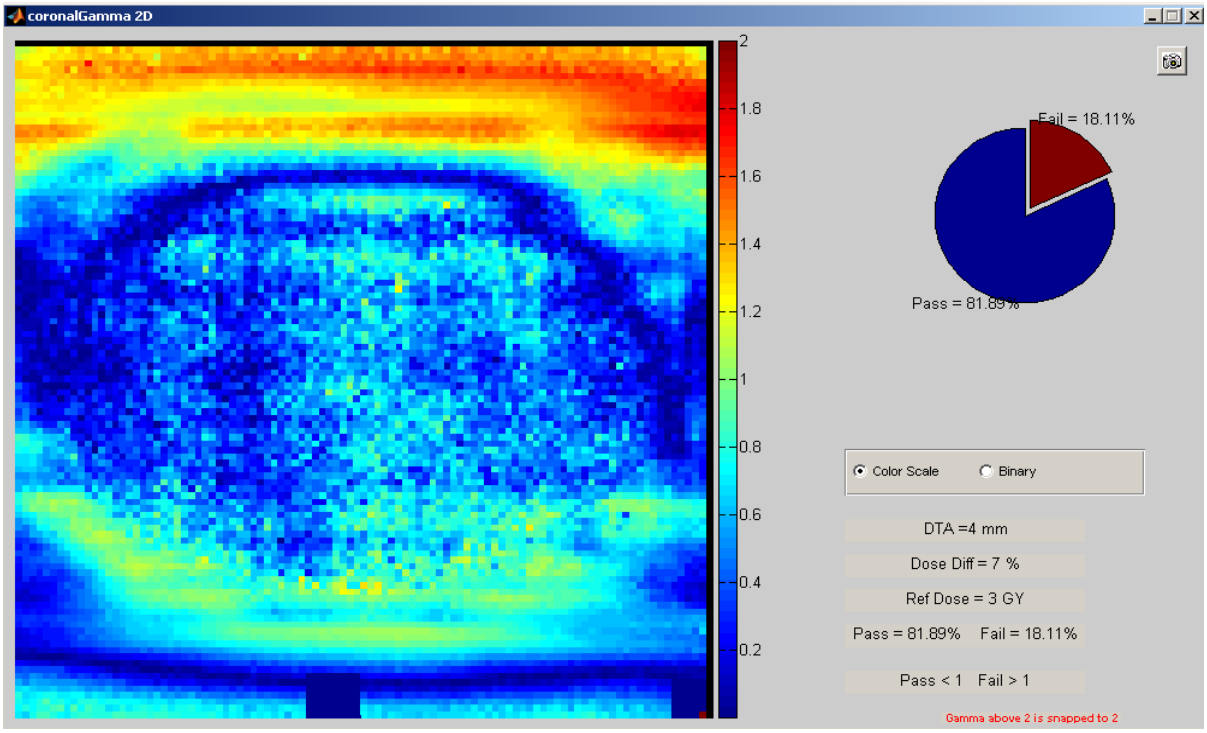

Figure 5.33 IMRT_3 color scale gamma results for coronal film normalized to TLD dose

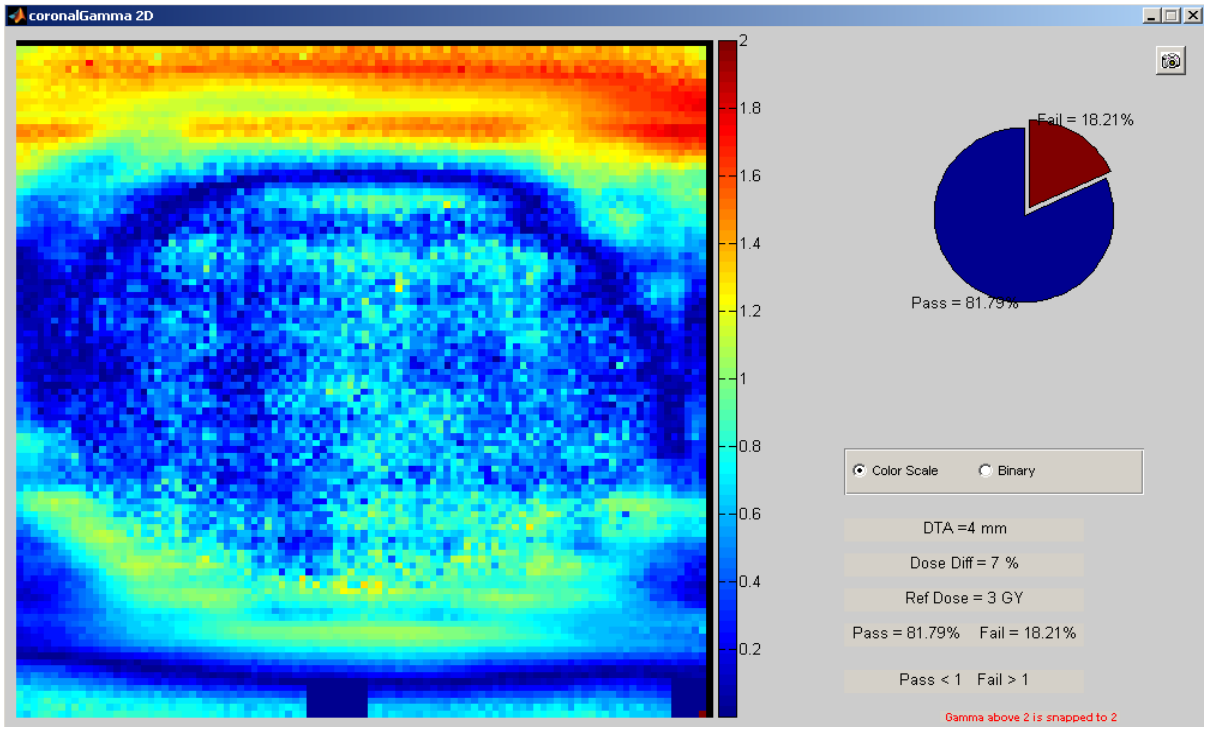

Figure 5.34 IMRT_3 color scale gamma results for coronal film normalized to corrected OSLD dose

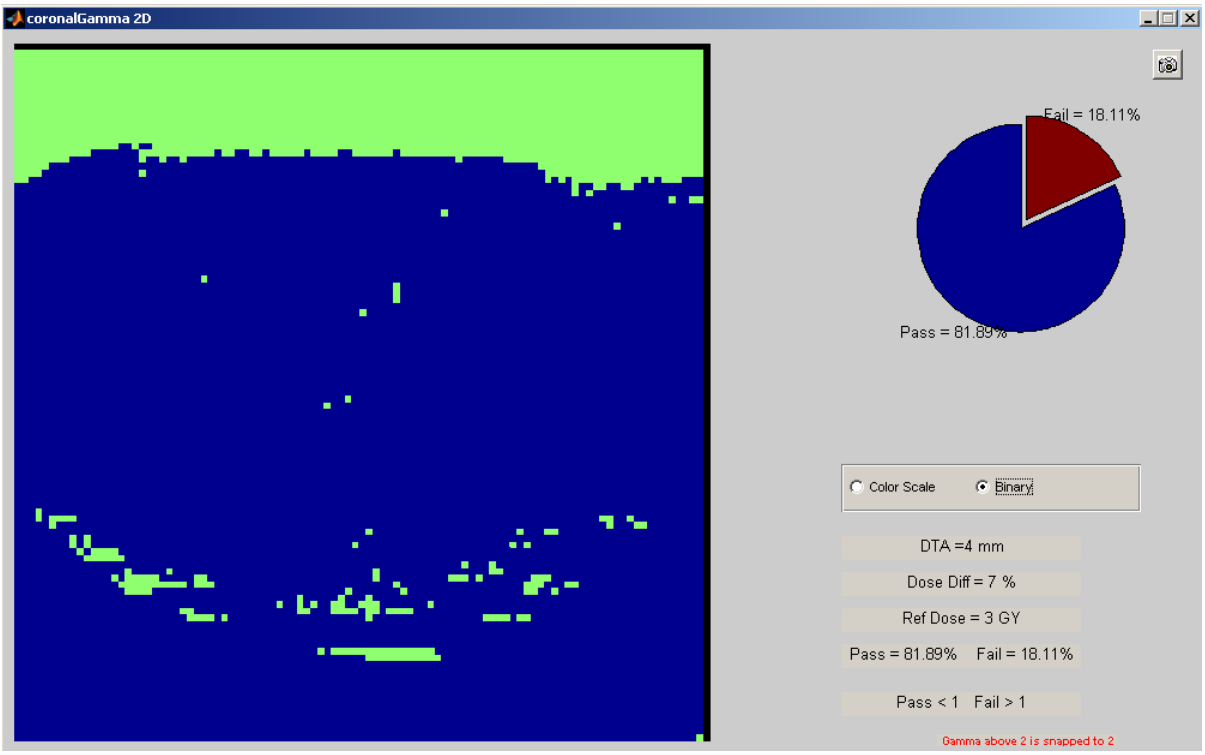

Figure 5.35 IMRT_3 binary gamma results for coronal film normalized to TLD dose

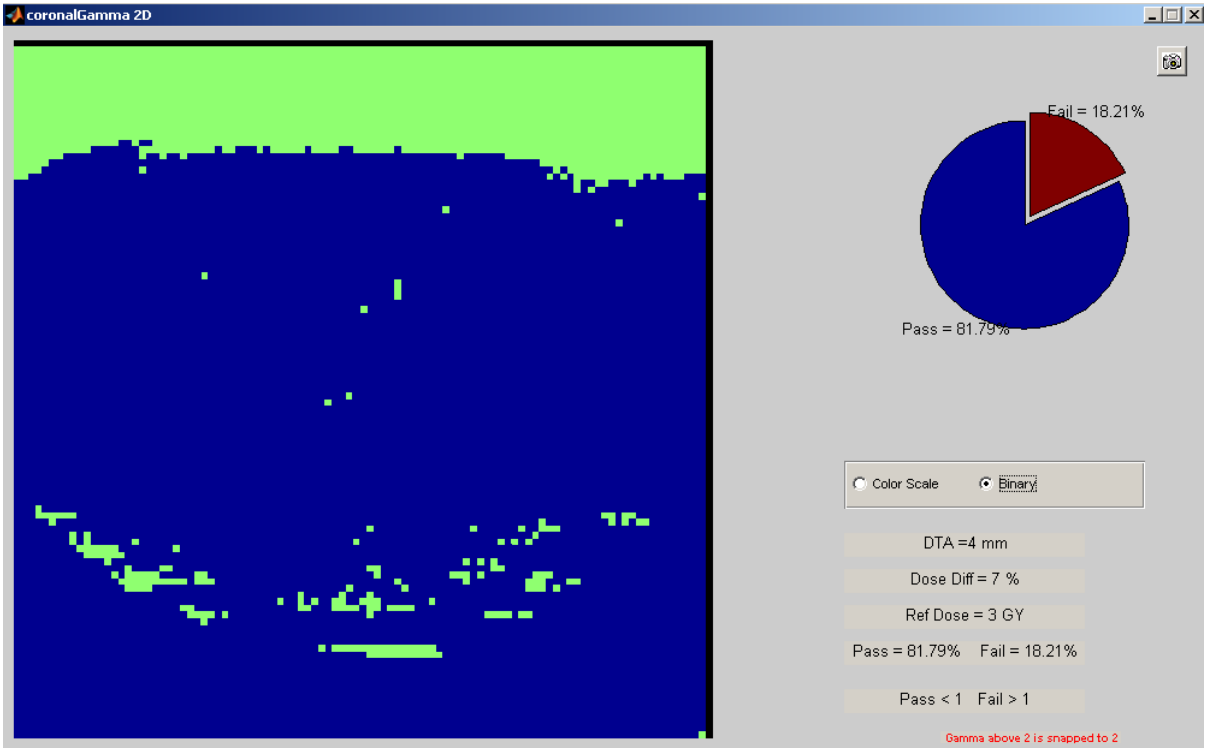

Figure 5.36 IMRT_3 binary gamma results for coronal film normalized to corrected OSLD dose

5.3.4 IMRT_3 Sagittal Films

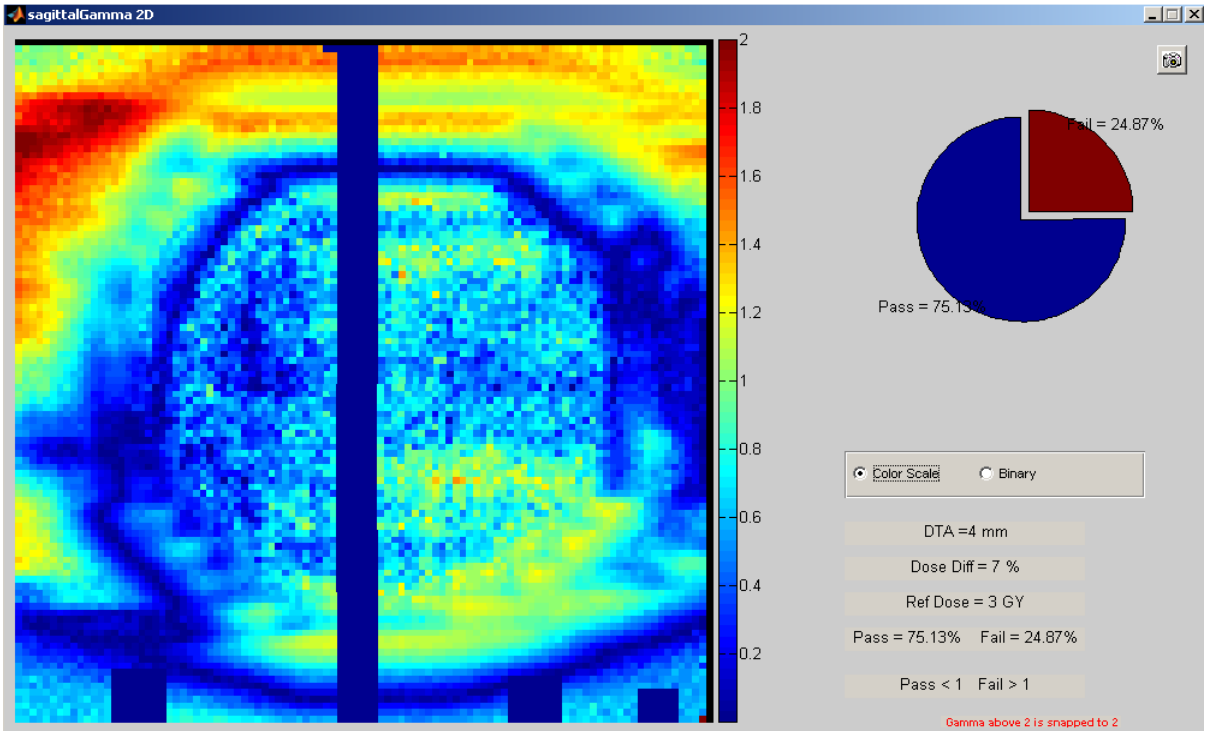

Figure 5.37 IMRT_3 color scale gamma results for sagittal film normalized to TLD dose

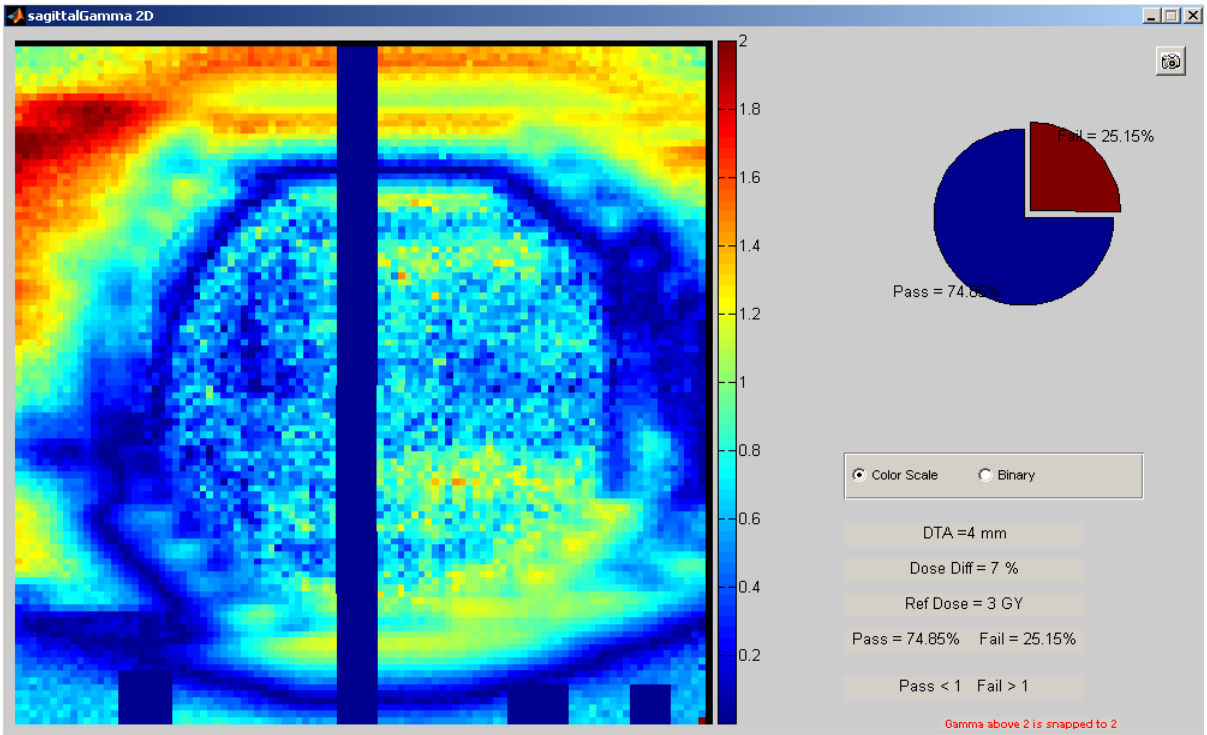

Figure 5.38 IMRT_3 color scale gamma results for sagittal film normalized to corrected OSLD dose

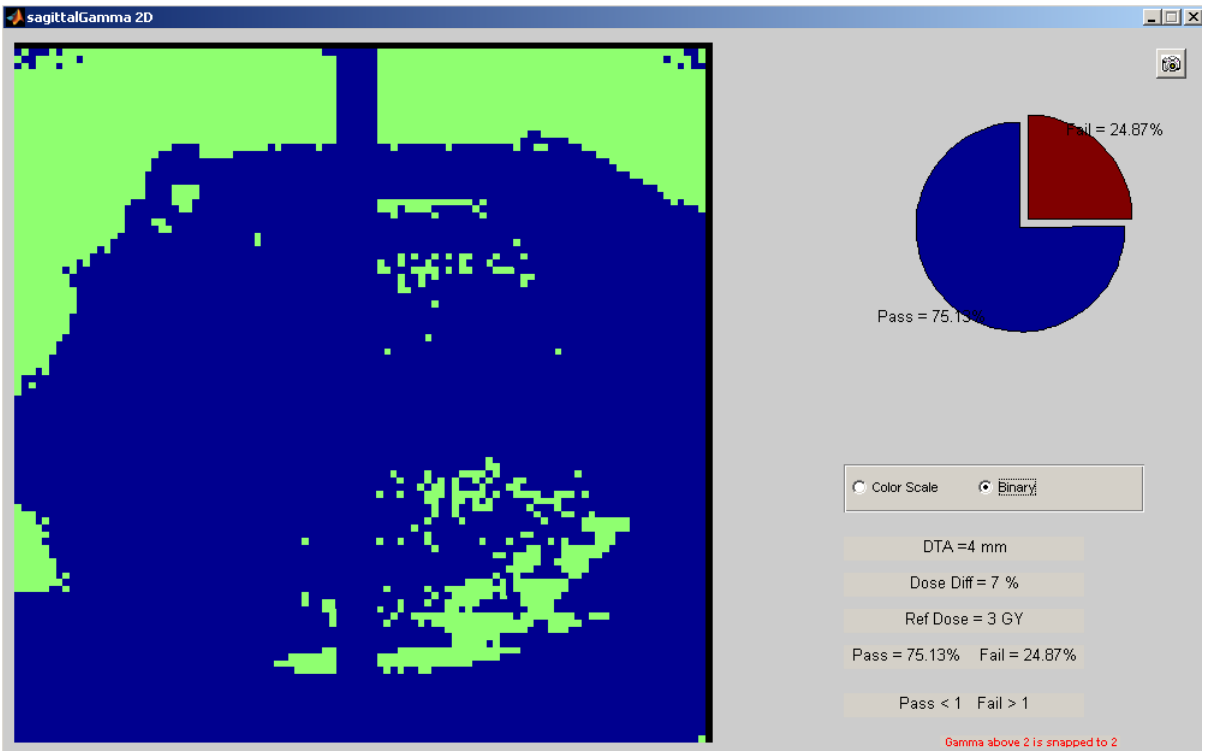

Figure 5.39 IMRT_3 binary gamma results for sagittal film normalized to TLD dose

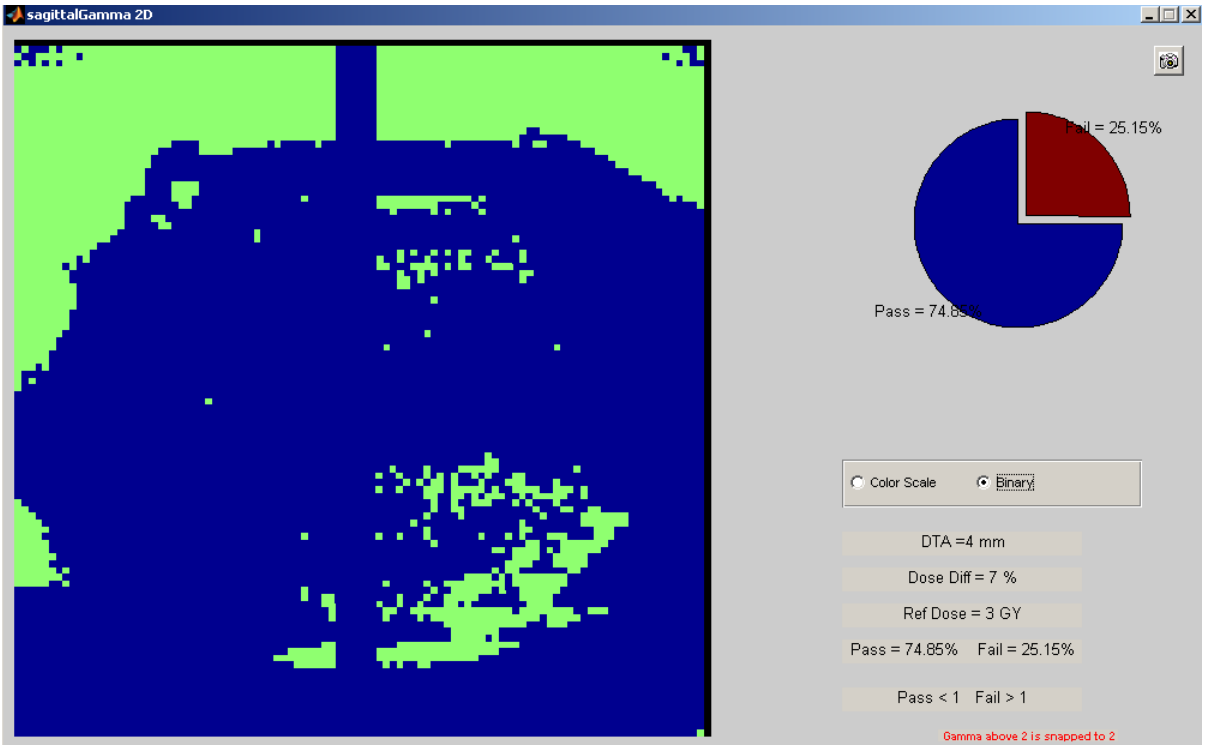

Figure 5.40 IMRT_3 binary gamma results for sagittal film normalized to corrected OSLD dose

5.3.5 CyberKnife Trial Coronal Films

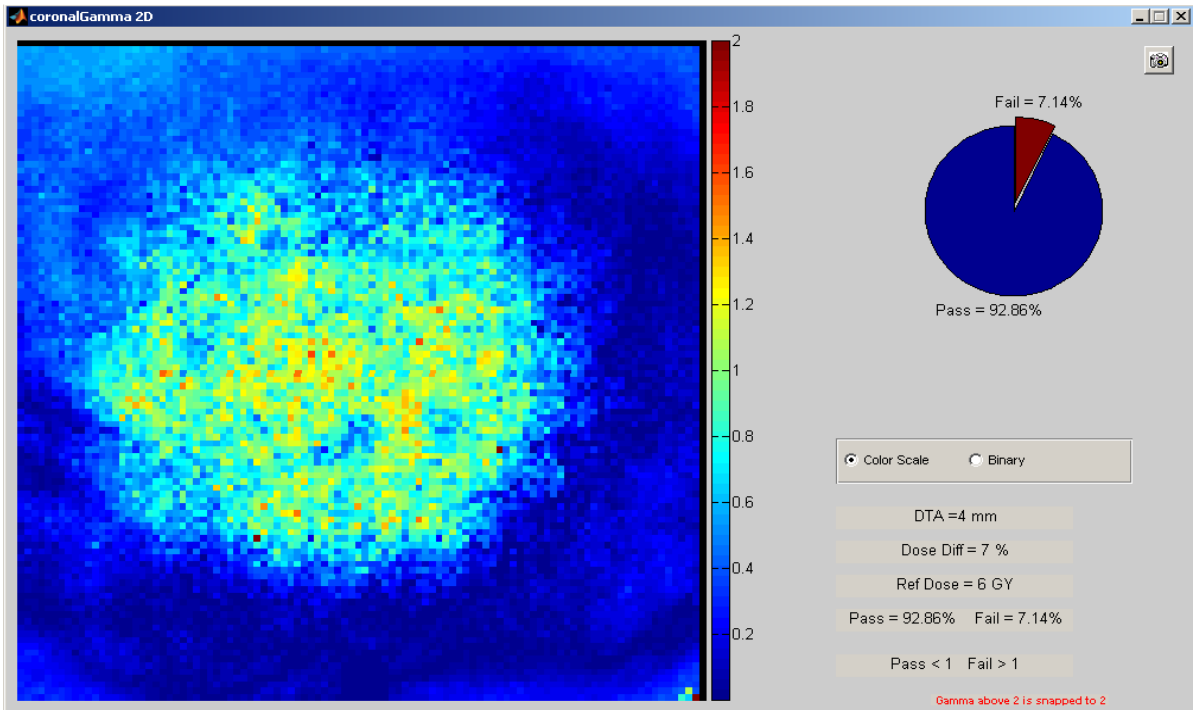

Figure 5.41 CyberKnife trial color scale gamma results for coronal film normalized to TLD dose

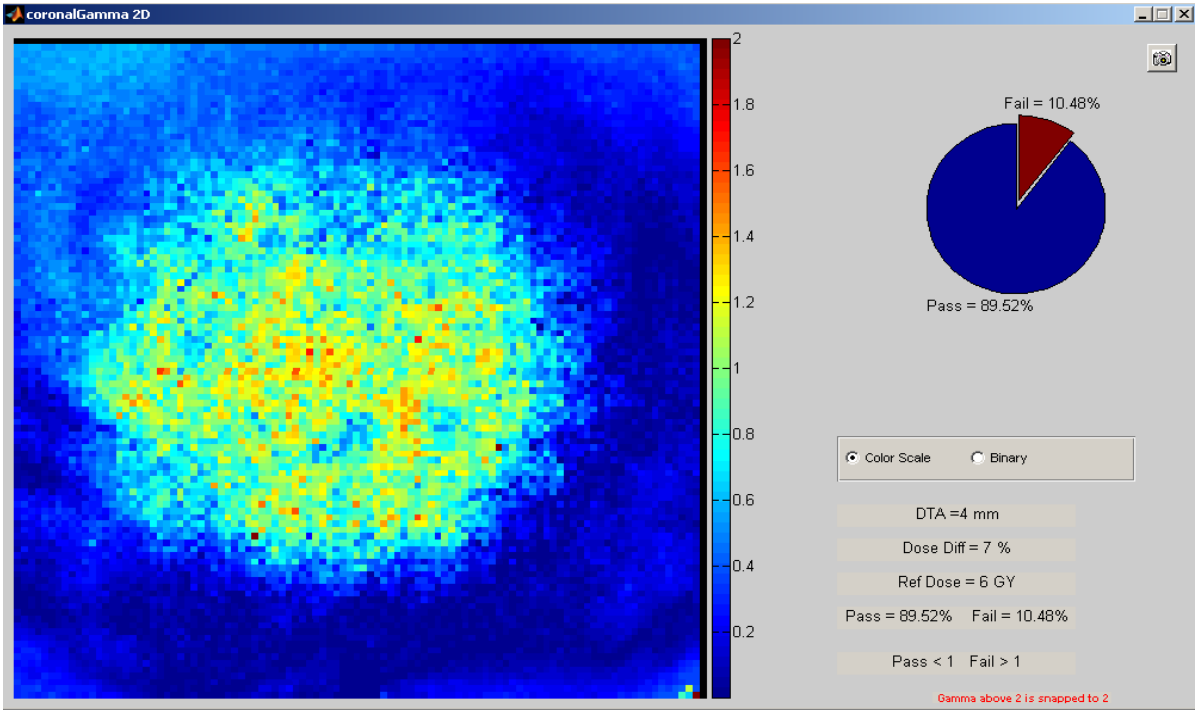

Figure 5.42 CyberKnife trial color scale gamma results for coronal film normalized to corrected OSLD dose

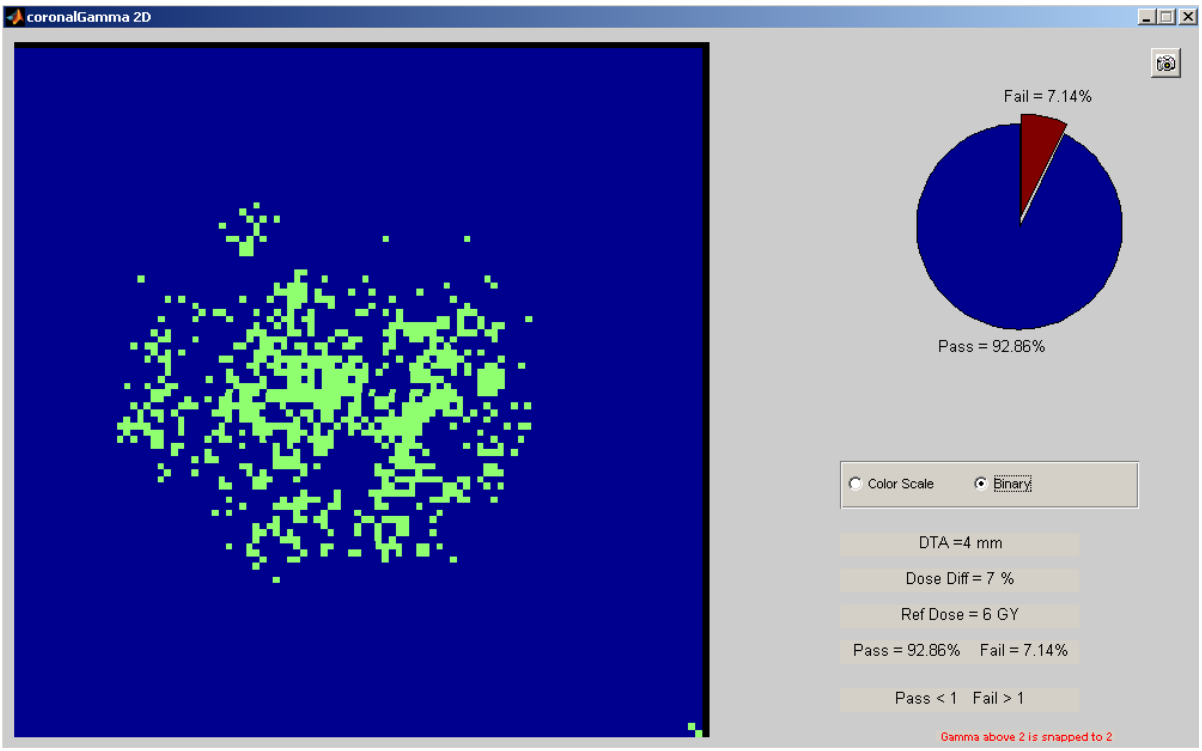

Figure 5.43 CyberKnife trial binary gamma results for coronal film normalized to TLD dose

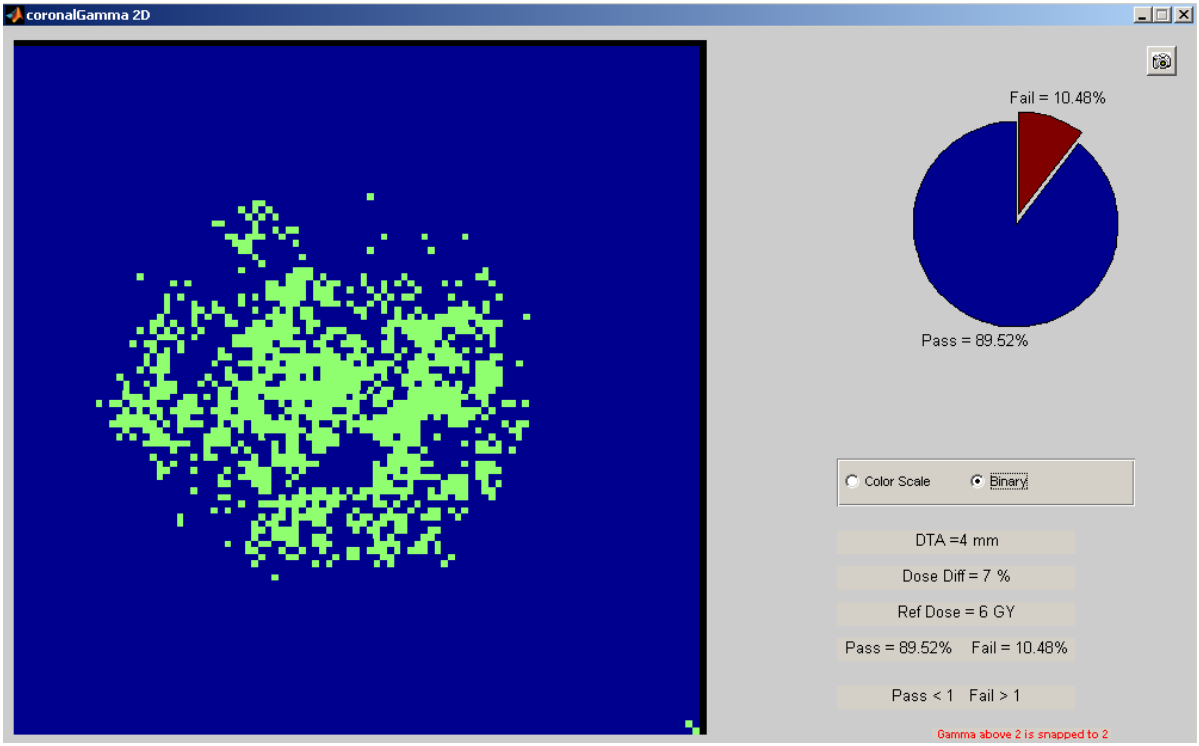

Figure 5.44 CyberKnife trial binary gamma results for coronal film normalized to corrected OSLD dose

5.3.6 CyberKnife Trial Sagittal Films

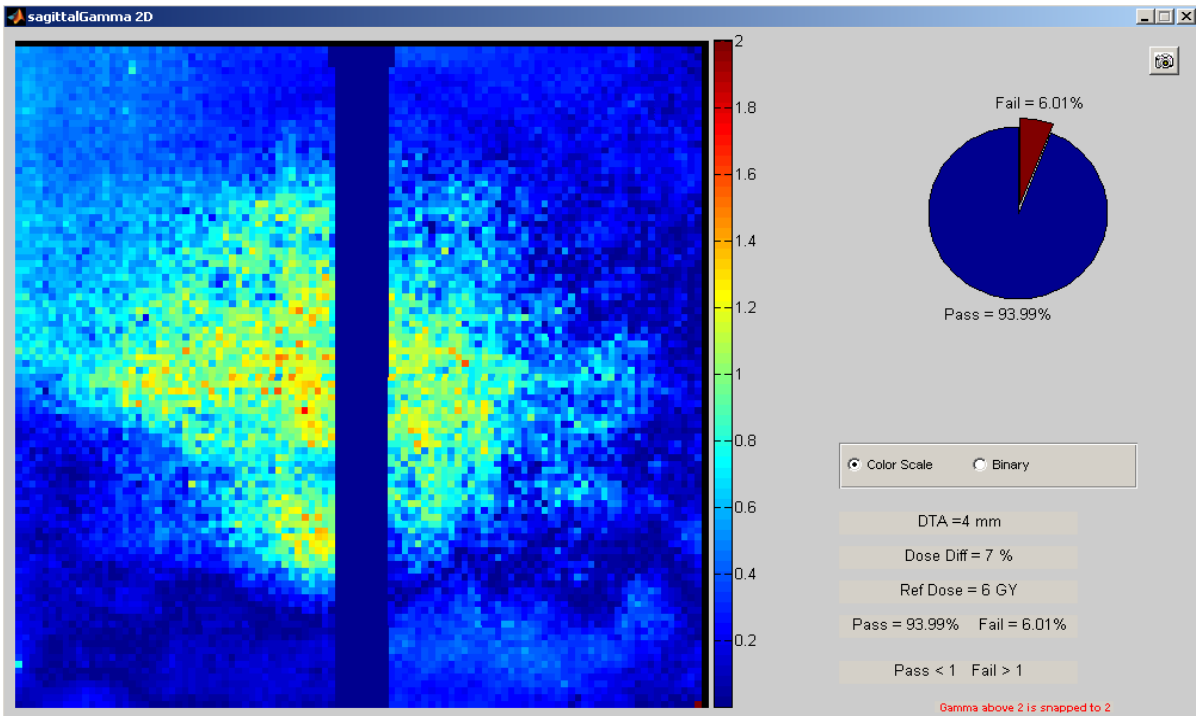

Figure 5.45 CyberKnife trial color scale gamma results for sagittal film normalized to TLD dose

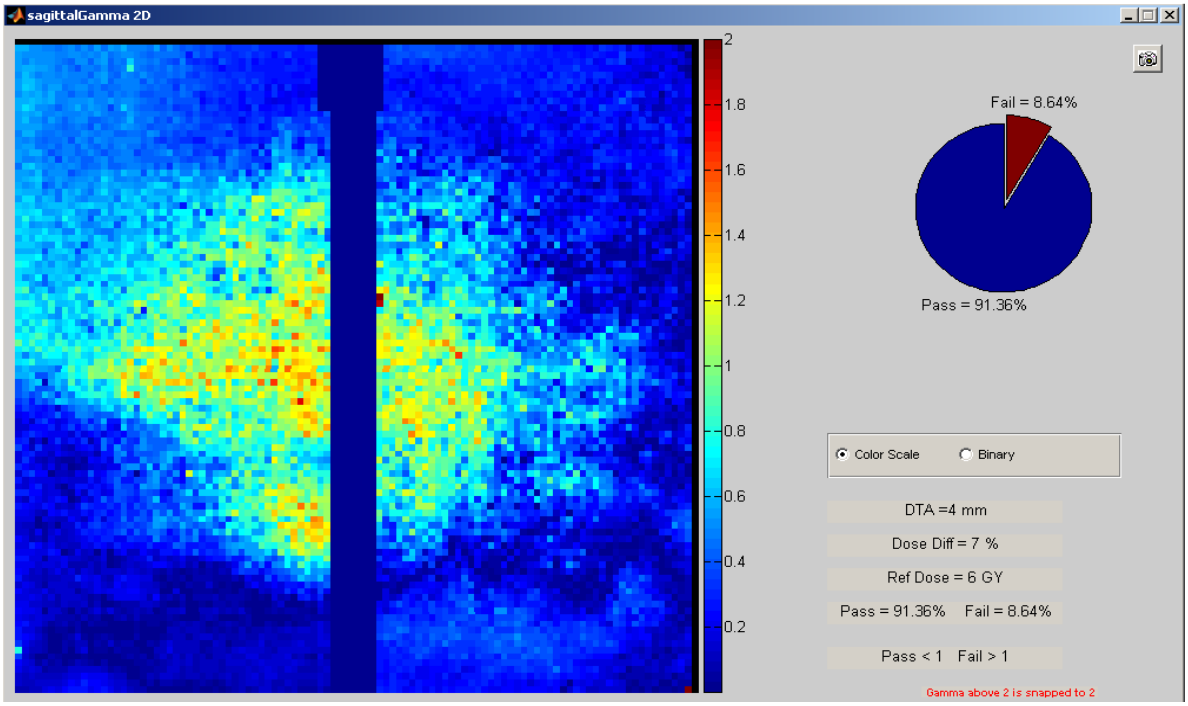

Figure 5.46 CyberKnife trial color scale gamma results for sagittal film normalized to corrected OSLD dose

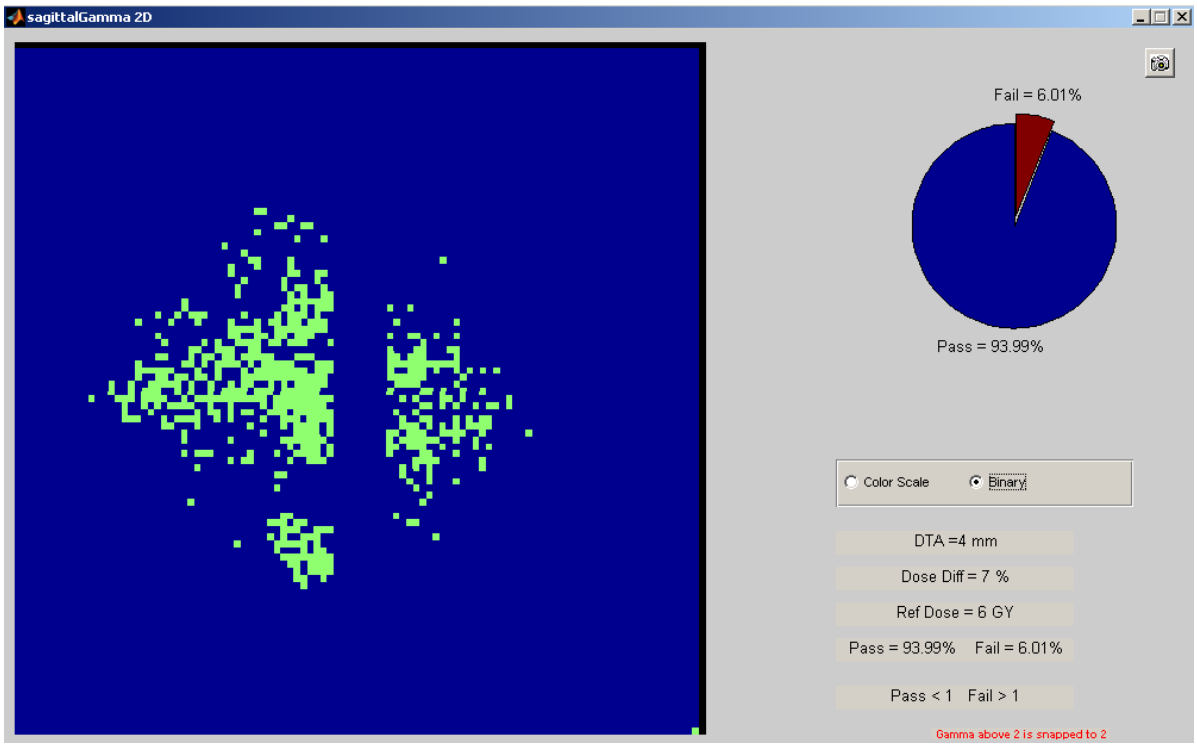

Figure 5.47 CyberKnife trial binary gamma results for sagittal film normalized to TLD dose

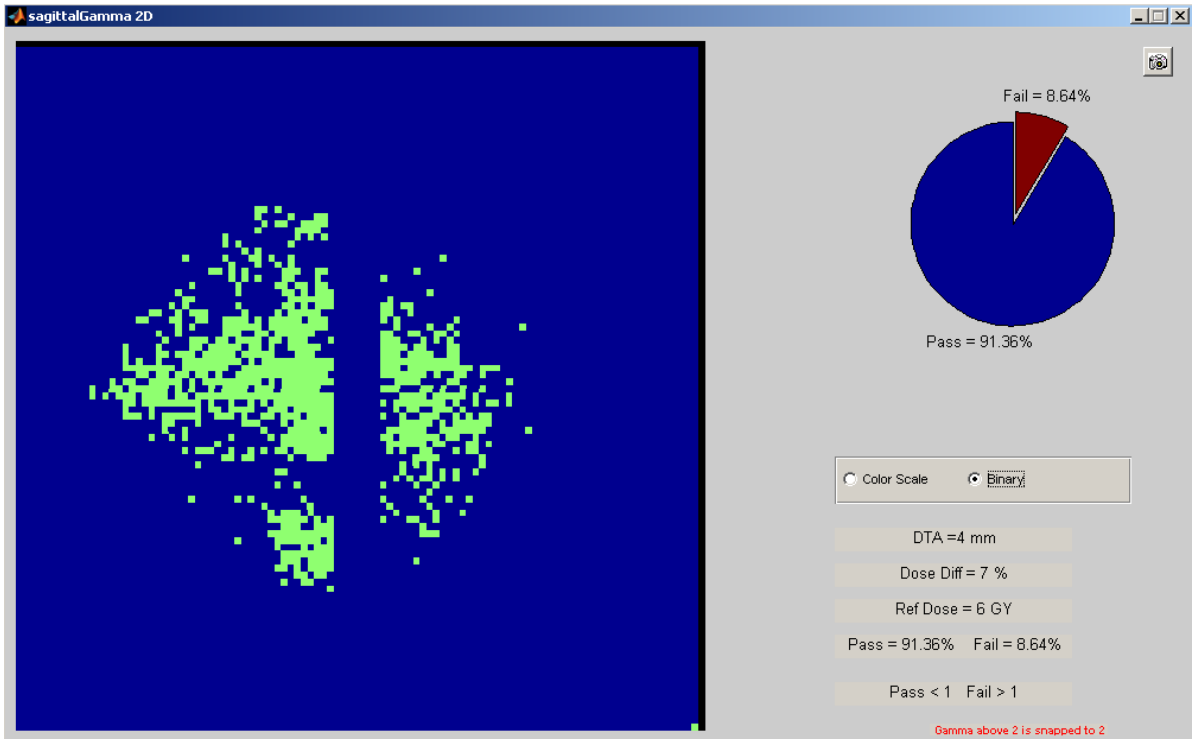

Figure 5.48 CyberKnife trial binary gamma results for sagittal film normalized to corrected OSLD dose

5.3.7 IMRT Trial Coronal Films

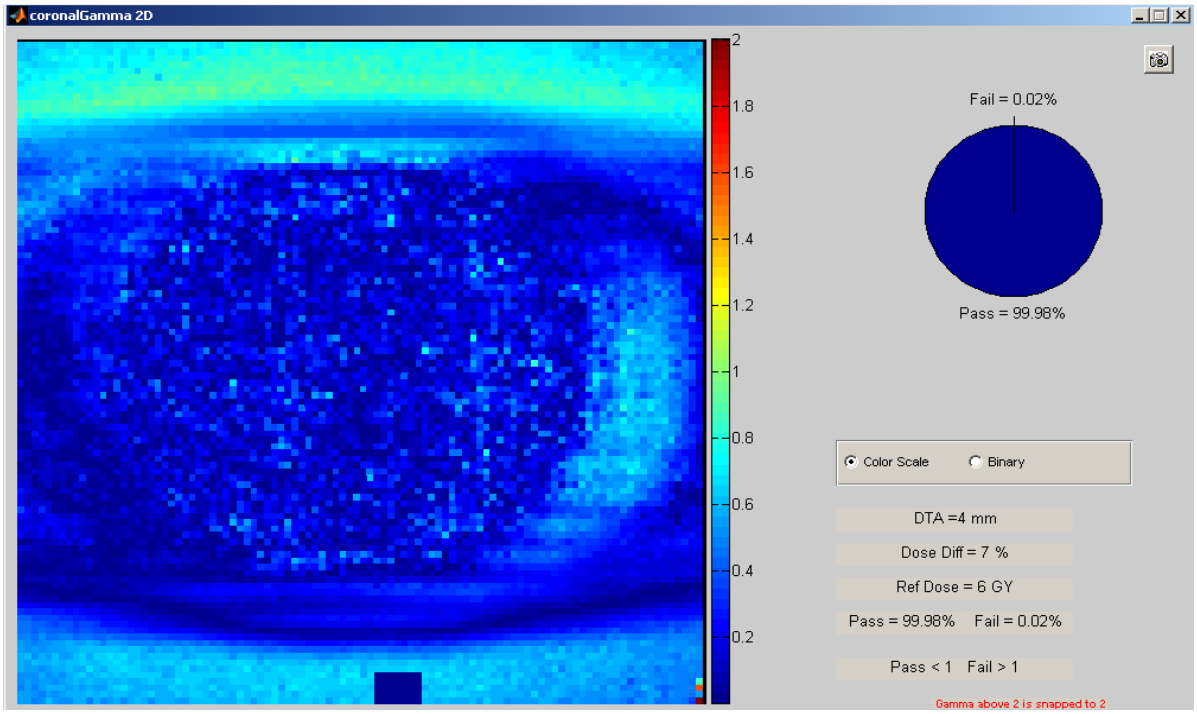

Figure 5.49 IMRT trial color scale gamma results for coronal film normalized to TLD dose

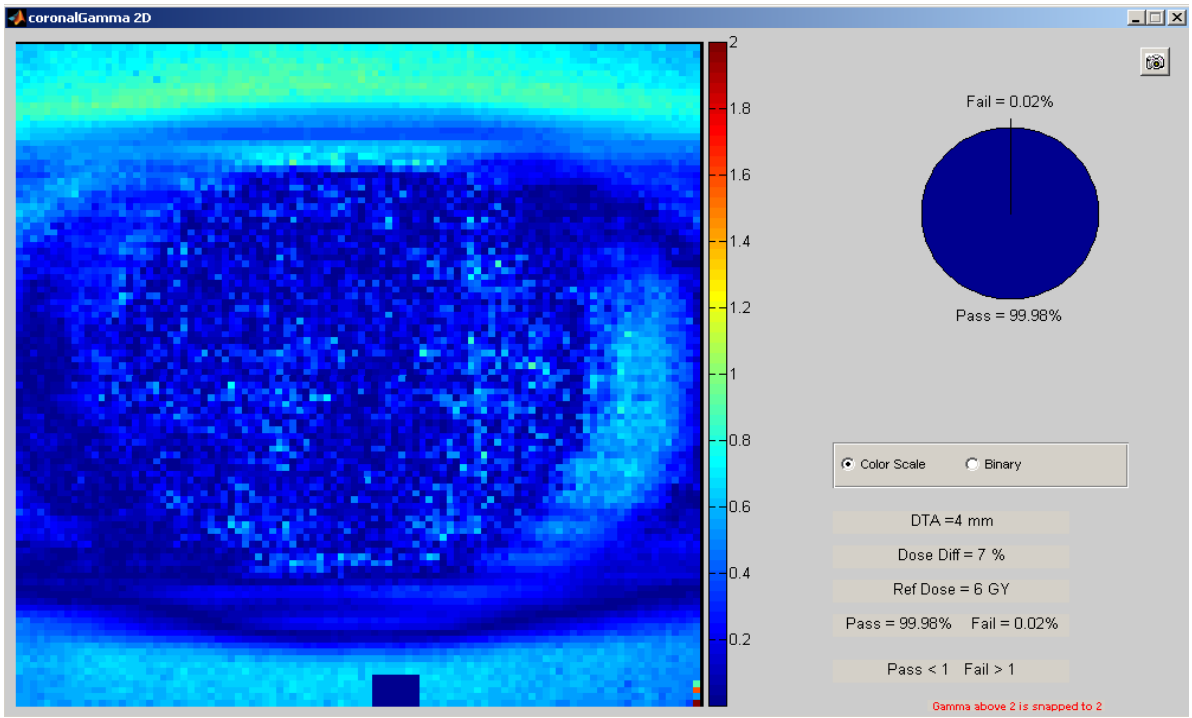

Figure 5.50 IMRT trial color scale gamma results for coronal film normalized to corrected OSLD dose

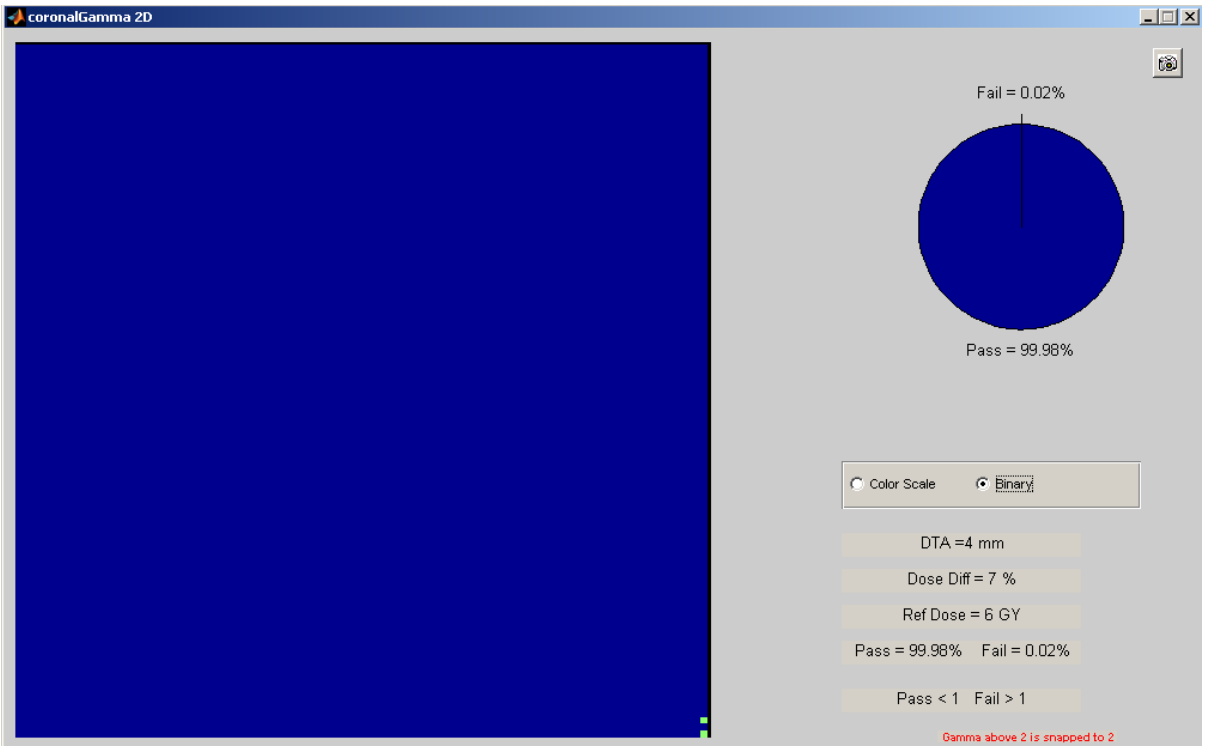

Figure 5.51 IMRT trial binary gamma results for coronal film normalized to TLD dose

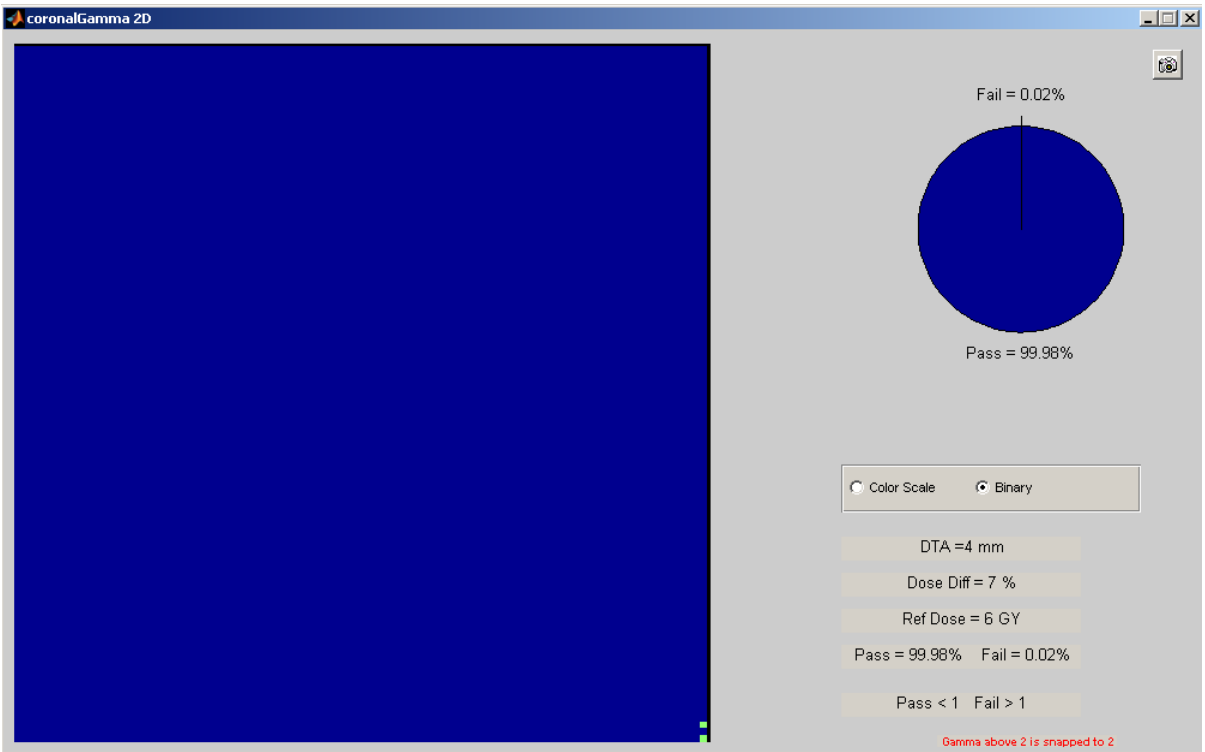

Figure 5.52 IMRT trial binary gamma results for coronal film normalized to corrected OSLD dose

5.3.8 IMRT Trial Sagittal Films

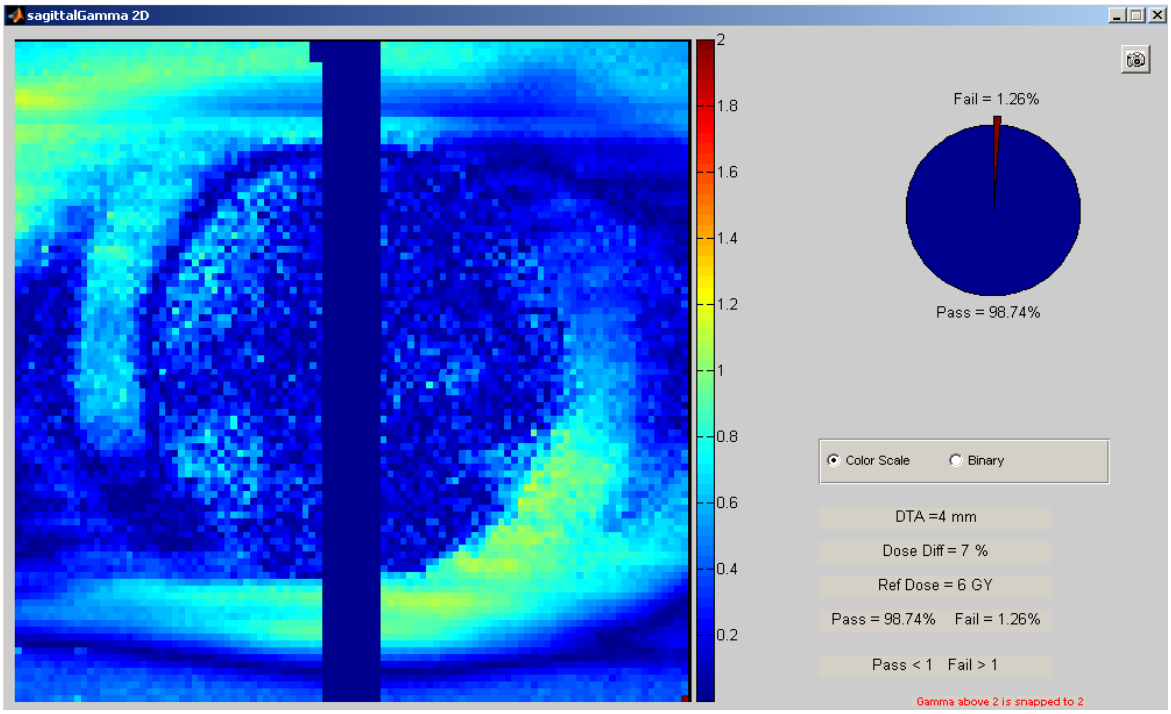

Figure 5.53 IMRT trial color scale gamma results for sagittal film normalized to TLD dose

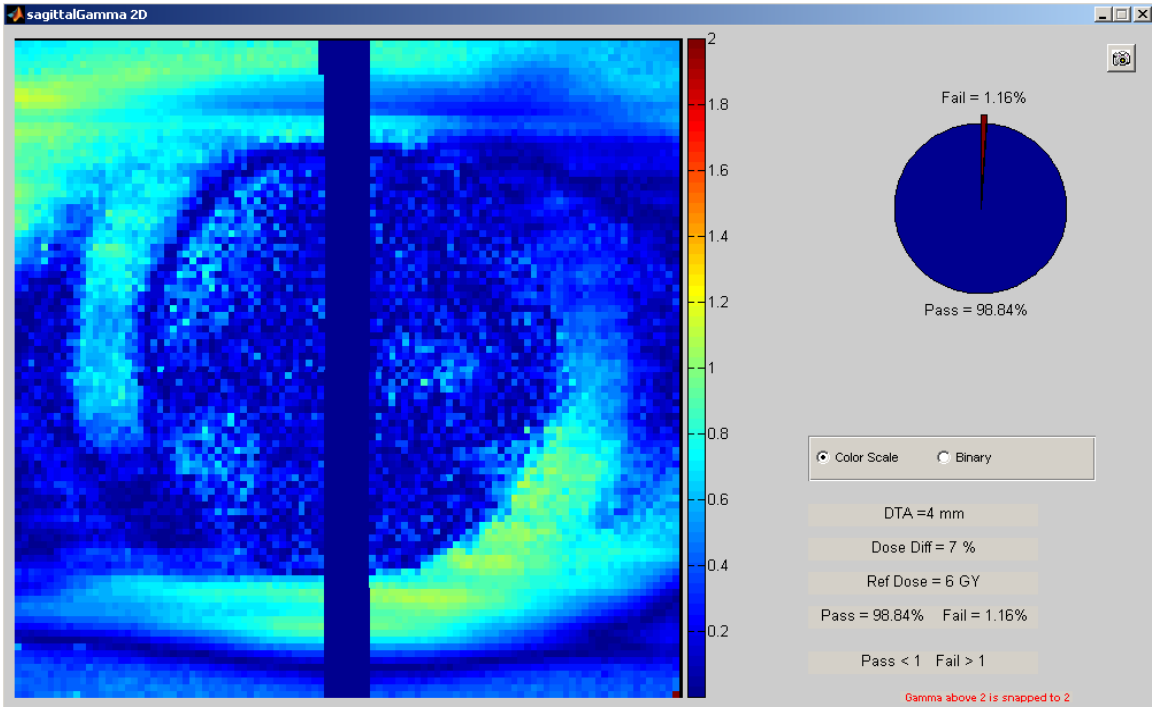

Figure 5.54 IMRT trial color scale gamma results for sagittal film normalized to corrected OSLD dose

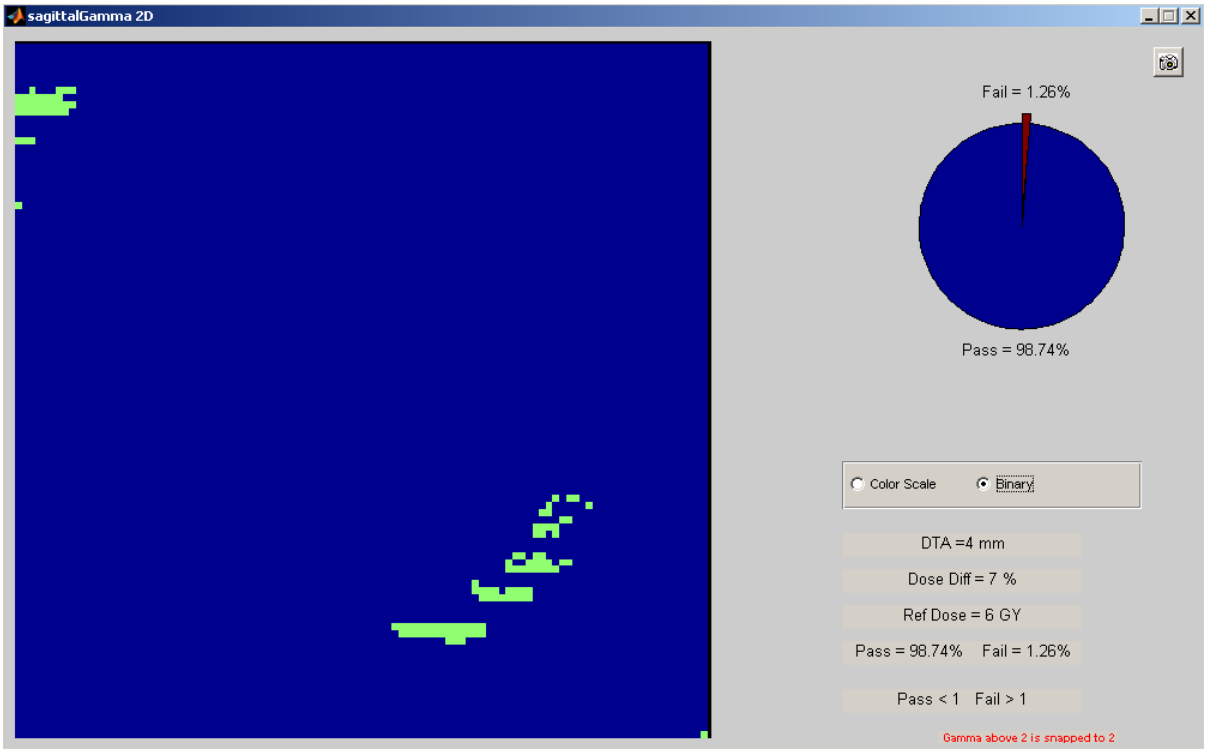

Figure 5.55 IMRT trial binary gamma results for sagittal film normalized to TLD dose

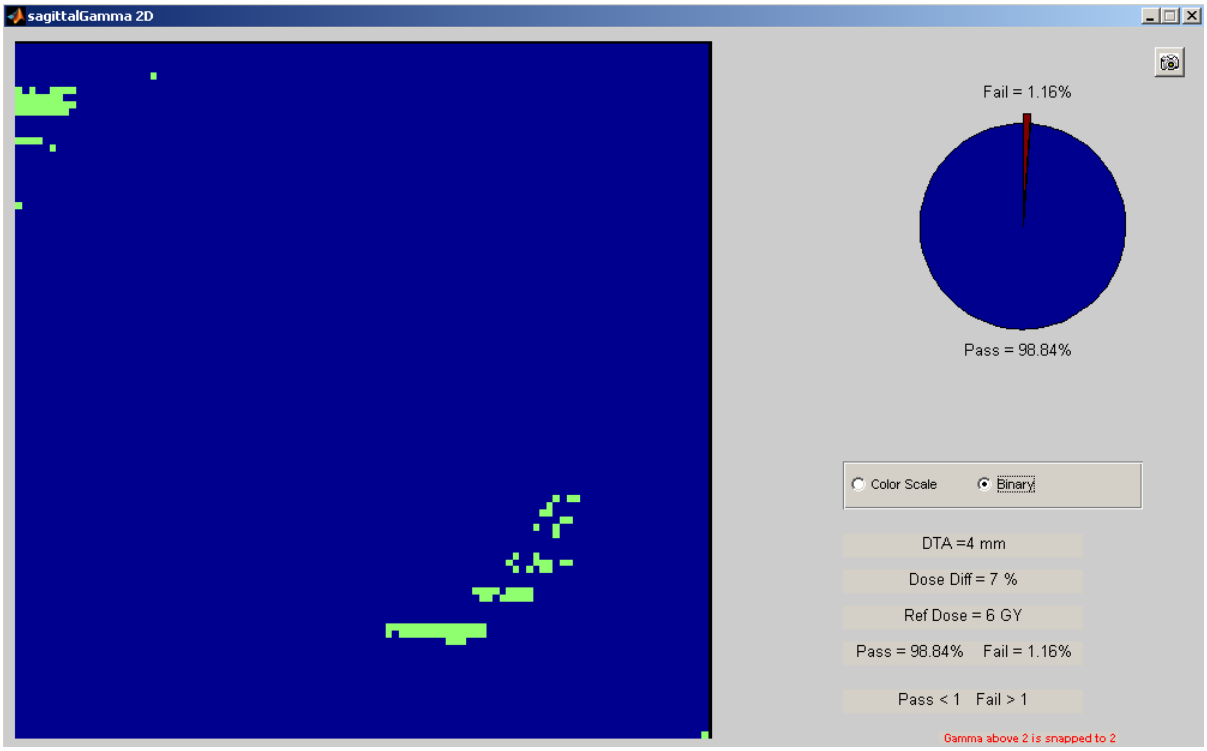

Figure 5.56 IMRT trial binary gamma results for sagittal film normalized to corrected OSLD dose

References

1 T. H. Kirby, W. F. Hanson, R. J. Gastorf, C. H. Chu, and R. J. Shalek, "Mailable Tld System for Photon and Electron Therapy Beams," Int J Radiat Oncol **12** (2), 261-265 (1986).

2 J. Aguirre, P. Alvarez, C. Amador, A. Tailor, D. Followill, and G. Ibbott, "WE-D-BRB-08: Validation of the commissioning of an optically stimulated luminescence (OSL) system for remote dosimetry audits," Med Phys **37** (6), 3428 (2010).

3 J. R. Kerns, S. F. Kry, N. Sahoo, D. S. Followill, and G. S. Ibbott, "Angular dependence of the nanoDot OSL dosimeter," Med Phys **38** (7), 3955-3962 (2011).

4 D. S. Followill, D. R. Evans, C. Cherry, A. Molineu, G. Fisher, W. F. Hanson, and G. S. Lbbott, "Design, development, and implementation of the Radiological Physics Center's pelvis and thorax anthropomorphic quality assurance phantoms," Med Phys **34** (6), 2070-2076 (2007).

5 E. G. Yukihara and S. W. S. McKeever, "Optically stimulated luminescence (OSL) dosimetry in medicine," Phys Med Biol **53** (20), R351-R379 (2008).

6 Eduardo G. Yukihara and S. W. S. McKeever, *Optically stimulated luminescence : fundamentals and applications*. (Wiley, Chichester, West Sussex, 2011).

7 M. S. Akselrod, V. S. Kortov, and E. A. Gorelova, "Preparation and Properties of Alpha-Al2o3c," Radiat Prot Dosim **47** (1-4), 159-164 (1993).

8 A. J. J. Bos, "High sensitivity thermoluminescence dosimetry," Nucl Instrum Meth B **184** (1-2), 3-28 (2001).

9 S. W. S. McKeever, M. S. Akselrod, L. E. Colyott, N. A. Larsen, J. C. Polf, and V. Whitley, "Characterisation of Al2O3 for use in thermally and optically stimulated luminescence dosimetry," Radiat Prot Dosim **84** (1-4), 163-168 (1999).

10 M. S. Akselrod, L. Botter-Jensen, and S. W. S. McKeever, "Optically stimulated luminescence and its use in medical dosimetry," Radiat Meas **41**, S78-S99 (2007).

11 C. S. Reft, "The energy dependence and dose response of a commercial optically stimulated luminescent detector for kilovoltage photon, megavoltage photon, and electron, proton, and carbon beams," Med Phys **36** (5), 1690-1699 (2009).

12 L. Bøtter-Jensen, S. W. S. McKeever, and A. G. Wintle, *Optically stimulated luminescence dosimetry*. (Elsevier, Amsterdam ; Boston ; London, 2003), 1st ed.

13 A. Viamonte, L. A. R. da Rosa, L. A. Buckley, A. Cherpak, and J. E. Cygler, "Radiotherapy dosimetry using a commercial OSL system," Med Phys **35** (4), 1261-1266 (2008).

14 V. Schembri and B. J. M. Heijmen, "Optically stimulated luminescence (OSL) of carbon-doped aluminum oxide (Al2O3 : C) for film dosimetry in radiotherapy," Med Phys **34** (6), 2113-2118 (2007).

15 P. A. Jursinic, "Changes in optically stimulated luminescent dosimeter (OSLD) dosimetric characteristics with accumulated dose," Med Phys **37** (1), 132-140 (2010).

16 J.F. Aguirre, P. Alvarez, C. Amador, A. Tailor, D. Followill, and G. Ibbott, "Commissioning of an optically-stimulated luminescence (OSL) system for remote dosimetry audits", in *51st Annual Meeting of the American Association of Physicists in Medicine* (Anaheim, California, 2009).

17 P. A. Jursinic, "Characterization of optically stimulated luminescent dosimeters, OSLDs, for clinical dosimetric measurements," Med Phys **34** (12), 4594-4604 (2007).

18 E. G. Yukihara, E. M. Yoshimura, T. D. Lindstrom, S. Ahmad, K. K. Taylor, and G. Mardirossian, "High-precision dosimetry for radiotherapy using the optically stimulated luminescence technique and thin Al2O3 : C dosimeters," Phys Med Biol **50** (23), 5619-5628 (2005).

19 E. G. Yukihara, P. B. R. Gasparian, G. O. Sawakuchi, C. Ruan, S. Ahmad, C. Kalavagunta, W. J. Clouse, N. Sahoo, and U. Titt, "Medical applications of optically stimulated luminescence dosimeters (OSLDs)," Radiat Meas **45** (3-6), 658-662 (2010).

20 C.A. Perks, C. Yahnke, and M. Million, "Medical dosimetry using optically stimulated luminescence dots and microStar readers", in *12th International Contress of the International Radiation Protection Association* (Buenos Aires, Argentina, 2008).

21 M. S. Akselrod, A. C. Lucas, J. C. Polf, and S. W. S. McKeever, "Optically stimulated luminescence of Al2O3," Radiat Meas **29** (3-4), 391-399 (1998).

22 S. C. Sharma, J. T. Ott, J. B. Williams, and D. Dickow, "Commissioning and acceptance testing of a CyberKnife linear accelerator," J Appl Clin Med Phys **8** (3), 119-125 (2007).

23 P. R. Almond, P. J. Biggs, B. M. Coursey, W. F. Hanson, M. S. Huq, R. Nath, and D. W. O. Rogers, "AAPM's TG-51 protocol for clinical reference dosimetry of high-energy photon and electron beams," Med Phys **26** (9), 1847-1870 (1999).

24 "A Protocol for the Determination of Absorbed Dose from High-Energy Photon and Electron-Beams," Med Phys **10** (6), 741-771 (1983).

25 F. Aguirre, P. Alvarez, C. Amador, A. Tailor, D. Followill, and G. Ibbott, "Validation of the commissioning of an OSLD system for remote dosimetry", in *52nd Annual Meeting of the American Association of Physicists in Medicine* (Philadelphia, Pennsylvania, 2010).

26 J. R. Kerns, S. F. Kry, and N. Sahoo, "Characteristics of optically stimulated luminescence dosimeters in the spread-out Bragg peak region of clinical proton beams," Med Phys **39** (4), 1854-1863 (2012).

27 A. Niroomand-Rad, C. R. Blackwell, B. M. Coursey, K. P. Gall, J. M. Galvin, W. L. McLaughlin, A. S. Meigooni, R. Nath, J. E. Rodgers, and C. G. Soares, "Radiochromic film dosimetry: Recommendations of AAPM Radiation Therapy Committee Task Group 55," Med Phys **25** (11), 2093-2115 (1998).

28 B. Arjomandy, R. Tailor, A. Anand, N. Sahoo, M. Gillin, K. Prado, and M. Vicic, "Energy dependence and dose response of Gafchromic EBT2 film over a wide range of photon, electron, and proton beam energies," Med Phys **37** (5), 1942-1947 (2010).

29 D. A. Low, W. B. Harms, S. Mutic, and J. A. Purdy, "A technique for the quantitative evaluation of dose distributions," Med Phys **25** (5), 656-661 (1998).

Vita

Jennelle Emily Bergene was born in St. Cloud, Minnesota on June 24, 1986 to Myron Imholte and Carol Seibert. She graduated high school from Becker, Minnesota in 2004 and entered South Dakota State University. She graduated cum laude from SD State in 2009 with a Bachelor of Science degree in Physics, and a minor in Mathematics. In August of 2010, she entered the Medical Physics graduate program at the University of Texas Health Science Center at Houston Graduate School of Biomedical Sciences.